GROWTH OF COMPLEX FRACTURE SYSTEMS IN EXTENSIONAL TECTONIC SETTINGS ON EARTH AND THE MOON WITH APPLICATIONS TO TECTONIC GEOMORPHOLOGY, FAULT ROCK EVOLUTION, AND DIKE EMPLACEMENT

by

Melanie B. Callihan

(Under the Direction of Christian Klimczak)

ABSTRACT

Planetary surfaces record an abundance of information on lithospheric evolution. Low rates of erosion allow for long-term preservation of structures, and on airless planetary bodies this can be billions of years. One such body is the Moon, which displays a long record of planetary tectonics on its surface. Brittle deformation in the form of fracturing provides vital clues for the characterization of the tectonics of the body, including localization, distribution, and kinematics of deformation in the lithosphere, lithospheric strength properties, and the underlying tectonic processes that are responsible for the observed deformation. Analyzing brittle deformation structures has direct implications for understanding planetary evolution, and this dissertation specifically addresses the extensional tectonics that cause complex fracture system formation and interactions with magmatism and volcanism, such as dike emplacement. Similarly, on

Earth, brittle structures reveal the inner processes of our planet and analogue field studies on Earth are crucial to interpret geologic processes on extraterrestrial worlds.

Research presented in this dissertation uses fractures on planetary bodies to piece together a more cohesive understanding of how brittle structures evolve considering deformation kinematics, strength properties, and tectonic processes. In this research, I present an in-depth characterization of 14 major lunar grabens, with detailed descriptions of their geomorphology and geometry. By studying individual faults bounding these grabens, I address the evolution of faults: how faults grow, patterns they exhibit, loading conditions required for formation, and fault rock evolution over time. Graben formation on planetary bodies has previously been tied to dike intrusion and relates to an analysis of the King's Bowl fracture system at Craters of the Moon National Monument and Preserve. A detailed investigation of fracture-lava interaction and dike intrusion was conducted by combining a field investigation with an Unpiloted Aerial Vehicle campaign. By studying the interaction of fractures and lava flow, I address the timing relationships for fracture formation as well as the topographic signatures caused by emplacement of a dike. These results are compared to models of dike intrusions with implications for the understanding of complex subsurface plumbing systems for Earth and similar sites on the Moon and other planetary bodies.

INDEX WORDS: Tectonic geomorphology, structural geology, planetary tectonics, Moon, Craters of the Moon National Monument, Idaho, King's Bowl, volcanic-tectonic interaction.

GROWTH OF COMPLEX FRACTURE SYSTEMS IN EXTENSIONAL TECTONIC SETTINGS ON EARTH AND THE MOON WITH APPLICATIONS TO TECTONIC GEOMORPHOLOGY, FAULT ROCK EVOLUTION, AND DIKE EMPLACEMENT

by

MELANIE B. CALLIHAN

BS, University of Mississippi, 2010

MS, University of Minnesota Duluth, 2013

A Dissertation Submitted to the Graduate Faculty of The University of Georgia in Partial Fulfillment of the Requirements for the Degree

DOCTOR OF PHILOSOPHY

ATHENS, GEORGIA

2020

GROWTH OF COMPLEX FRACTURE SYSTEMS IN EXTENSIONAL TECTONIC SETTINGS ON EARTH AND THE MOON WITH APPLICATIONS TO TECTONIC GEOMORPHOLOGY, FAULT ROCK EVOLUTION, AND DIKE EMPLACEMENT

by

MELANIE B. CALLIHAN

Major Professor:	Christian Klimczak
Committee:	Douglas E. Crowe
	Robert B. Hawman
	Paul K. Byrne

Electronic Version Approved:

Ron Walcott
Interim Dean of the Graduate School
The University of Georgia
May 2020

DEDICATION

For Isabel and Stephen, who always believe in me.

ACKNOWLEDGEMENTS

I'd like to first acknowledge and thank my committee members: Dr. Christian Klimczak, Dr. Doug Crowe, Dr. Rob Hawman, and Dr. Paul K. Byrne. These professors provided guidance, advice, and support whenever I needed it and helped me become the structural geologist I am today. Thank you to Dr. Crowe for helping me pursue the career path I have dreamed of, to Dr. Hawman for his kindness and encouragement that he always gives so freely, and to Dr. Byrne who helped getting my last project started. I also want to extend a special thank you to my mentor, Dr. Christian Klimczak. Over the last 4.5 years he has taught me so much, and always been there for me with advice and guidance. He's pushed me to learn, to ask more questions, and helped me to become a better scientist. He's been honest, which is one of the qualities that I appreciated the most, but also kind, and understanding to situations when life throws a curveball. I can now return the favor and honestly say, that my experience without Dr. Klimczak would not have been the same in regard to lessons learned, experience gained, overall fun had while pursuing this degree.

I would also like to thank the people that were instrumental to complete my most recent research. Cash A. Owens was tremendous help in the field, which included being an amazing field and conversation partner, but also a retriever of phone that got dropped into fractures or lost in the prairie. And to my dear friend Andrea Bowen, who took time to help me complete my fieldwork. I would not have been able to process the data for my last project without the help, conversations, encouragement, and computing power

provided by Dr. Tripp C. Lowe III. I would also like to thank Todd Stefanic, who helped to make it possible to conduct my UAV field work.

I am grateful for the research and travel funding I have received over the years, provided by the Department of Geology and the Graduate School as well as the Geological Society of America for helping me fund my research. I'd like to extend gratitude to the Planetary Division of GSA and the Association of Women Geoscientists for supporting me in traveling to conferences so I could present my research.

I want to also acknowledge my office mates Jupiter, Sierra, Isik, that over the last few semesters have become good friends, and that made the end of this PhD more fun with insightful conversations, laughter and shared cultural experiences. Last, and definitely not least, I want to thank my family. To my parents, Andrea and Gisbert Bergmann, who let me move across the world to pursue my goals and who are supportive when I call at any hour of the day. To my brother and family, who are always cheering me on and reaching out when I most need it. And also, to my American family, Matt and Margaret Callihan, without your support I would not have been able pursue these goals, thank you for the kind words and love. A very special thanks goes out to my daughter Isabel, who has been the most wonderful addition to my life, and brightens my every day. A hug from her has cured any cloudy day I had.

Most of all I want to thank most of all my husband, Stephen, who has been my rock, and constant supporter, my person, and someone that reassures me, and tells me truths I need to hear. Even when I do not believe in myself, I know he is the one person that will. I most definitely would not have completed this without your constant support and help. I'm grateful that he is my partner in life, and for keeping up with all my crazy ideas.

TABLE OF CONTENTS

Page

LIST OF TABLES

Page

LIST OF FIGURES

Page

CHAPTER 1

INTRODUCTION AND LITERATURE REVIEW

Extensional structures, such as fractures, are important expressions of brittle deformation and reflect the nature of stresses that are present in the lithosphere of Earth and other planetary bodies, such as the Moon. Opening mode fractures are sharp, planar to sub-planar discontinuities displaying a local reduction in strength. Fractures can be categorized as shear fractures, opening fractures, (including joints, veins, fissures, and dikes) or closing fractures (Fossen, 2009, Schultz and Fossen, 2008). Joints (also referred as tension cracks and tension fractures) are sharp structural discontinuities where field evidence highlights predominantly opening between opposing walls (Schultz and Fossen, 2008). Dikes and fissures are also opening-mode cracks, but only dikes are magma-filled at depth (Pollard et al., 1983; Mastin and Pollard, 1988). Fractures with shear movement along slip planes, and larger displacement, and fault core or fault damage zone are termed faults (Fossen, 2009; Schultz, 2019). Normal faults are defined as planar discontinuities with shear displacement accommodated by frictional slip, displaying an established sheared fault core or a well-developed slip zone (Schultz and Fossen, 2008). Normal faults may evolve to complex graben over time in extensional tectonic settings where faulting occurs continuously and creates fault populations that include oppositely dipping normal faults. Graben themselves are defined as linear landforms that display a down-dropped crustal block bound by two oppositely-dipping (antithetic) normal faults (Schultz et al., 2007; Fossen, 2009) and have been the subject of many studies on Earth but also on

other planets (e.g., Golombek, 1979; Golombek and McGill, 1983; Schultz et al., 2006; Polit et al., 2009; Wieczorek et al., 2013; Nahm and Schultz, 2013; Klimczak, 2014; French et al., 2015; Nahm, 2016; Nahm and Dudde, 2016). As these extensional structures grow, they develop from simple fractures to faults and even more complex systems of segmented, interacting fault systems. This increase in complexity with continued growth of discontinuities also pertains to rift formation. Rifting occurs when lithospheric crust is pulled apart by tectonic forces and causes the formation of discontinuities along linear margins.

The intrusion of dikes can lead to the formation of lunar grabens, which is widely known and documented (Head and Wilson, 1993; Klimczak, 2014; Wilson and Head, 2018), as well as other planetary bodies (Wilson and Head, 2002; Schultz et al., 2004a; Polit et al., 2009; Hardy, 2016). Similarly, dike intrusion has been suggested to drive early stage graben deformation on Earth (Pollard et al., 1983; Mastin and Pollard, 1988; Rubin and Pollard, 1988; Rubin, 1992), along the Great Rift of the Eastern Snake River Plain in Idaho (Greeley and Schultz, 1977; Greeley, 1982; Kuntz, 1992; Kuntz et al., 2002, 2007; Holmes et al., 2008). During the intrusion of a dike, the general surrounding region will experience uplift, creating a rise directly above the dike. Tension cracks form along the inflection points of the resulting sloping topography (Pollard et al., 1983; Rubin, 1992). Both of these features can be observed and investigated in topography.

Studying these extensional structures and analyzing their geomorphological and geometrical characters, spatial extent, and topographic expressions can highlight the evolution of planetary tectonic environments and shed light on the causes and mechanisms of their formation. This dissertation explores and documents in great detail

how fractures and faults grow in extensional tectonic settings on Earth and the Moon, and what their structural patterns and topography reveal about rock properties and formation mechanisms.

Normal faults and fractures can be traced across most planetary surfaces by long, linear surface breaks that dissect the terrain (Figure 1.1). Normal faults may display substantial shear displacements that are apparent in the local topography, and fractures will generally appear as opening-mode discontinuities. These geologic structures can be studied on Earth and planetary bodies using photogeology (Figure 1.1A, B) and topography collected by images and altimeter instruments onboard spacecraft. On Earth, such remote sensing can be ground-truthed by traditional field methods. With recent scientific advances, we are now able to utilize Unpiloted Aerial Vehicles (UAVs) to collect orthoimagery (Fig. 1.1 C, D) to study the surface of the Earth in unprecedented detail with resolutions as low as centimeters per pixel and spatial coverage of an area of 0.5 km^2 with just one flight (one battery). This data can be further processed to produce Digital Elevation Models (DEMs) that reveal an unprecedented amount of detail in topography. To better understand planetary structures and their Earth analogues they are described based on their spatial extent, topographic expressions, and morphological patterns. Frequently, further analysis and modeling are applied to understand the growth and formation of these structures.

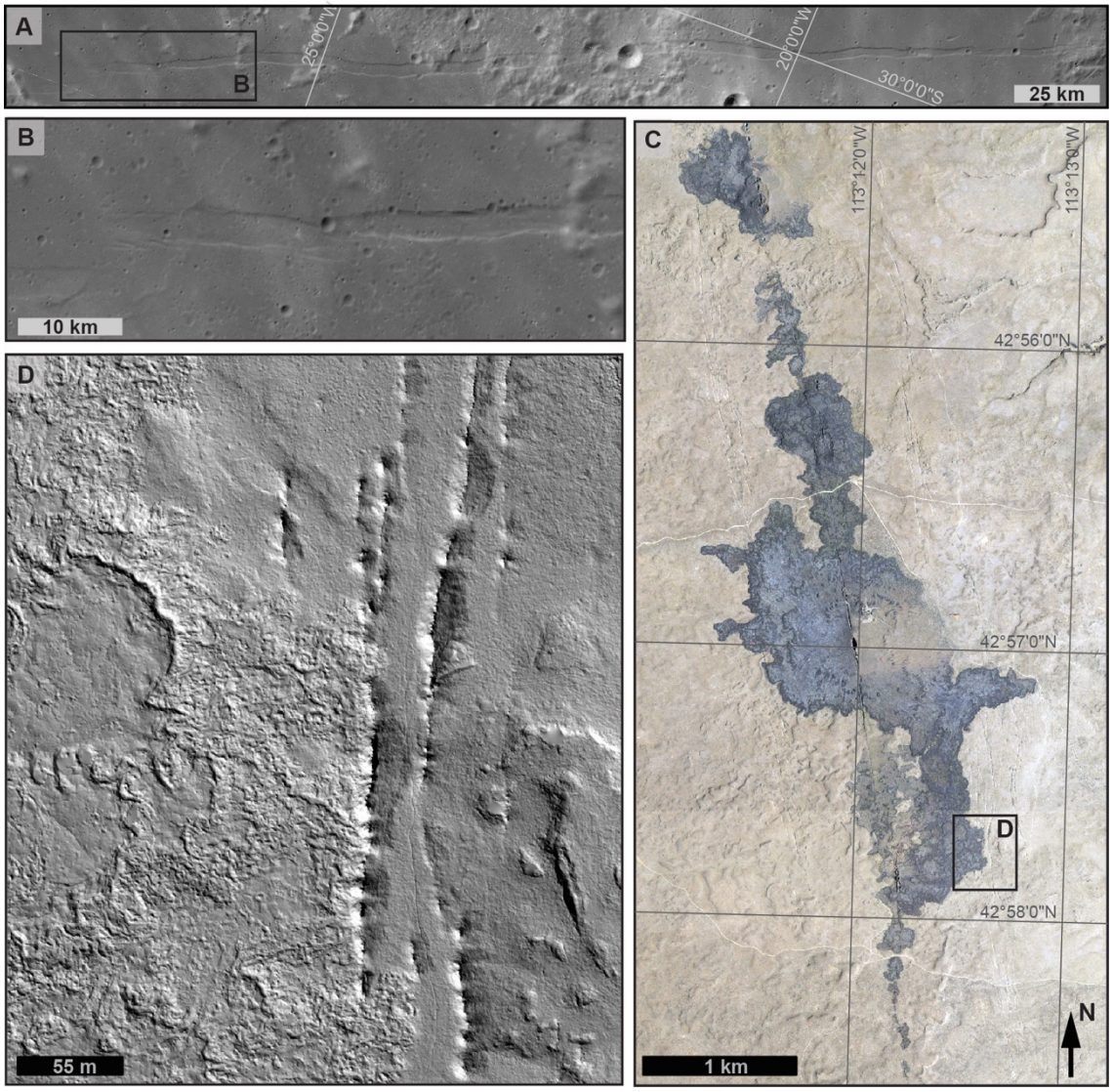

Figure 1.1 Examples of complex fracture systems on the Moon and Earth from this dissertation. (A) A Lunar Reconnaissance Orbiter image mosaic shows multiple normal faults form the graben named Rima Hesiodus. Image in north pole orthographic projection centered at 23°0’0” W and 30°0’0” S. (B) Insert shows intricate fault interaction in detail, displaying multiple overlaps and linked faults. (C) Example of rift system on Earth, an eruptive fissure marks the center of the rift system, centered at 42°56’57” N, 113°12’54” W in Transverse Mercator projection. (D) UAV-derived

hillshade (40° azimuth and 90° sun angle direction) reveals a complex fracture system paralleling the fissure.

In general, these extensional structures are first characterized by their geometries: fault length in map view, recording the surface extent of the fracture or fault. Fault displacement, the total recorded fault offset considering horizontal and vertical movement, which is represented by the horizontal and vertical components, heave and throw, respectively, is recorded. Together with topography, these geometries can be used to investigate the relationship between length and displacement using slip distributions. Complex fracture systems, such as grabens, appear in multiple segmented fractures or faults, the overlap and spacing of which, as well as the ratio between fault length and displacement can relay information on fault growth patterns, and mechanical stratigraphy of the lithosphere (Watters et al., 2000; Schultz et al., 2006; Polit et al., 2009; Vaz et al., 2014; Stubblefield, 2019; Studer-Ellis, 2019). Other studies have used these geometric relationships to establish a framework that explains fault slip distributions (Cowie and Scholz, 1992; Bürgmann et al., 1994; Schultz et al., 2004b, 2006; Klimczak, 2014; Klimczak et al., 2018). Fault growth modeling methods include linear elastic fracture mechanics modeling, post-yield fracture mechanics modeling, and symmetric linear stress distributions, and are applied to constrain loading conditions and host rock yield strength. None of these growth models have been directly compared to a fault population but can be applied to better understand how host rock and loading conditions change over

time. Therefore, these studies can be used to investigate the growth for these complex fracture or fault systems.

Surface expressions of extensional structures

Brittle deformation accommodates extension via fractures and faults, and ultimately leads to formation of complex graben and rift systems. In map view, these structures appear as sharp, linear surface breaks that may reveal a juxtaposition of older next to younger rock units on the surface. All large structures begin with microscopic discontinuities, or cracks, that grow larger into fractures, faults, and more complex systems.

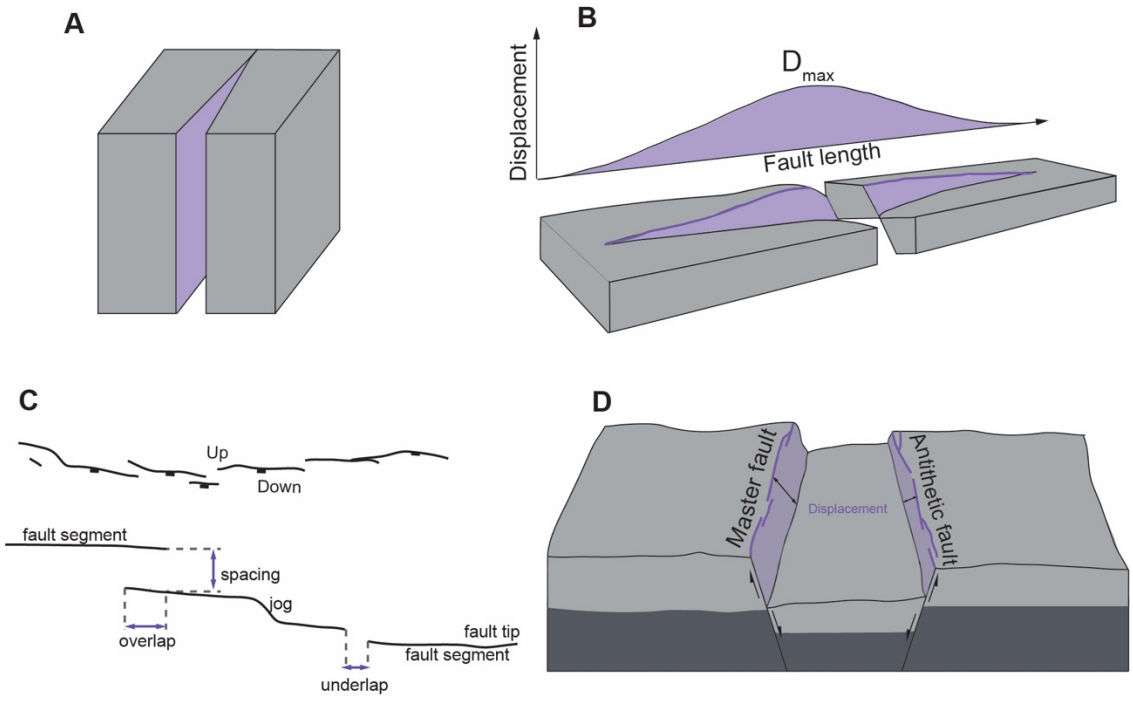

Figure 1.2 Structural discontinuities and their surface expressions as discussed in this dissertation grow from fractures to more complex fracture systems. (A) Opening-mode fracture with displacement perpendicular to fracture wall. (B) Block diagram and

associated slip distribution of an isolated normal fault showing slip (purple) along the strike of the fault, and displacement profile with D_{max} in the center of the fault length. The slip distribution highlights how displacement changes along fault length. Image modified after Fossen (2009). (C) Map view of normal faults showing interaction and fault linkage patterns in en echenlon faults, including overlap, underlap and spacing, and a jog. With increasing number of slip events on the fault plane in extensional tectonic settings, complex systems grow that display en echelon faults segments and different types of fault interaction. Image modified after Willemse (1997). (D) Block diagram of a graben system. Extensional tectonic settings can lead to the formation of graben, with two oppositely dipping normal faults (can be composed of multiple fault segments), that create a flat, down-dropped block in the center.

The tectonic stress regime governing the formation of normal faults was first defined by Anderson's fault classification (1951), where a combined vertical maximum compressive stress and horizontal minimum compressive stress causes structures to slip at a ~60° orientation to the horizontal. Single isolated normal faults (Figure 1.2B) can be used as an analogy as one half of a graben, i.e., a half-graben. The lateral extent of a single fault corresponds with the total length of the fault terminating in the fault tip points. Displacement, which is the (shear) offset created during faulting, gradually changes along the length of the fault and portrays the maximum displacement (D_{max}) in the center (Figure 1. 2B). Structural geologists have studied normal fault growth in

complex graben and rift systems (Peacock and Sanderson, 1991; Trudgill and Cartwright, 1994; Dawers and Anders, 1995; Willemse, 1997; Cartwright and Mansfield, 1998; Gupta and Scholz, 2000; Peacock, 2002; Finch and Gawthorpe, 2017; Peacock et al., 2017b; Rotevatn et al., 2018). Individual normal faults grow in length by the propagation of fault tips during slip events that enlarge the displacement along the fault plane. Displacement and length are accumulated and grow larger over time with increasing number of slip events on the fault plane (Cowie and Scholz, 1992b; Shipton and Cowie, 2003). Displacement and length frequently show a linear scaling relationship (Cowie and Scholz, 1992; Cartwright et al., 1995; Dawers and Anders, 1995; Mansfield and Cartwright, 2001; Schultz and Fossen, 2002; Kim and Sanderson, 2005; Soliva and Benedicto, 2005; Soliva and Schultz, 2005). In a region under tectonic stress, a group of faults may grow, rather than a single isolated fault, establishing a fault population composed of faults with similar trend and geometric properties (Fig. 1.2C) (Fossen, 2009; Schultz and Fossen, 2008). Fault growth in a population also may occur via fault linkage or coalescing with smaller regional faults over time (Cartwright et al., 1995). These en echelon faults create characteristic map patterns, consisting of multiple fault segments rather than one single fault slip plane (Willemse, 1997; Fossen et al., 2010; Rotevatn et al., 2018).

Two segmented faults that approach another, but yet do not link, are said to underlap (Figure 1. 2C), which reaches a critical point when fault segments and their stress fields start to interact with each other (Willemse, 1997). Overlapping faults are characterized by fault tips that have moved past one another (Fig. 2.2). Once the interaction between segments begins, the fault tip propagation will temporarily arrest, and

fault tips begin curving toward each other (Peacock and Sanderson, 1991; Willemse, 1997; Fossen and Rotevatn, 2016). Structures are considered to be soft-linked (over- and underlapping) until further slip events causes the two faults to physically connect and the faults link. This is considered as a breached relay ramp and the two fault segments are now hard-linked (Willemse, 1997). The connecting segment between the originally discontinuous faults is called a jog (Figure 1.2 C) and represents the breached portion of the relay ramp (Willemse, 1997; Peacock, 2002). The linkage of smaller segmented faults in a population can lead to the formation of complex structures in map view and in the subsurface.

With sustained extensional tectonics, the normal faults grow into graben (Fig. 1.2D). For this dissertation, we consider a graben or rift system composed of fractures to be complex if it is composed of multiple interacting structures rather than a single fault plane. Each graben consists of a master and subordinate fault oriented antithetically to the master fault. The master fault corresponds to the fault with the larger displacements in the system, whereas the antithetic fault is smaller fault dipping towards the master fault (Fig. 1.2D). Grabens have been studied in respect to better understand their formation, their role in landscape and structural evolution, and also as hosts of economic resources in the petroleum industry (e.g., Melosh and Williams, 1989; Fossen et al., 2010; Allken et al., 2013).

As part of this dissertation, I analyzed brittle deformation structures in extensional tectonic environments. I collected an abundant amount of data on complex fracture systems on the Moon and Earth, including spatial distribution, map patterns they exhibit, and fracture geometry. I used this information to investigate fracture growth and to test a

fault growth model in order to constrain how loading conditions and rock properties change over time. Additionally, I examined the topography of geologic structures growing in extensional tectonic regimes and contributed to the understanding of topographic expressions of fractures and topography related to dike intrusion.

Data products of this dissertation include detailed structural maps for long lunar graben highlighting fault growth patterns in map view, high-resolution orthoimage mosaics for the lunar analogue site at Craters of the Moon National Monument and Preserve, Idaho, fine-scale DEMs for the same location, and assessments of topography across the King's Bowl Rift. This work provides substantial contributions to the understanding of how fractures and faults grow into the complex systems in extensional tectonic settings that we observe them in. Chapter 2 provides the first in-depth description of long lunar grabens with implications for fault growth understanding. Chapter 3 further illustrates normal fault growth on the Moon, identifying specific loading conditions and strength properties in the lithosphere that were required for fault growth. Chapter 4 presents a lunar analog study on Earth, showing how fractures and topography can be governed by the intrusion of a surface-breaching dike.

Chapter 2 Overview

Grabens have been long recognized at different scales on the Moon (Golombek, 1979; Hiesinger and Head, 2006; Watters and Johnson, 2010; Klimczak, 2014; Nahm, 2016; Nahm and Dudde, 2016). The lack of major erosional processes on the Moon has preserved morphologies and topographic expressions of these landforms, allowing us to study the evolution of normal faults. Grabens are linear landforms composed of multiple segmented normal faults flanking a down-dropped block in the center (Fig. 1.1 A, B)

(Schultz et al., 2007; Fossen, 2009). *Lunar Reconnaissance Orbiter (LRO)* camera and altimetry data have allowed us allowing us to investigate graben-bounding fault length, segmentation, offset, fault displacement, and the overall fault growth to become complex graben systems.

Grabens had been previously identified across the lunar surface, bordering to the maria (Golombek and McGill, 1983; Watters and Johnson, 2010; Nahm, 2016), as part of floor-fractured craters (Schultz, 1976; Jozwiak et al., 2012, 2015), at small, local scales (Watters et al., 2000; Watters and Johnson, 2010; French et al., 2015), and within large impact basins (Wilhelms et al., 1979; Nahm, 2016). Prior to Chapter 2, none of these studies systematically studied the topographic expressions of large lunar grabens, specifically addressing the along-strike characteristics and relationships between fault displacement and length. We used *LRO* data to investigate 14 grabens, across different terrains and locations on the Moon. Our study revealed that the grabens range in length from 43 km to 453 km, with displacements of up to 1115 m. Displacement was plotted as a function of length using slip distributions, revealing individual growth patterns between faults, and highlighting fault interactions. Fault growth is attributed to propagation via fault interaction, which is supported by observed sublinear fault growth patterns. Additionally, this study revealed scaling ratios that are higher than previously estimated. These results are the basis for understanding mechanical properties of host and fault rocks and how they changed during fault growth.

Chapter 3 Overview

Even though the previous study gave us an in-depth look at the extent, spatial distribution, complex faulting relationships, and growth patterns of long lunar graben,

questions about their formation remain. Since these grabens are widely distributed across the lunar surface along different terrains and host rock types, I wanted to gain a better understanding under which conditions each of these grabens formed. Post-yield fracture mechanics (PYFM) fault growth modeling has been suggested to reveal stress and strength conditions during fault formation (Cowie and Scholz, 1992). PYFM modeling produces a bell-shaped displacement profile, with maximum displacement along the center of the fault length, tapering towards the fault tips. This model relates the strength of the host rock to the frictional resistance to sliding and loading conditions of the fault plane.

We used the previously produced slip distributions of the 14 graben complexes and matched them with PYFM model solutions. In particular, by matching the observed slip distributions with models, we simulated host rock strength and required far-field tectonic stress—both as values averaged over the lifetime of the fault—that are needed for the fault to grow to the observed shape for each individual fault segment. In total, we produced and matched 89 PYFM model solutions. We found that there is a dependency of stress and strength properties with fault length. Shorter fault systems generally require higher remote stress to propagate in comparison to longer fault systems, but interestingly, rock properties and loading conditions within the systems itself are found to evolve in two ways. For the master fault systems of 9 grabens they remain constant irrespective of the length of the individual fault lengths, and for the master fault systems of 5 grabens they are found to decrease for longer fault segments within their respective fault system. We attribute these findings to differences in fault gouge formation.

Chapter 4 Overview

The King's Bowl (KB) basaltic field at Craters of the Moon National Monument and Preserve, Idaho, is an excellent area to study the topographic uplift and fracture formation caused by a shallow or surface-breaching dike on the topography. As part of the Great Rift system of the Eastern Snake River Plain, KB is host to hundreds of fractures that parallel a north-south oriented eruptive fissure. The prevalent arid climate in the region has allowed for the preservation of ~ 2200-year-old basaltic lava flow and the fractures surrounding it. The formation of KB has long been attributed to the intrusion of a dike, but specific timing relationships between fracture formation and volcanic eruptions have not yet been addressed. Dike intrusion causes characteristic surface topography, which on the scale of KB, can be investigated in cm-scale DEMs. In turn, this can be used to test if previously hypothesized dike dimensions (Holmes et al., 2008) cause the derived topography by modeling dike-induced ground displacement that can be compared to observed topography.

Our field observations provide evidence for fracture formation before and during continued uplift caused by dike intrusion but pre-dating the eruption of basaltic lava. At seven locations across KB, we documented interaction between fractures and lava highlighting lava flowing into fractures, lava flow surface deformation, and lava squeezing upwards through fractures. Using UAVs to collect orthographic images allowed us to build high-resolution DEMs. These data products were used to extract detailed long-wavelength topographic profiles across the rift for analysis and interpretation, revealing a 10 m rise with a width of 1.5 to 3 km across the rift zone. Size, dimensions, and shape of this rise suggest that it was caused by a dike. We compared

numerical outputs of ground displacements produced using the open-source USGS COULOMB code to investigate the geometric properties of a dike that would cause the observed topography. Previously proposed dike dimensions do not produce the observed rise, whereas unusually shallow but wide dikes reflect the observed topography, overall suggesting a more complex subsurface arrangement of intrusive structures.

Significance

The brittle structures left behind on bodies in our Solar System record a rich history of fractures and faults that preserve information on stresses in the lithosphere and possible mechanisms that drive them. The geomorphologic patterns, global, regional, or local distribution, and topographic signatures of fractures, faults, and grabens provide clues to understanding local and regional stress environments and other processes such as dike emplacement. A better understanding of structures and their kinematics will improve knowledge addressing not only academic questions but also affect studies with real-life applications. Fault growth mechanisms and patterns may be informative for earthquake resources. Learning how fracturing, fault rocks, and fault gouge evolve during increasing number of slip events on the fault plane may apply in studies concerning fluid flow, which is vital for the petroleum and environmental industries.

Each chapter in this dissertation addresses aspects of extensional tectonics. Chapter 2 sheds light on the geomorphological characteristics of long lunar graben in unprecedented detail and then investigates fault growth and the relationship between displacement and length for these structures. Chapter 3 reveals how several lunar normal fault systems and the fault rock associated with them behaved over time, showing how loading conditions and host rock strength evolved. Chapter 4 examines an analogue site

on Earth that constrains timing between dike emplacement, fracture formation, and lava flows, revealing the topographic signature of a dike. Together, these chapters advance our understanding of fracture and fault evolution in extensional tectonic settings, documenting topographic signatures and how they can be used to study their growth, changes in mechanical properties of the deformed rock, and volcanic-tectonic interactions.

CHAPTER 2

TOPOGRAPHIC EXPRESSIONS OF LUNAR GRABEN

[1] Callihan, M. B. and Klimczak. 2019. *Lithosphere.* 10.1130/L1025.1
Reprinted here with permission of the publisher.

Abstract

Grabens, landforms produced by normal faulting, have long been recognized on the Moon, but their map patterns, as well as topographic expressions, have not been studied systematically. The topography across grabens and its along-strike variations reveal details on the growth of the normal faults forming the grabens. Individual normal faults grow in length by the propagation of fault tips during slip events that also enlarge the displacement along the fault plane. Displacement and length are accumulated and grow larger over time with more slip events, fault interaction, and linkage. We measured fault lengths and vertical offsets, and then calculated the displacement for lunar grabens using data from the camera and laser altimeter onboard the Lunar Reconnaissance Orbiter. Our study systematically investigates 14 graben systems across the lunar surface. Graben lengths are found to range from ~43−453 km and displacements of ~127−1115 m. These displacements were plotted against graben fault length to produce slip distributions, which reveal growth patterns involving mechanical interaction and fault linkage. Displacement-to-length scaling was used to further study the evolution of graben-bounding normal faults. We observe a sub-linear growth pattern for lunar graben-bounding normal faults, consistent with growth of faults via segment linkage where different stages of linkage are present on the lunar surface. Lunar graben-bounding faults show higher scaling ratios than previously estimated, likely due to variations in host rock properties and mechanical stratigraphy.

Introduction

Planetary bodies lacking major erosional processes and atmospheres, such as the Moon, preserve the morphologies and topographic expressions of major landforms over long timescales. This enables us to study faults in terms of their lateral extent, segmentation, offset, fault displacement and the overall fault evolution. In recent years the collection of high-resolution topographic measurements from the Lunar Laser Orbiter Laser Altimeter (LOLA) (Smith et al., 2010) on board of the Lunar Reconnaissance Orbiter (LRO) gathered the data essential to create an in-depth understanding of lunar faults and structures. Using lunar graben geomorphology, geometry, displacement-to-length scaling, and overlap-to-spacing ratios, this study aims at creating a better understanding of the growth of graben-bounding normal faults on the Moon.

Graben geomorphology

Normal faults, inclined planar discontinuities along which extensional strains are accommodated via frictional sliding, are commonly found across the surface of the Moon (Golombek, 1979; Hiesinger and Head, 2006; Smith et al., 2010; Watters and Johnson, 2010; Klimczak, 2014; Nahm, 2016). Grabens are linear landforms marked by multiple, oppositely dipping (antithetic) normal faults, that create a down-dropped block in the center (Fig. 2.1) (Schultz et al., 2007; Fossen, 2009). Each displacement along the normal faults can be decomposed into its horizontal and vertical displacement components, heave and throw, respectively. Displacement is the total offset considering horizontal and vertical movement (Fig. 2.1) and can either be calculated using the fault dip and throw or be measured along slip. Grabens that show similar offset on both faults are symmetric. Frequently, however, the two graben-bounding faults show differences (asymmetry) in

displacement, where the fault with the higher displacement is considered the master fault, opposed by the lower displacement at the antithetic fault. The symmetry of a graben reveals information about its maturity. Asymmetric graben or half-graben typically indicate the early stages of graben development, but as they grow larger, they become more symmetric.

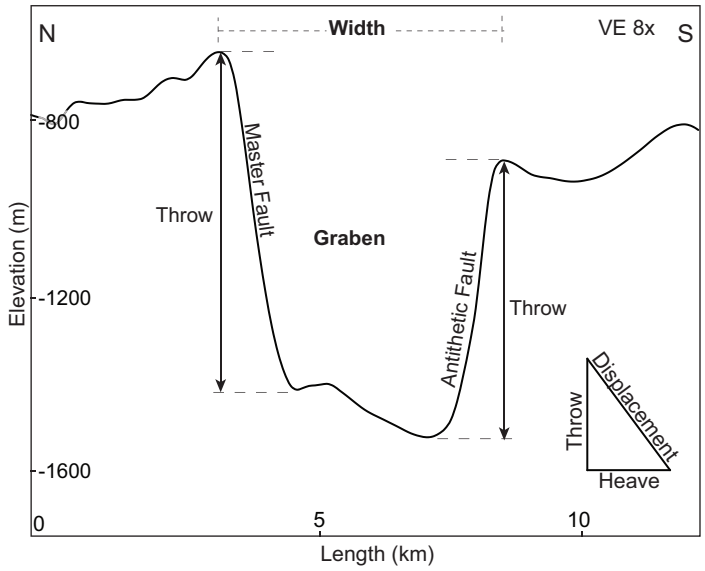

Figure 2.1 Topographic profile with eight times vertical exaggeration (VE) across a graben forming Rima Ariadaeus. Graben showing identified master and antithetic faults based on amount of throw/displacement.

However, information from displacement paired with map patterns show that long lunar grabens are either concentric or radial to the maria, where mare-concentric grabens, in particular, show the master fault dipping toward the mare center. Therefore, we interpret that formation of these grabens is linked to cooling of the lunar maria.

Generally, fault growth is governed by preexisting discontinuities, the local or regional stress field, rock strength, and pore fluid pressure (Arthur et al., 1963). Faults generally grow by accumulation of seismic slip (Walsh and Watterson, 1987; Cowie and Scholz, 1992a; 1992b) and fault linkage (Peacock and Sanderson, 1991; Cartwright et al., 1995; Mansfield and Cartwright, 2001). Isolated faults grow via continued slip events and enable the formation of fault populations in which groups of smaller faults occur in the same region. In the second case, faults can increase their length and displacement over time by linking or coalescing with smaller faults in the region (Cartwright et al., 1995). These arrays of sub-parallel (en echelon) small faults consist of fault segments rather than one single fault slip plane and form different characteristic structures in map and outcrop view (Willemse, 1997; Fossen et al., 2010). When two faults grow toward one another, they begin to mechanically interact (Peacock and Sanderson, 1991; Willemse, 1997; Gupta and Scholz, 2000; Peacock, 2002; Soliva and Benedicto, 2005). Two segmented faults that approach another, but are not physically linked, are said to underlap. Underlap reaches a critical point when fault segments and their stress fields start to interact with each other (Willemse, 1997). When fault tips have moved past one another, the faults are considered to be overlapping. Once interaction and linkage between segments begins, the fault tip propagation will temporarily arrest, and fault tips begin curving toward each other (Peacock and Sanderson, 1991; Willemse, 1997; Fossen and Rotevatn, 2016). Overlapping segments and underlapping segments are considered to be soft-linked when individual faults mechanically interact but do not form a continuous fault plane. Once the faults fully coalesce to form a single fault plane, the two original fault segments are considered hard-linked and can be identified by jogs or abrupt changes in fault

orientation in map view (Willemse, 1997; Soliva and Benedicto, 2004). Grabens that have grown by linkage of smaller segments as opposed to growth of a single isolated fault exhibit a much more complex set of structures and variety of map patterns. These map patterns show changes in spacing, overlap, and sudden changes in fault strike. Spacing is defined as the horizontal distance between two fault surfaces, whereas the overlap is the distance between the two individual overlapping fault tips.

To better understand fault growth, slip distributions have been used to analyze how the fault geometry varies with length and to describe the relationship between displacement and fault length. A slip distribution highlights changes in displacement along the fault length, which in a single fault shows a gradual increase in displacement from the fault tip to the fault center. The maximum displacement is located in the center of the fault trace. The general shape of the slip distributions can vary from peaked to more flattened or plateaued profiles. In cases where more than one fault is involved, slip distributions can reveal linked or interacting faults with respectively higher displacements that skew towards another. Fault growth via segment linkage is reflected in their slip distributions. Plateaued slip distributions arising from linked segments can indicate an intermediate stage of fault growth, whereas peaked slip distributions can indicate early or more advanced stages of fault growth (Peacock and Sanderson, 1991; Cartwright et al., 1995; Kim et al., 2004). Our analysis reveals how displacement changes with fault length, how faults mechanically interact, and how that affects the shape and magnitude of a slip distribution. Additionally, slip distributions and scaling allows us to infer information on the mechanical rock properties and regional stresses (Cowie and Scholz, 1992b) for future research on lunar normal faults.

Previous studies suggest that maximum displacement (D_{max}) and fault length, L, are related to one another by:

$$D_{max} = \gamma L^c, \quad (1)$$

where γ is a constant dependent on rock type and regional stresses (Cowie and Scholz, 1992b) and c is the scaling exponent. In scenarios where faults are isolated, the scaling exponents was found to be near unity, whereas the effect of fault linkage or restriction at depth resulted in lower exponents. Previous studies on faults have revealed D_{max}/L (γ) ratios of ~0.001-0.05 (Muraoka and Kamata, 1983; Walsh and Watterson, 1987; Krantz, 1988; Opheim and Gudmundsson, 1989; Peacock and Sanderson, 1991;Cowie and Scholz, 1992a; Dawers et al., 1993; Cartwright et al., 1995; Dawers and Anders, 1995; Clark and Cox, 1996; Watters et al., 2000; Mansfield and Cartwright, 2001; Schultz and Fossen, 2002; Schultz et al., 2006; Polit et al., 2009; Watters and Johnson, 2010; Gudmundsson et al., 2013; Roggon et al., 2017).

Grabens on the Moon

The majority of grabens on the Moon occur along the periphery of the lunar maria (Fig. 2.2A) (Golombek and McGill, 1983; Watters and Johnson, 2010; Nahm, 2016;), but they are also found in floor-fractured craters (Schultz, 1976; Jozwiak et al., 2015; Jozwiak et al. 2012;), in large impact basins (Wilhelms et al., 1979; Nahm, 2016), and on very local scales (Watters et al., 2000; Watters and Johnson, 2010; French et al., 2015). Grabens occur in a variety of terrains including basaltic mare, anorthositic highlands, and in mare-highland transitions. The majority of grabens analyzed in this study is found at the mare-highland transitions and Schrödinger basin (Fig. 2.2B-C).

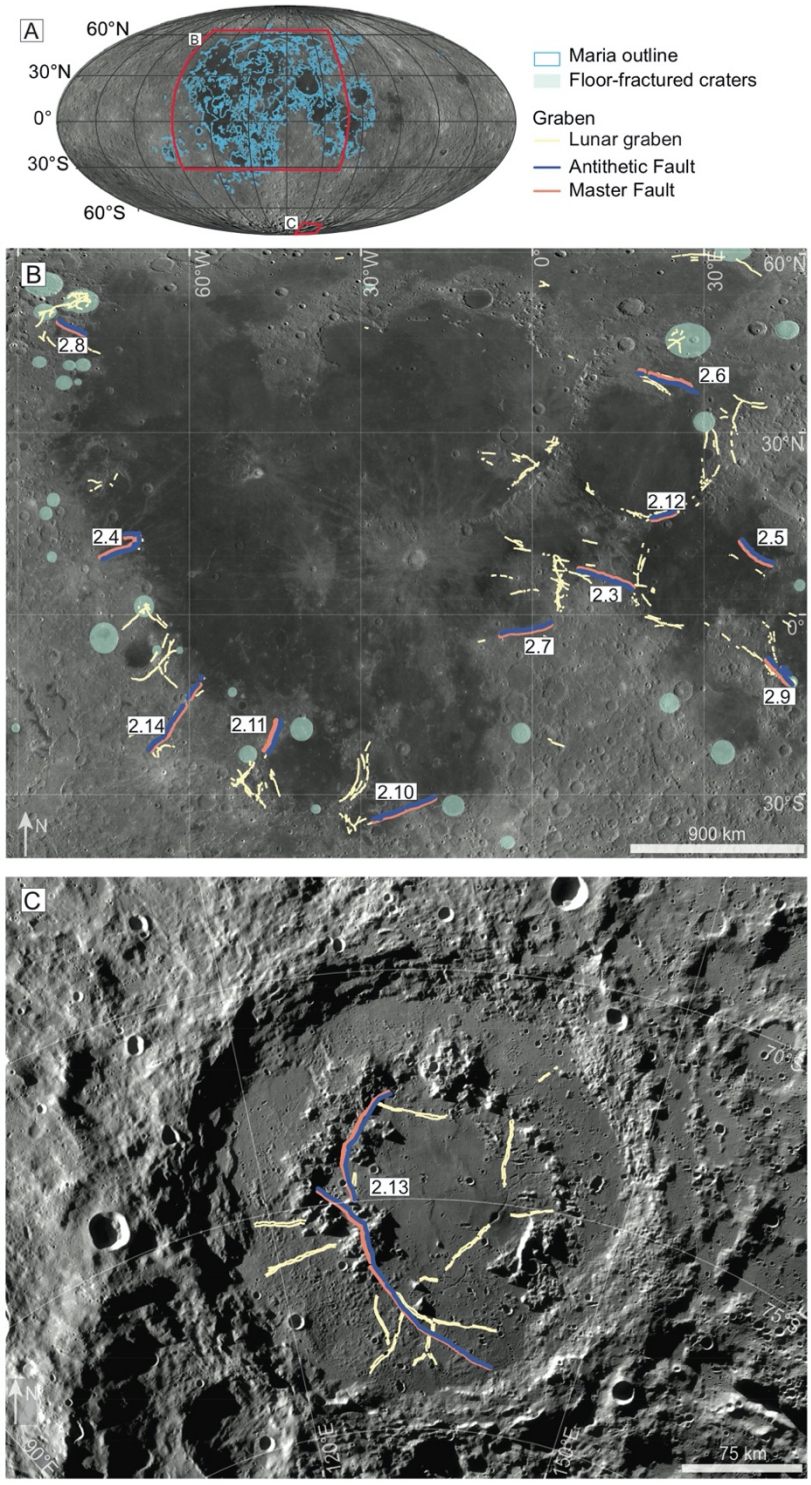

Figure 2.2 Overview of the study areas. (A) Location of the subset images (red outline) relative to the maria on the lunar nearside (blue outline). (B) Lunar Reconnaissance

Orbiter Camera (LROC) mosaic in equirectangular projection showing all individual grabens locations mapped (yellow lines). Our specific study sites around the lunar maria highlight the master (orange line) and antithetic (blue line) graben-bounding faults. Individual figures (labeled in white boxes) can be found in the Supplementary Material. Floor fractured craters containing grabens are distributed widely (green shading). (C) LROC mosaic in south polar orthographic projection of Schrödinger basin with mapped graben.

Large-scale lunar grabens have not yet been systematically investigated for their along-strike characteristics in order to fully understand their geomorphologic expressions. Our investigation examines these relationships and thus reveals growth mechanisms involving fault linkage and interaction and what their displacement-to-length scaling relationships are. Previous studies have investigated smaller lunar grabens for geomorphological patterns (Watters and Johnson, 2010) and an in-depth study of an isolated lunar normal fault has been conducted (Nahm and Schultz, 2013). Theoretical D_{max}/L ratios for lunar faults are predicted to scale at 0.001 due to the influence of the low lunar surface gravitational acceleration (Schultz et al., 2006). None of these previous studies have considered the slip distributions, D_{max}/L scaling, or overlap-to-spacing relationships of normal faults in large and segmented grabens systems.

Graben formation on the Moon has been a long-standing topic of discussion, and it has been suggested that their formation may be linked to the intrusion of dikes (Head and Wilson, 1993; Wilson et al., 2011; Klimczak, 2014) or due to extension along

mascon basins (Solomon and Head, 1979; Freed et. al. 2001). The methodology used in this research does not directly allow us to distinguish among graben formation mechanisms, but instead enables us to characterize the growth of the graben-bounding faults with implications for mechanical properties of the lunar lithosphere. For that, we present a detailed examination of 14 different graben systems (Fig 2B). Slip distributions were generated for these grabens by measuring and plotting the displacements along the lengths of both graben-bounding faults. Slip distributions that incorporate both graben-bounding faults reveal maximum displacements, allow for comparison of displacements between the two opposing faults and thus assessments of graben symmetry. The overall shapes of slip distributions are also useful for understanding subsurface geology or fault interaction. The well-exposed and preserved graben-bounding faults allow us to use D_{max}/L scaling to interpret fault evolution and investigate the possibility of multiple graben fault populations.

Materials and methods

Graben-bounding normal faults in this study were identified using a combination of the Lunar Reconnaissance Orbiter Camera (LROC) global mosaic with a resolution of 100 meters/pixel and the 118 meters/pixel digital elevation model (DEM) from LOLA (e.g. Fig. 2.3A). Throw measurements obtained from the LOLA DEMs were manually extracted in ArcGIS 10.2 using the 3D Analyst toolbox.

Mapping of faults and fault segments was conducted in several stages. The first stage consisted of identifying and mapping fault traces and was followed by the extraction of elevation data along the normal fault traces (Fig. 2.3A, B). In order to collect accurate and coherent data, geodetic fault lengths were measured along the map

trace of the fault, terminating in the fault tips. If graben-bounding faults appeared in several en echelon faults we measured the length and trace of all interacting faults. When en echelon fault segments met in an overlap (Willemse, 1997) we discontinued the fault trace and mapped two individual faults. In cases where grabens were superposed by impact craters or pits, fault traces were terminated, and a new segment was started. When the fault was superposed by features such as ejecta blankets, we mapped the fault as inferred. All geologic features were mapped at the highest resolution of the data. Figure 2.3B shows an example of one of the resulting structural maps with all geologic features considered. Once mapping was complete the map patterns were interpreted for fault growth.

We extracted topographic profiles (Fig. 2.1) from the LOLA DEMs across each of our studied grabens in evenly spaced intervals (see position of one such topographic profile in Fig. 2.3A). The interval of spacing of profiles was determined based on fault length in order to create a consistent representation each fault segment. On average, these profiles were spaced in 2–5 km intervals, with larger intervals ranging up to 8 km and the smallest segments having profiles spaced at <1 km intervals. Topographic profiles ranged in length from 20 to 30 km to ensure that graben topography and local topographic variations would be appropriately identified. For each profile, we identified the locations of graben-bounding faults (Fig. 2.1) to determine their throw. Throw measurements can be converted into the true fault displacement knowing the slip direction and fault dip. We assumed fault motion to be pure dip slip and fault dips to be 60°.

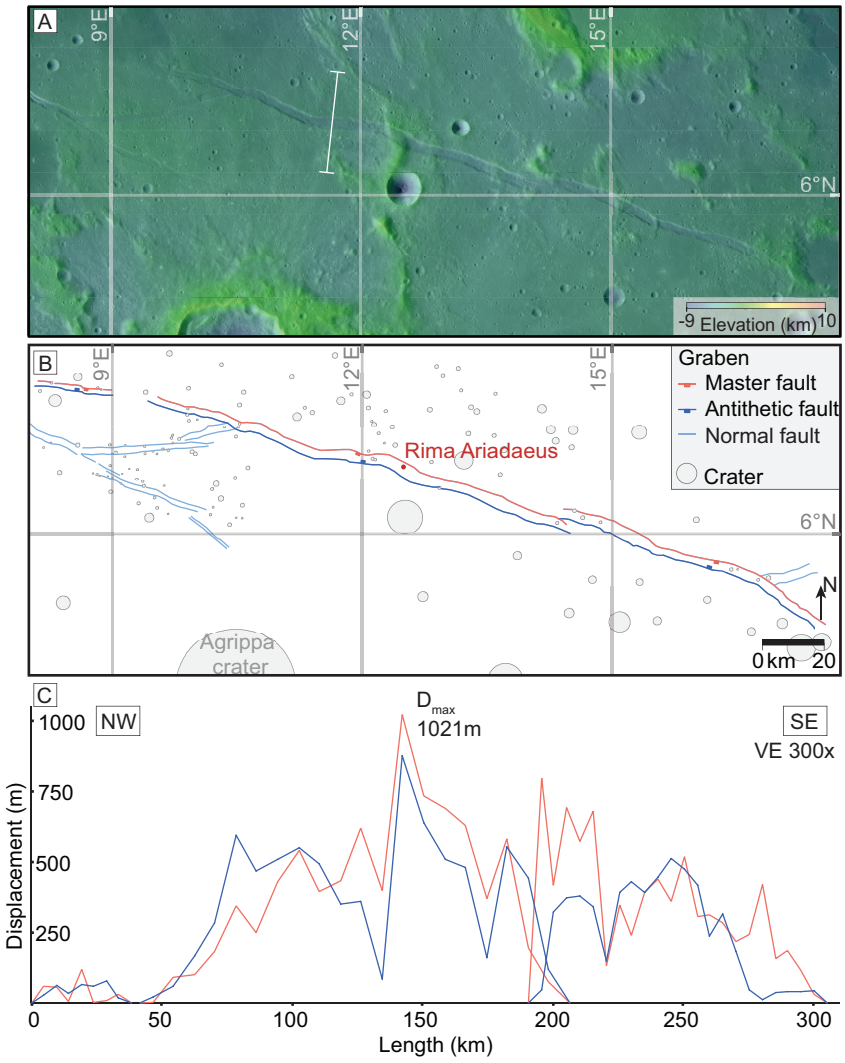

Figure 2.3 Structural analysis of Rima Ariadaeus centered at 12°N, 007°E. (A)The LOLA DEM overlaid on LROC global mosaic in equirectangular projection shows the extent of the grabens and individual faults. The white line indicates where part of the topographic profile shown in Figure 1 was extracted. (B) The structural map of the region shown in (A) highlights six individual fault segment traces and surrounding features. We produced structural maps based on this methodology for all 14 graben systems. (C) Topographic profiles were then used to create slip distributions along-strike of the grabens. The

interpreted slip distributions for this graben reveal a peak in displacement at the center of the graben length. The legend presented here applies to all figures in chapter 2.

Finally, slip distributions for each graben were derived by plotting the calculated true displacement along the map trace for each graben-bounding fault segment (Fig. 2.3C). We also determined the master and antithetic faults for each graben system (Fig. 2.1) and assessed the amount and location of the displacement maximum along the slip distribution (Fig. 2.3C). We assigned the master fault upon visual inspection of our slip distributions to the fault with the maximum displacement along the total graben fault trace (Fig. 2B, C; Fig. 2.3B, C). When maximum displacements were too similar for both graben fault traces, we assigned the master fault to the fault with the higher displacement average. Both, the maximum displacement and length values for each fault segment were extracted from the data for our fault scaling analysis.

Results

Map patterns and slip distributions

Similar to previous studies (Wilhelms et al., 1979; Watters and Johnson, 2010; Nahm, 2016), we surveyed the LROC basemap and mapped all grabens that could be clearly identified on the scale of this dataset. We found that lunar grabens are commonly segmented, and a total of 1800 normal fault segments were recognized and mapped in this study. From this population, we then selected 14 different study sites, for detailed characterization of the graben-bounding normal faults. The grabens investigated in this study are summarized in Table 1. These grabens include Rima Ariadaeus (Fig. 2.3), Rima

Cardanus (two structures, Fig. 2.1), Rima Cauchy (Fig. 2.5), Rimæ Daniell (Fig. 2.6), Rima Flammarion and Oppolzer (Fig. 2.7), Rimæ Gerard (Fig. 2.8), Rima Goclenius (two structures) (Fig. 2.9), Rima Hesiodus (Fig. 2.10), Rima Mersenius (Fig. 2.11), Rimæ Plinius (Fig. 2.12), the graben in Schrödinger Basin (Fig. 2.13), and Rimæ Sirsalis (Fig. 2.14).

The grabens presented in this study display a wide range of map patterns and morphologies and cannot be classified into specific populations based on their structural characteristics. In the following, we first explain our observations in detail for each graben and will then summarize overall observations and findings on the slip distributions from topographic measurements.

Table 2.1 Grabens analyzed for this study.

Graben	Location	Terrain type	Graben trend	Length (km)	D_{max} (m)	Master fault scarp	Max graben width (km)	Graben Symmetry	Fault seg-ments (total)	*Fault segment lengths (km)*	*Slip distribution profile*	D_{max}/L ratio
Rima Ariadaeus	12°N, 007°E	Highlands	WNW/ ESE	304.8	1022.0	south-dipping	5.4	Symmetric	6	29 - 162	Peaked	0.0034
Rima Cardanus 1	13°N, 069°W	Transition	E/W	72.5	168.5	north-dipping	2.5	Symmetric	2	72.5	Plateaued	0.0023
Rima Cardanus 2	11°N 071°W	Transition	SW/ NE	223.2	302.5	south-dipping	2.8	Symmetric	10	25 -104	Plateaued	0.0014
Rima Cauchy	10°N, 038°E	Mare	NW/ SE	204.8	200.2	north-dipping	2.7	Asymmetric	20	9 - 44	Peaked	0.0010
Rimæ Daniell	38°N, 45°E	Transition	NW/ SE	264.7	272.4	south-dipping	3.5	Asymmetric	32	3 – 32	Unclassified	0.0010
Rima Flam. & Opp.	02°S, 001°W	Highlands	WSW/ ENE	282.9	313.5	north-dipping	3.3	Symmetric	9	10 -166	Plateaued	0.0011
Rimæ Gerard	46°N,080°W	Transition	NW/ SE	115.3	538.3	north-dipping	2.2	Symmetric	4	18 - 97	Plateaued	0.0047
Rima Goclenius 1	08°S, 043°E	Mare	NW/ SE	179.3	291.4	north-dipping	3.3	Variable	22	3 - 43	Unclassified	0.0016
Rimæ Geoclenius 2	09°S, 044°E	Mare	NW/ SE	42.9	127.5	north-dipping	2.0	Asymmetric	6	6- 19	Peaked	0.0030
Rima Hesiodus	31°S, 022°W	Transition	NE/ SW	303.7	381.4	north-dipping	4.7	Symmetric	30	4 - 91	Plateaued	0.0013
Rimæ Mersenius	19°N,046°W	Transition	NNE/ SSW	173.0	348.7	east-dipping	3.4	Symmetric	5	28 - 112	Plateaued	0.0020
Rimæ Plinius	17°N, 023°E	Transition	WNW/ ENE	121.2	388.9	north-dipping	3.4	Asymmetric	2	121.2	Peaked	0.0032
Schrödinger graben	75°S, 128°E	Basin	NNW/ SSE	234.1	1115.2	east-dipping	3.7	Variable	8	9 - 106	Plateaued	0.0048
Rimæ Sirsalis	16°S, 059°W	Transition	SW/ NE	453.3	752.6	west-dipping	4.1	Variable	28	3 – 90	Unclassified	0.0017

In-depth analysis of study areas and slip distributions

Rima Ariadaeus

Rima Ariadaeus (Fig. 2.3A), a graben centered at 12°N, 007°E is part of the highlands bound by Mare Vaporum and Tranquillitatis. Rima Ariadaeus is a linear graben striking WNW/ESE and has a total length of 304 km with the average width ranging from 2 – 4 km. The graben crosses a near-perpendicular ridge at the near-center of the fault scarp. This graben system is composed of three fault segments on each graben-bounding side (Fig. 2.3B) with individual six fault segment lengths ranging from 29 km to 162 km. Two antithetic normal faults in the northwestern portion of Rima Ariadaeus are spaced slightly apart from the main fault segments (Fig. 2.3B). The antithetic faults to the southeast overlap in the center region of the graben.

The measured structural relief that informs our interpretation of slip distribution (Fig. 2.3C) reveals a clear displacement maximum of at the center of the slip distribution. This maximum fault displacement is 1021 m, located on the northern fault scarp (master fault). Graben-bounding faults in the northwest show low displacements, whereas the segments in the center and southeast of the structure show much higher slip distributions. Each segment is peaked towards the center of the fault segment, except when soft-linked faults interact, resulting in a skewed slip distribution. This slip distribution displays maximum displacement is at the center of the fault length and tapers towards the tip, and also highlights the interaction between soft-linked fault segments. The displacements for antithetic and master faults remain similar through the graben length indicating that this symmetric graben is mature.

Rima Cardanus

Rima Cardanus (Fig. 2.4), located on the western edge of Oceanus Procellarum is centered at 13°N, 069°W and is located at the transition between lunar highlands and the maria. This graben system is characterized by two near-perpendicular grabens and was mapped as two separate graben systems, Rima Cardanus 1 and Rima Cardanus 2. Rima Cardanus 1 (Fig. 2.4B) strikes generally E/W and has a total length of 73 km with a graben width of 1 – 2 km.

Rima Cardanus 1 consists of two single oppositely dipping normal faults. The southern fault scarp is crosscut by the main graben system from the south, whereas the northern scarps remains intact. The northern-dipping graben scarp was determined to be the master fault and the southern-dipping scarp its antithetic fault.

Rima Cardanus 2 (Fig. 2.4B) strikes from a linear graben in the southwest to a semi-arcuate graben in the northeast and then is sharply truncated by the respectively much shorter and perpendicular Rima Cardanus 1. Generally striking SW/NE the graben-bounding faults change orientation to N/S towards the other graben system centered above it and terminates in the southern fault scarp. Rima Cardanus 2 is centered at 11°N 071°W and has a total length of 223 km. Each graben bounding side hosts a large subset faults segment. The average fault segment lengths range from 25 to 104 km. In this main graben system, the master fault is south-dipping and the antithetic counterpart is north-dipping.

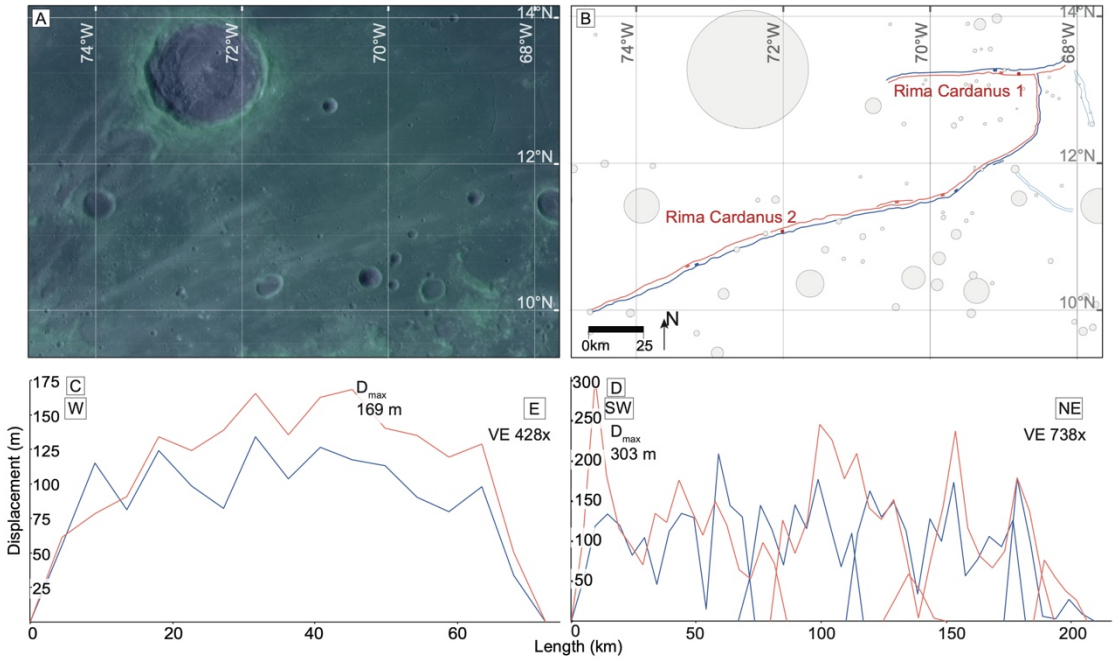

Figure 2.4 Structural analysis of Rima Cardanus centered at 69°N, 013°W. (a) A LOLA DEM draped over LROC global image mosaic shows the study area in equirectangular projection. (b) Structural map of region shown in (a). This map reveals two major graben systems, Rima Cardanus 1 and Rima Cardanus 2. (c) The slip distribution for Rima Cardanus 1 shows a displacement with a plateaued shape. (d) Rima Cardanus 2 has a slip distribution with a maximum peak at the southwestern fault tip.

The interpreted slip distributions for the two graben vary greatly (Fig. 2.4C-D). The slip distribution for Rima Cardanus 1 does not have a pronounced peak but a maximum displacement of 169 m on the southern fault scarp was measured (Fig. 2.4C). Master and antithetic displacements values are similar for this graben, displaying a symmetric graben profile. The slip distribution for the larger fault, Rima Cardanus 2 (Fig.

2.4D), indicates a much more complex picture. Generally, the slip distribution appears fairly flat, offset by a large peak near the southwestern fault tip. The maximum displacement here is 303 m and only occurs along the northern fault. The remainder of the slip distribution shows several lower peaks. If individually interpreted nearly all fault segments display peaked profiles, where the longest fault in the center of the graben system has a maximum displacement of 246 m. The southwestern fault segments along Rima Cardanus 2, show an increase in displacement, indicating interaction and possible linkage with the previous fault. These slip distributions show evidence of linkage as well as flattened shapes and symmetric graben-bounding indicating a mature graben. Master and antithetic values in Rima Cardanus 2 are similar, indicating symmetry between both graben-bounding faults.

Rima Cauchy

Rima Cauchy (Fig. 2.5), located within the eastern margin of Mare Tranquillitatis, is centered at 10°N, 038°E and generally strikes NW/SE. Rima Cauchy has a total length of 204 km and an average width of 2 km. Few small craters cut across graben segments but further leave the structure undisturbed. Rima Cauchy consists of 10 fault segments on each graben-bounding side (Fig. 2.5B). The center of the graben system shows several en echelon soft-linked fault segments, as well as one hard-linked segment on the northern fault scarp. Fault segment lengths range from 9 to 44 km in length and are highly variable across the graben. The graben is linear in the southeast and curvilinear in the northwest.

Throughout the entire graben system, the master fault is north-dipping and the antithetic fault is south-dipping.

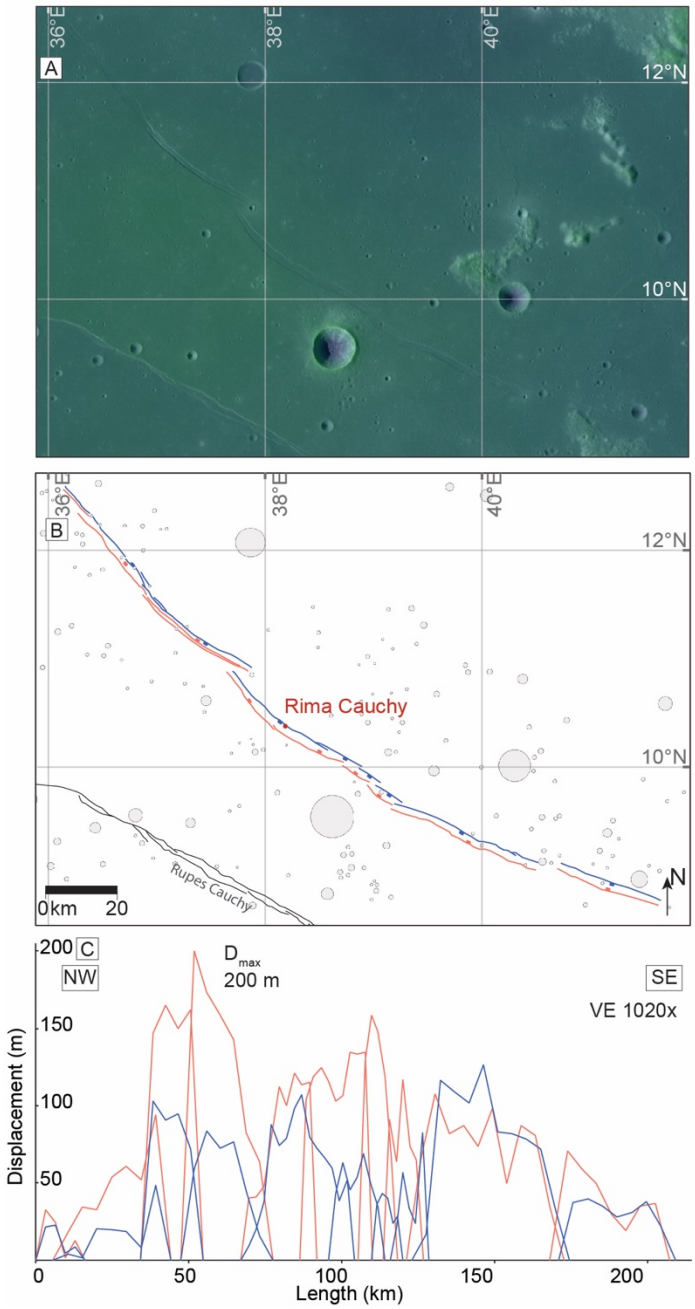

Figure 2.5 Structural analysis of Rima Cauchy centered at 10°N, 038°E. (A) An equirectangular projection of a LOLA DEM draped over LROC global image mosaic

shows the fault scarps of Rima Cauchy. (B) The corresponding structural map shows abundant, interacting fault segments. (C) The slip distribution for Rima Cauchy shows several high displacement peaks toward the center of the fault length.

The interpreted slip distribution for Rima Cauchy (Fig. 2.5C) shows a maximum displacement of 200 m along the southern fault scarp (master fault). Displacement clearly tapers towards the fault tip and peaks towards the fault trace center. The fault segment to the west of the peak also shows a relatively high displacement and represents an en echelon, interacting fault. Each of the individual profiles peak near the center of the fault segment length. Between fault length 100 to 130 km the displacement at individual fault tips is high (Fig. 2.5C) and skewed towards en echelon faults, suggesting soft-linkage between faults. Master and antithetic faults are predominantly asymmetric in the northwest and symmetric in the southeastern portion.

Rimæ Daniell

Rimæ Daniell is a large graben system in the transitional terrain between Lacus Somniorum and Mare Serentatis (Fig. 2.6A). The subset of graben selected for this study system strikes linear in the southeast and northwest and is joined in the center by a slightly curved graben. Generally, Rimæ Daniell (Fig. 2.6B), strikes NW/SE and has a total length of 264 km with a range in width of 2 to 3 km. The north-dipping scarp is host to 18 individual fault segments and the south-dipping scarp consists of 14 fault segments.

The graben turns into a single normal fault towards the southeast (Fig. 2.6B). The center of the graben is host to abundant soft-linked en echelon faults.

The interpreted slip distribution for Rimæ Daniell shows high displacement peaks near the graben fault tips and respectively lower displacement along the center of the fault trace (Fig. 2.6C). The maximum displacement found along the western segment is along the scarp is 272 m, whereas the smoother, mare terrain generally exhibits lower displacements. Areas with increased fault segment soft-linkage show increases in displacement at the fault tips near the fault overlap and are evident in the slip distribution at length positions 100, 130, 160 and 200 km. A total of 22 individual fault segments display a symmetric peaked shape. The very southeastern fault has also a high displacement, similar to the first fault segment in this graben system.

The master fault is south-dipping along the analyzed graben. The antithetic fault scarp distribution is asymmetric, and the peak skewed towards the southeast. The master fault is also asymmetric, and its peak is skewed towards the northwest. This relationship results in a highly asymmetric slip distribution. Both graben-bounding faults also show large discrepancies in their relative offset, when the master fault displacement is high, the corresponding antithetic fault has a much lower displacement and vice versa. The southeastern fault represents the only half-graben in this study.

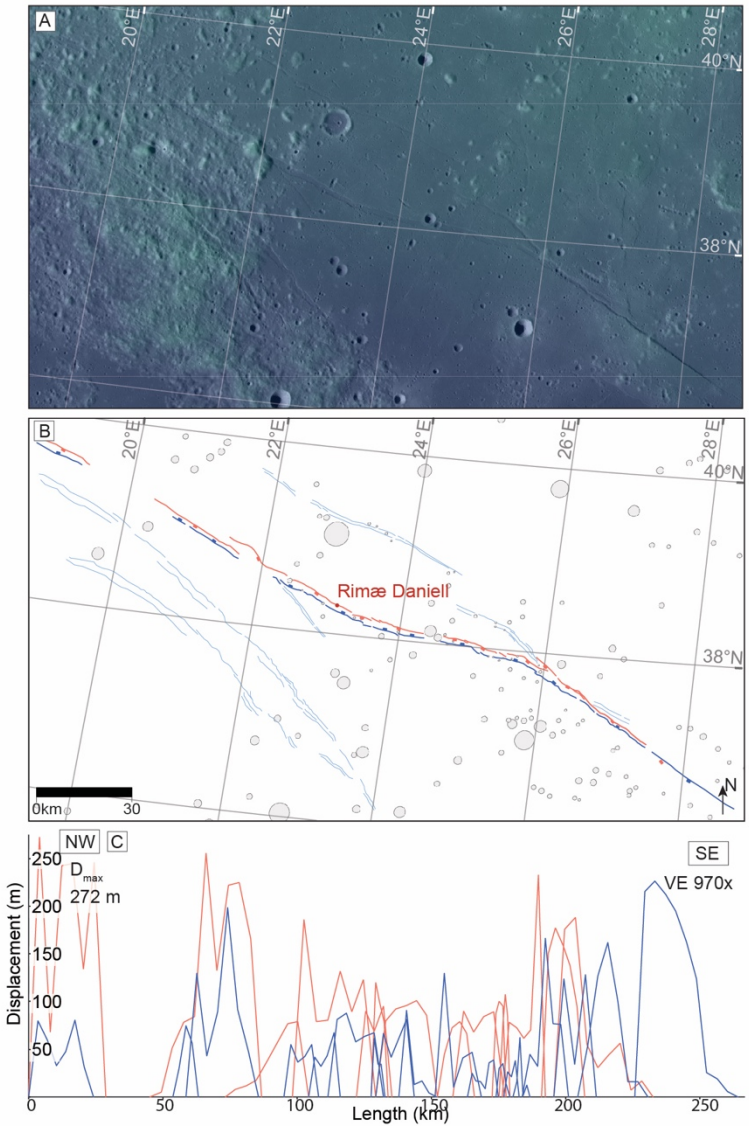

Figure 2.6 Structural analysis of Rimæ Daniell centered at 38°N, 045°E. (A) LOLA DEM draped over LROC global image mosaic in north polar orthographic projection. (B) The corresponding structural map of the region reveals the specific graben examined in this study where the master fault is the south-dipping scarp. (C) Slip distributions for this

graben show high displacement along rough terrain (west) and in locations where fault interactions have occurred (east).

Rima Flammarion and Rima Oppolzer

The next graben study site is composed of two different graben systems, Rima Flammarion in the west and Rima Oppolzer in the east (Fig. 2.7A). This study site is located in the highlands at the base of Sinus Medii and generally strikes WSW/ENE. These two graben have been previously interpreted as two individual graben (Arthur et al., 1963) but our mapping with LRO data indicates that they are part of one continuous graben which is spatially separated by rugged terrain and a crater. This higher resolution imagery revealed a fault traces that could be traced throughout the rugged terrain and clearly linked both individual faults. The entire length of both graben combined is 283 km.

Rima Oppolzer, which is truncated in the west by the 6.3 km diameter crater, Flammarion W, has a total length of 230 km. Each graben-bounding segment has 5 fault scarps ranging in length from 10 to 166 km in length. Generally, fault segments underlap along Rima Oppolzer, while a hard-linked segment is visible in the south-dipping Rima Flammarion. Rima Flammarion, which is truncated in the east by rough terrain, has a total length of 42 km. This graben consists of three individual fault segments with lengths ranging from 10 – 42 km. Rima Flammarion additionally shows a small overlap in fault

segments along the north-dipping scarps. The master fault for these two graben is north-dipping, while the antithetic fault is south-dipping.

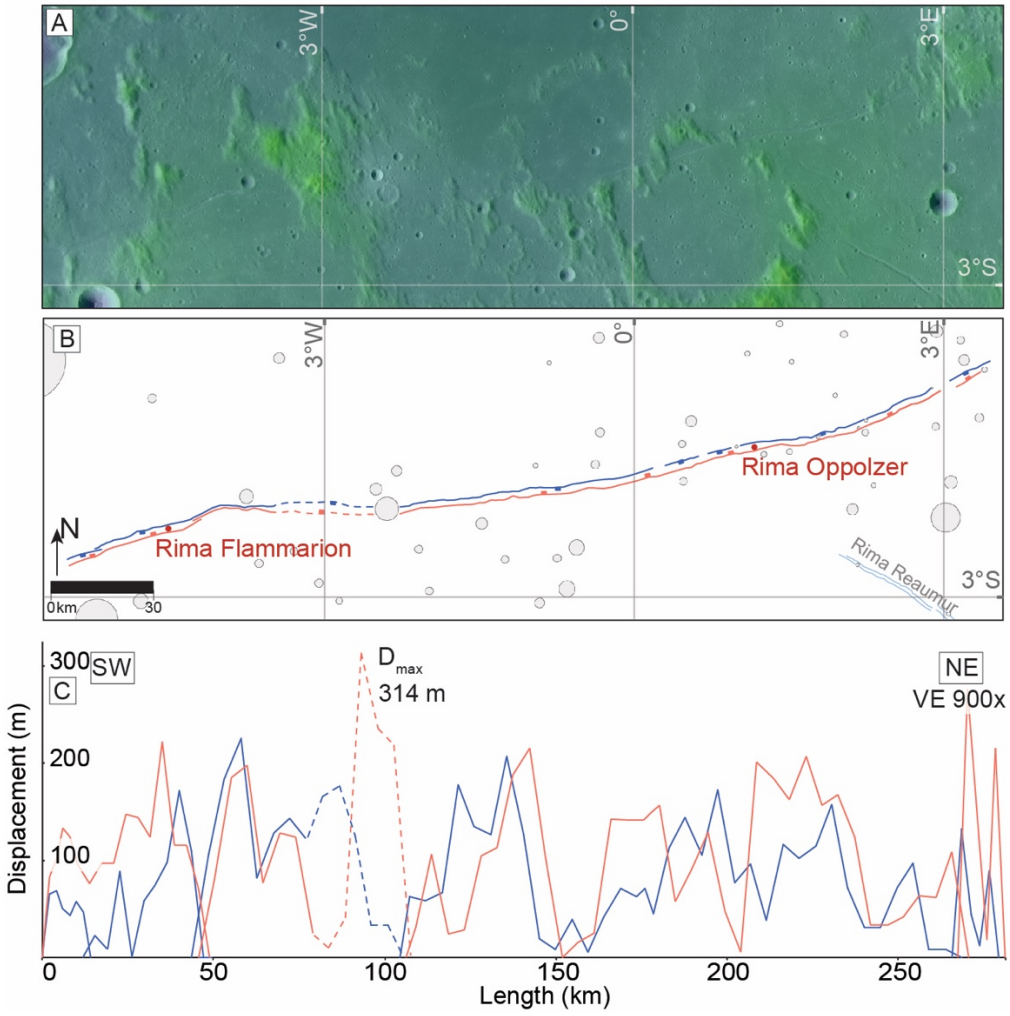

Figure 2.7 Structural analysis of Rimæ Flammarion and Oppolzer. (A) LOLA DEM draped over LROC global mosaic image (equirectangualr position) here shows highland terrain with rough terrain and cratering. (B) Structural map of region shown in (A).The structural map of Rima Flammarion and Rima Oppolzer, together centered at 02°S, 001°W. Rima Flammarion fault segments show two overlaps whereas Rima Oppolzer has

four underlapped fault segments. (D) The slip distribution of both graben show a nearly continous average displacement with only one large peak.

The interpreted slip distribution for Rima Flammarion and Rima Oppolzer has multiple peaks at ~ 200 m (Fig. 2.7B). The maximum displacement of 314 m in this graben system lies along a small ridge, which could account for the slightly higher displacement. The average displacement ranges from 100 to 200 m. Rima Flammarion has a slip distribution that has its highest displacement in the center of the fault trace, but also shows enlarged displacement towards the next fault scarp segment. Rima Oppolzer shows two soft-linked overlaps along the southwest and four instances of underlap along the northeastern graben section. Both graben show increased displacement in soft-linked fault segments near graben length position 50 km. The shape of this graben is symmetric, as evinced by the similar displacements of master and antithetic faults.

Rimæ Gerard

Rimæ Gerard consist of multiple graben near Gerard crater (Fig. 2.8A). Rimæ Gerard considered in this study is centered 46°N, 080°W and lies on the border between highlands and Oceanus Procellarum. Striking NW/SE, this graben has a total length of 115 km. The graben width varies; its widest extent of 2.2 km is in the center of the graben and the narrowest width of less than 1 km in the far southeastern portion. Rimæ Gerard cuts across two highly degraded craters and is crosscut by three small craters in the

northwestern portion of the graben (Fig. 2.8B). It consists of two fault segments on each graben side with lengths ranging from 18 to 97 km.

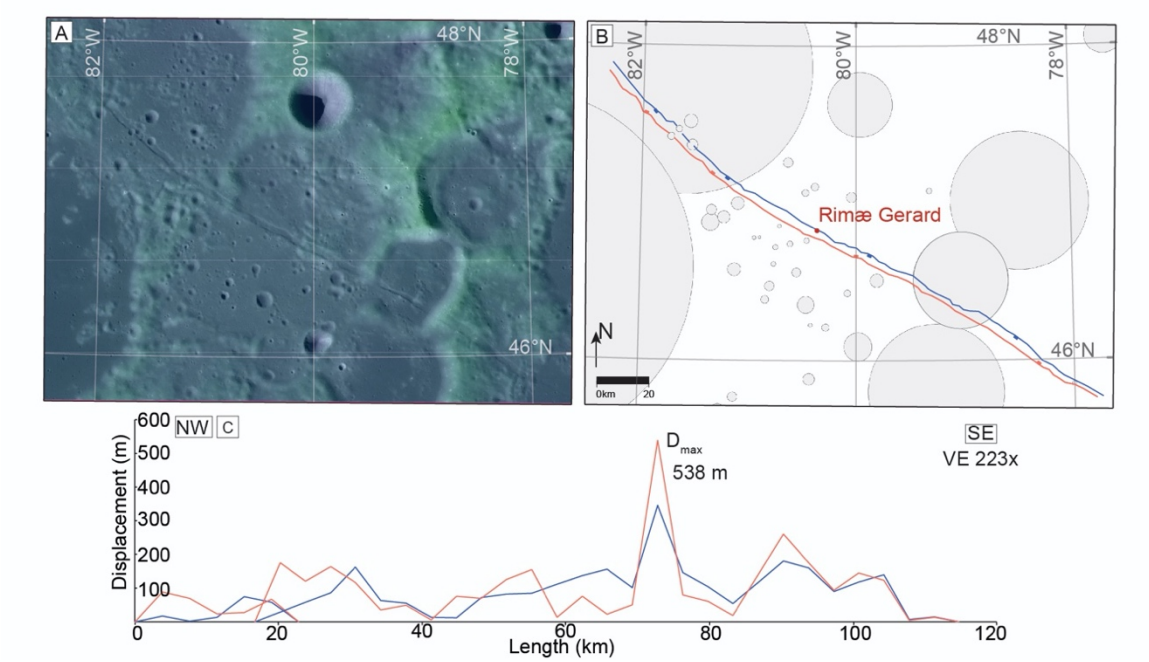

Figure 2.8 Structural analysis of Rimæ Gerard. (A) The LOLA DEM and LROC global image mosaic show the general rough topography around Rimæ Gerard in a north pole orthographic projection. (B) Structural map of region shown in (A). The structural map of the area reveals a north-dipping master and south-dipping antithetic faults cutting across several degraded craters. (C) Rimæ Gerard's slip distribution shows a flat slip distribution with a large peak in the proximity to the fault length center.

The interpreted slip distribution for Rimæ Gerard has one dominant peak (Fig. 2.8C). The remainder of the slip distribution has a much lower displacement and tapers towards the fault tips. The maximum displacement for this graben is 538 m and lies substantially above the average displacement of 94 m for all fault scarps. The peak location coincides with one of the degraded crater rims, which could explain the unusually large divergence between average displacement and maximum displacement. All other segments in this system are plateaued but do not show evidence of interaction or fault linkage. The master fault in Rimæ Gerard is the north-dipping fault scarp. Along Rimæ Gerard, the graben profiles of master and antithetic faults are similar and symmetric displaying a mature graben.

Rimæ Goclenius

Rimæ Goclenius, centered at 08°S, 043°E, are a system of graben bounded by Mare Nectaris to the southwest and Mare Fecunditatis to the northeast (Fig. 2.9A). Both graben studied here are predominantly linear and strike NW/SE. Rimæ Goclenius 1 has a total length of 180 km and an average width of 1 to 2 km. The graben is crosscut by the nearby Gutenberg E crater in its center. The southern graben-bounding fault consists of 12 segments, while the northern fault is comprised of 10 individual fault segments (Fig. 2.9B) ranging in length from 4 to 43 km. The northwestern portion of Rimæ Goclenius 1 shows fault interaction and soft-linkage between graben segments, in contrast to the southeastern graben in which fault segments tend to underlap.

Rimæ Goclenius 2 has a strike parallel to Rima Goclenius 1 but is much shorter, with a total length of 43 km and a maximum width of 2 km. Two south-dipping faults scarps are opposed to 4 north-dipping fault scarps along Rimæ Goclenius 2. This graben shows a higher degree of fault segmentation and linkage, displaying two clearly overlapping fault segments along the graben length.

The interpreted slip distribution for Rimæ Goclenius 1 (Fig. 2.9C) has its maximum displacement skewed towards the southeastern fault tip with a maximum displacement of 291 m. Rimæ Goclenius 1 is right-skewed due to a high amount of fault linkage in that portion of the graben. When individually analyzed, the northwestern portion of this graben is peaked towards the its center. The southeastern region shows five soft-linked en echelon faults, resulting in several large peaks in the slip distribution displaying the result of interacting stress fields.

Rimæ Goclenius 2 shows a similar interpreted slip distribution with a maximum displacement of 128 m (Fig. 2.9D). This graben has several en echelon, soft-linked fault segments resulting in a clear displacement peak at the center of the fault. When analyzed as individual fault segments, interacting faults show higher displacement in regions where faults overlap. Overall both slip distributions are excellent examples of increased displacement in soft-linked, en echelon fault scarps. Both graben have their master fault dipping to the north and antithetic fault scarps dipping to the south. The symmetry for Rimæ Goclenius 1 is not easily assessed but due to the abundant spikes in displacement it is interpreted as variable. Displacement along master and antithetic faults in Rimæ Goclenius 2 clearly reflects an asymmetric cross-section.

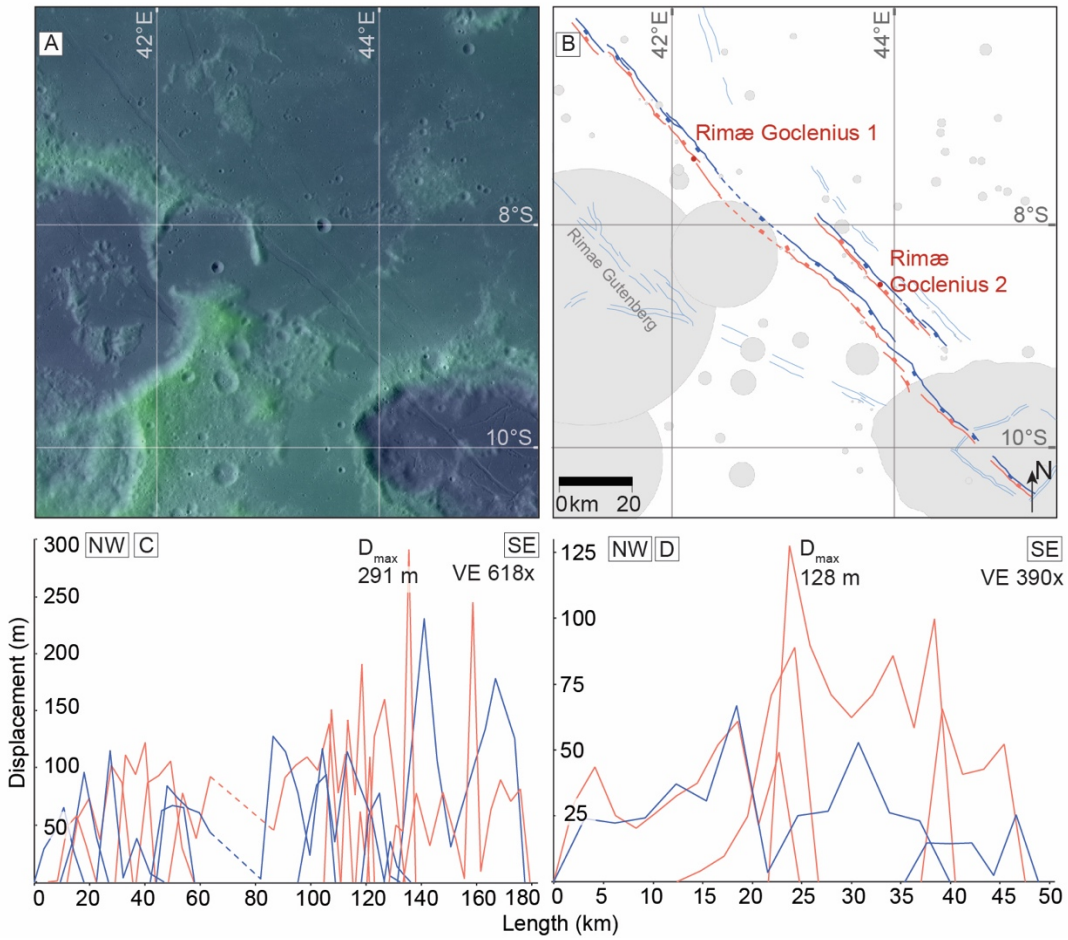

Figure 2.9 Structural analysis of Rimæ Goclenius. (A) The LOLA DEM over LROC global image mosaic in equirectangular projection here shows the general area of a Rimæ Goclenius graben cutting across degraded craters and rough lunar terrain. (B) Structural map of region shown in (A). The structural map reveals two specific graben systems selected for detailed study. (C) The slip distribution for Rimæ Goclenius 1 displays large displacement in the southeastern portion of the graben. (D) The slip distritbution for Rimæ Goclenius 2 has peak near the center of the total fault length.

Rima Hesiodus

Rima Hesiodus, centered at 31°S, 022°W, is located in the mare/highland transition zone south of Mare Nubium. The structure strikes NE/SW and has a total length of 304 km with widths ranging between 2 and 4 km (Fig. 2.10A). The graben mainly deforms mare units, but in its center portion, it cuts through rough terrain (marked in Fig. 2.10 by dashed lines). Its linear map pattern remains unaltered by the terrain change. The faults forming this graben are heavily segmented and display multiple fault overlaps, jogs, and underlaps in fault segment interaction. Each graben-bounding fault scarp consists of 15 fault segments, with fault segment lengths ranging from 4 to 91 km. The master fault is north-dipping throughout the graben system.

Our interpreted slip distribution of Rima Hesiodus shows a generally flat profile but contains a pronounced maximum of 381 m just southwest of the center of the graben. This displacement maximum is only observed on the south-dipping (antithetic) fault and is located near the topographic rise crossing the graben which, indicating the influence of rugged terrain on the slip distribution. The southern and northern scarps have average displacement of 138 and 112 m, respectively.

The observed fault segmentation in the southwestern part of the structure is also evident in its slip distribution in abundant peaked and overlapping fault profiles. Further northeast along the fault trace the interaction decreases and the slip distribution reflects less fault interaction. The lack of jogs or overlaps in the transition between symmetric and asymmetric slip distribution suggests that the more mature southwestern portion developed before the northeastern graben section. The majority of Rima Hesiodus is

symmetric as evinced by the similar displacements along master and antithetic faults; the only sight deviation occurs in the northeastern portion.

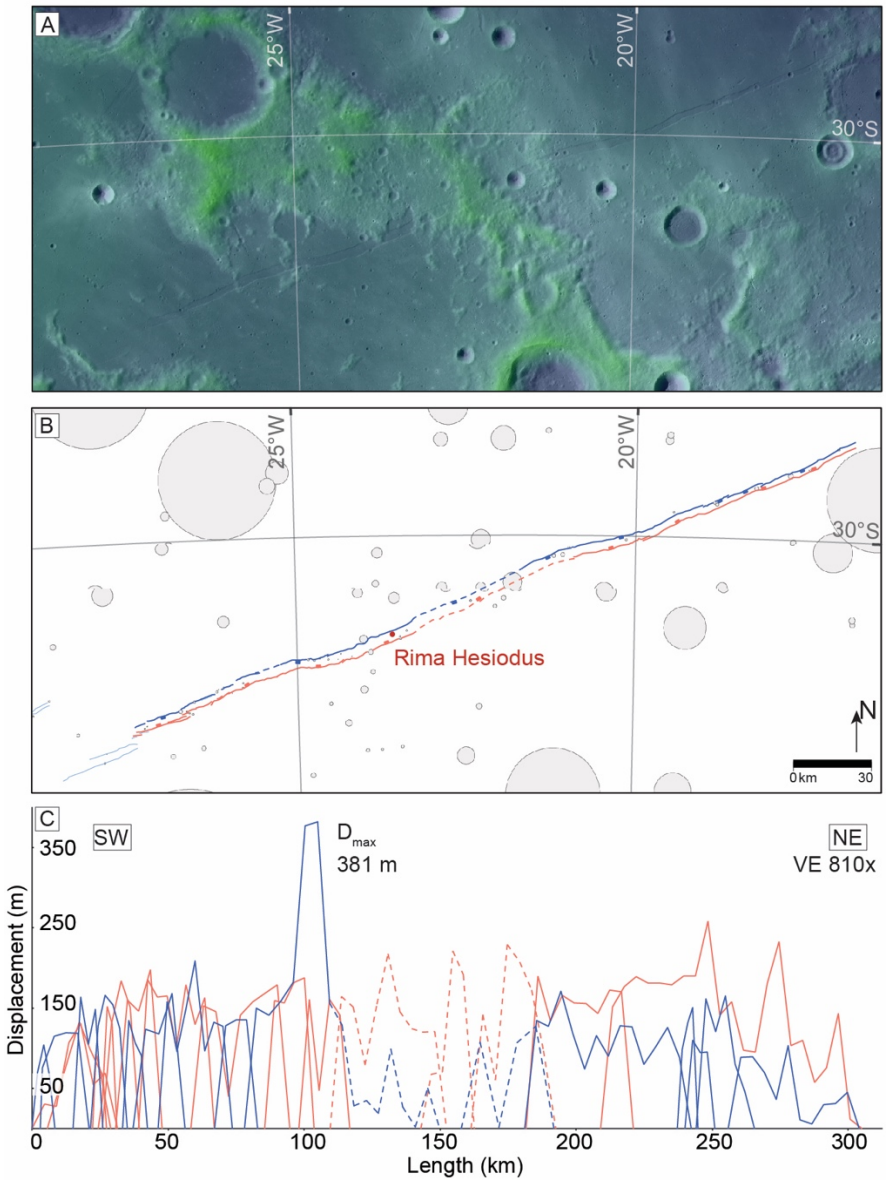

Figure 2.10 Structural analysis of Rima Hesiodus. (A) A LOLA DEM over LROC global image mosaic in equirectangular projection shows the highland-mare transitional topography surrounding this graben. (B) Structural map of region shown in (A) reveals a

north-dipping master and south-dipping antithetic fault. (C) The generally flat slip distribution of this Rima Hesiodus is interrupted by a large displacement peak near rough surface terrain.

Rimæ Mersenius

The western edge of Mare Humorum is host to Rimæ Mersenius, where two well-defined NNE/SSW striking graben are bounded by craters on either graben side (Fig. 2.11A). The total length of this graben system is 173 km and ranges in graben width from 1 to 3 km. The graben cuts across a 14 km diameter crater near the its center and is cut by a 0.4 km diameter crater in the south. We grouped these two graben together into one system, which has two fault scarps on the western side and three segments on the eastern graben side. Individual fault segment lengths range from 27 km to 112 km. The largest overlap of fault segments occurs near the center of the graben and measures 13 km. This graben system has 14 jogs (hard-linked faults), four along the master fault (east-dipping) and 10 along the antithetic fault.

The interpreted slip distribution for Rimæ Mersenius is flat-topped, has a no pronounced displacements peaks, and an average displacement of 181 m (Fig. 2.11C). The maximum displacement of 349 m was measured along the east-dipping scarp is only slightly higher than surrounding peaks. Even though soft-linkage in the form of a large overlap is visible in map view near the center of the graben, this is not evident in the slip distribution. Larger displacement in the southern region can be attributed to higher

regional topography. Displacement values for each graben-bounding fault scarps are not markedly different and lie very close. High symmetry between master and antithetic displacements indicate a well-developed, mature graben profile.

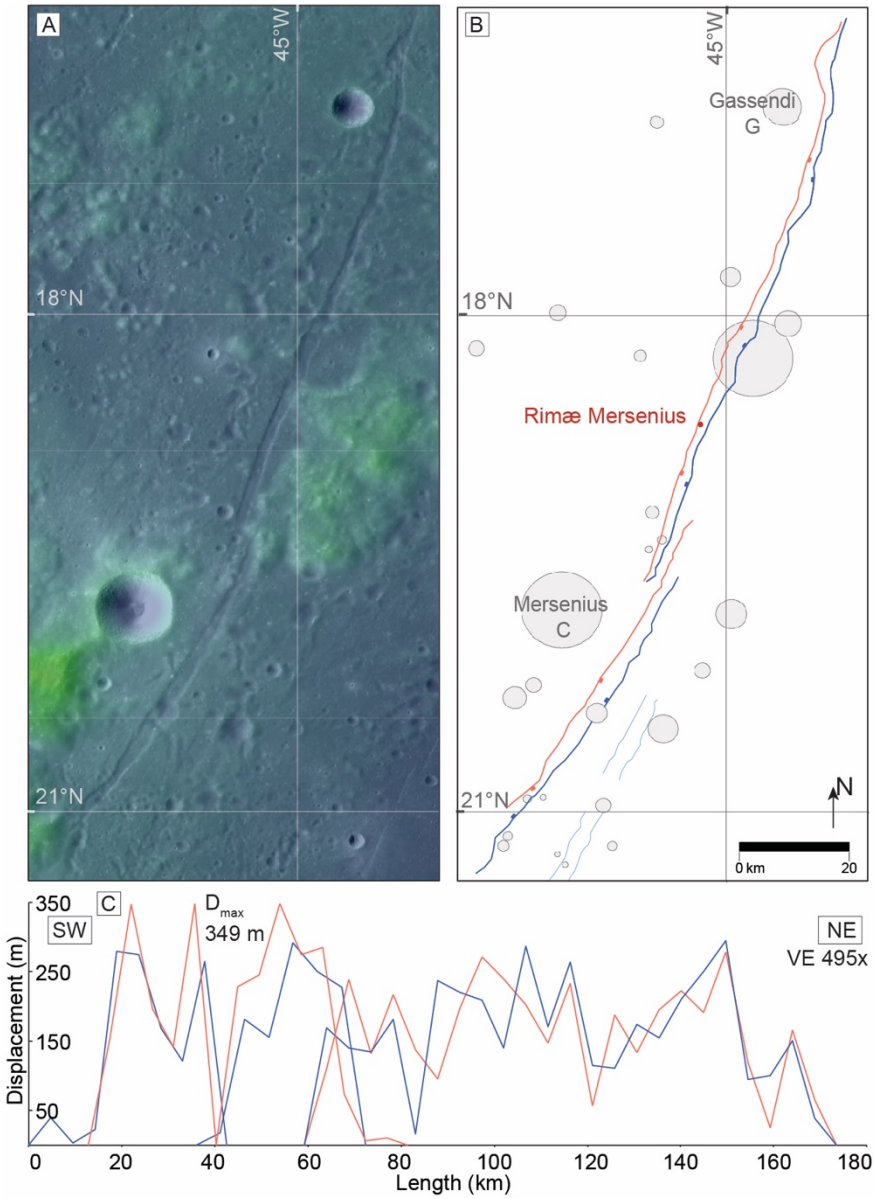

Figure 2.11 Structural analysis of Rimæ Mersenius. (A) LOLA DEM over LROC global image mosaic in equirectangular projection shows the graben centered at 19°N, 045°W.

(B) Structural map of region shown in (A) reveals two overlapping graben systems with a east-dipping master fault and a west-dipping antithetic fault. (C) The corresponding slip distribution is flat-topped and has three minor peaks between the southwestern tip and the center of the fault.

Rimæ Plinius

Rimæ Plinius, centered at 17°N, 023°E, are several curvilinear to arcuate graben located along the southern border of Mare Serenitatis (Fig. 2.12A). We assessed the longest graben of this system, which is surrounded by smooth terrain and is located along a mare/highland transition. This graben strikes WSW/ENE and has a total length of 121 km and a maximum width of 3.4 km. Rimæ Plinius is superposed by a few small (less than 1.4 km diameter) craters. This graben is not segmented and is composed of two antithetic normal faults (Fig. 2.12B). In the southwestern graben region, the graben strike sharply changes to E/W indicating the possibility of previous fault linkage.

The interpreted slip distribution (Fig. 2.12C) for Rimæ Plinius shows several peaks distributed along the master fault. The maximum displacement for Rimæ Plinius is 389 m, located in the western portion of the north-dipping fault. The same region depicts a change in fault strike in map view, indicating that this may have been the location coalescence of graben. This inference is supported by an increase in displacement in both directions away from the change in fault strike. Master and antithetic slip distributions are predominantly asymmetric and only show symmetry between 20 and 50 km.

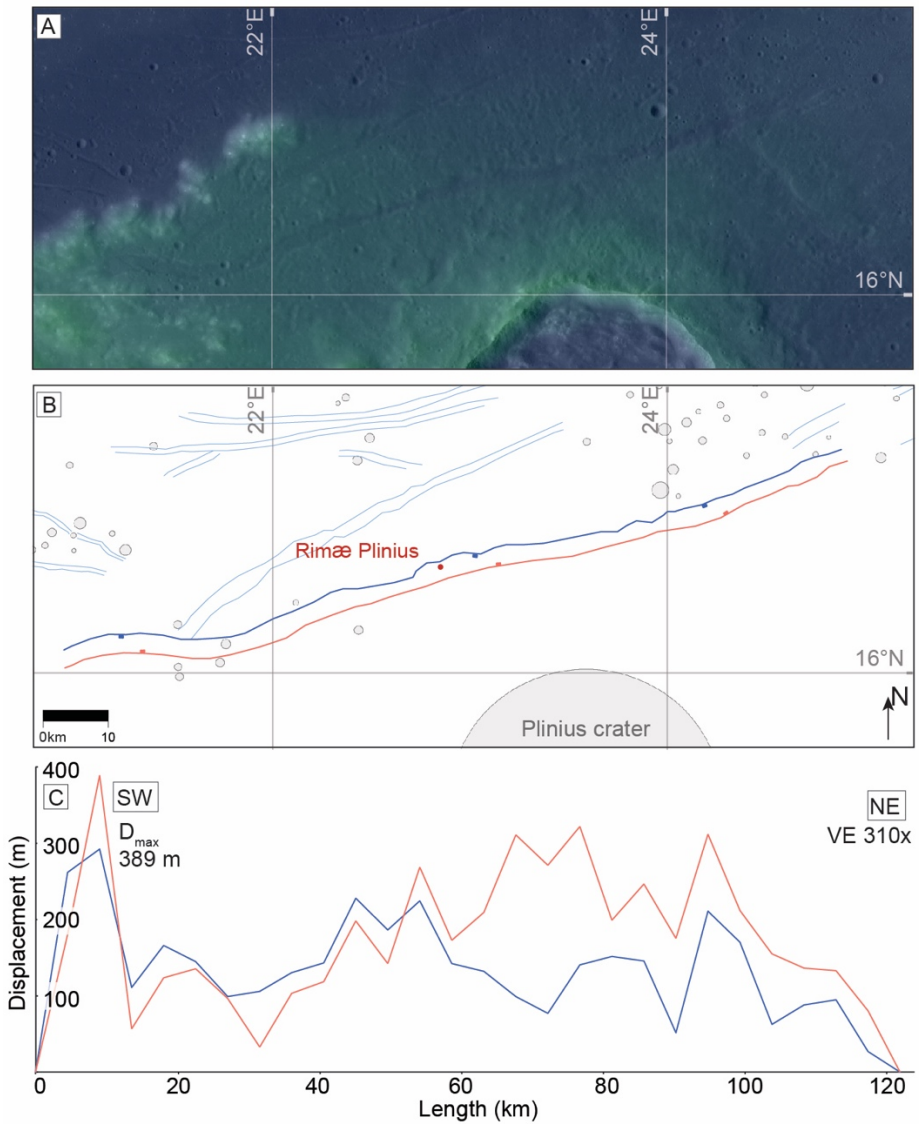

Figure 2.12 Structural analysis of Rimæ Plinius. (A) A LOLA DEM over LROC global image mosaic in equirectangular projection shows a long graben along mare-highland transition zone. (B) The structural map of Rimæ Plinius shows the single master fault north-dipping towards Mare Serentatis. (C) The corresponding slip distributions shows to peaked regions with a local minium near 30 km.

Schrödinger basin

The graben system in Schrödinger basin is located near the south pole on the far side of the Moon and includes the graben at the lowest elevation in this study (Fig. 2.13A). Graben in the basin are radial and concentric to the rim and we selected two NNW/SSE striking graben with semi-arcuate shape to be examined in this study. Parts of our analyzed graben cross through remnants of the central peak. The total length of this graben is 234 km and its width ranges from 1 to 4 km. Several small craters are superimposed on the graben scarps.

The northern graben is arcuate in map view with a total length of 79 km and is oriented circumferentially with respect to the center of Schrödinger basin. The northern graben is not segmented and is composed of two antithetic normal faults. The southern graben changes orientation at its northern tips and strikes linearly NW/SE. The southern graben has a length of 168 km and is composed of two western fault segments and two eastern fault segments.

The interpreted slip distributions for the two analyzed graben in Schrödinger basin displays three large peaks across the graben length (Fig. 2.13C). These peaks occur along the northern tip and surrounding the center of the graben on each side. The observed maximum of 1115 m and average displacement of 690 m are the highest across all our study sites. High displacement peaks coincide with the graben crossing topographically higher regions than its surroundings. The center of the graben system shows the maximum displacement. The master fault was found to be the east-dipping scarp. Displacements on the master and antithetic faults are highly variable and

increasingly differ towards the north (Fig. 2.13C). This suggests that from north to south the graben becomes more symmetric and thus mature.

Rimæ Sirsalis

Rimæ Sirsalis are a set of graben that run radial to the southwestern portion of Oceanus Procellarum that straddles the highlands/mare transition (Fig. 2.14A). Rimæ Sirsalis is the longest graben system in this study with a total length of 453 km. The graben strikes SW/NE and displays width ranges of 2 km to 4 km. This graben is predominantly linear but shows a curved map pattern in its southern portion. The very northeastern tip of the graben system is separated from the main graben area by 32 km. The northeastern portion of the graben is partially covered by ejecta blankets from two large craters, and the same region is superposed by two smaller craters. Along the southern end of the graben system craters and further ejecta material are cut by the faults. This region also displays abundant fault segmentation with several fault scarps overlapping another over their entire lengths. Closer to the northeastern portion, and the mare, we find less fault segmentation and overlap. The individual fault scarp lengths in this graben are highly variable and range from 3 to 90 km.

The interpreted slip distribution for Rimæ Sirsalis shows a picture similar to the graben map trace; the southwestern portion is heavily segmented and shows abundant overlap, resulting in high displacement, especially along the master fault trace (Fig. 2.14C). The first few faults displacements are skewed towards each other indicating linkage between segments. Along this region of the slip distribution the antithetic fault shows a much lower displacement. The remainder of the graben less segmented. Rimæ Sirsalis's maximum displacement of 753 m is found along the west-dipping fault scarp

and has the second highest maximum displacement of this study. Both graben-bounding sides are highly variable in their respective offsets across the graben. The southwestern extent is highly asymmetric and becomes increasingly more symmetric towards the northeast.

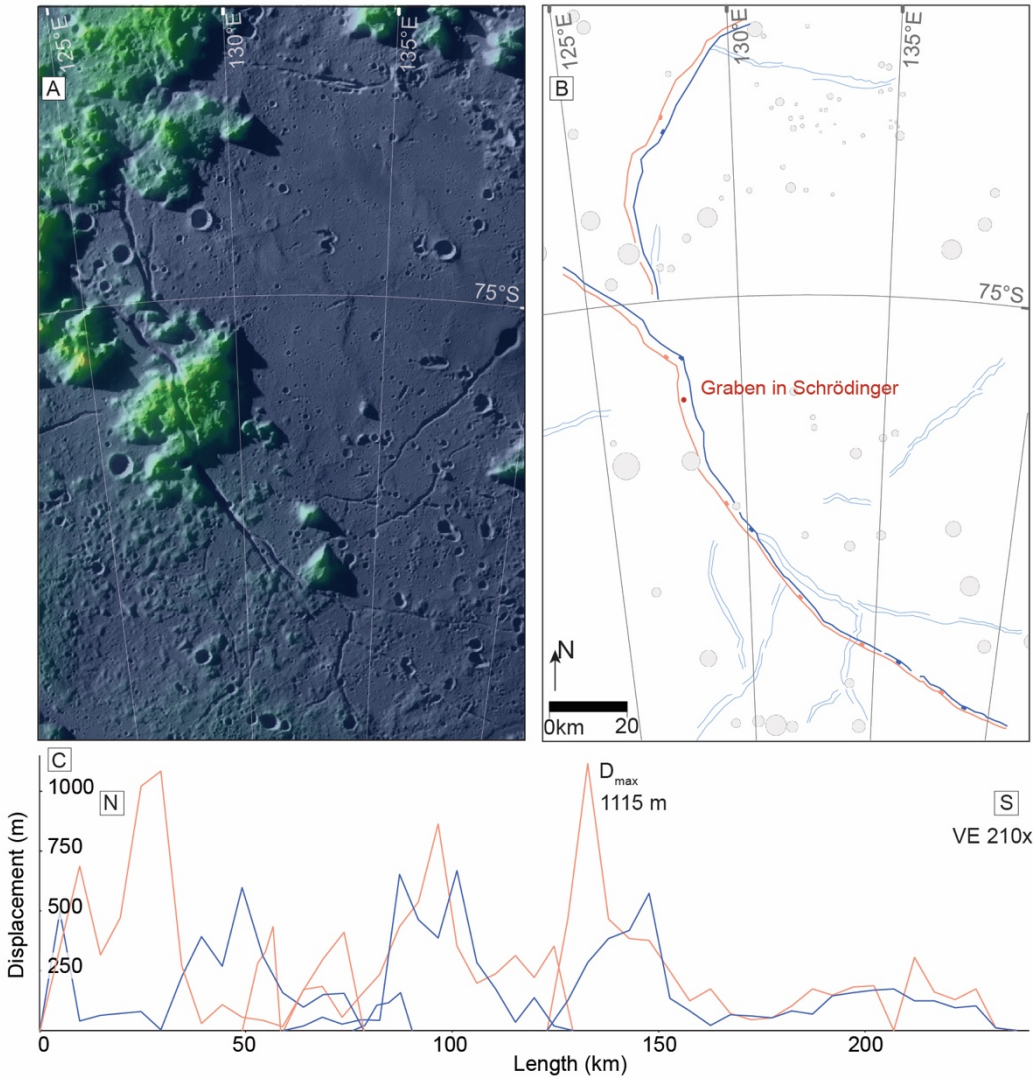

Figure 2.13 Structural analysis of Schrödinger basin, centered at 75°S, 128°E. (A) A LOLA DEM over LROC global image mosaic in polar stereographic projection of the large impact basin Schroedinger shows central peaks and rough basin terrain. (B) The

geologic map shows several arcute and long graben throughout the basin. Some graben cut across rougher terain. (C) The corresponding slip distribution for these graben displays a two high displacement peaks and an otherwhise genereally flattened profile.

Summary of findings

Grabens were found in multiple terrain types (Table 1), including highlands, mare, and the transitional boundaries between them. Graben trends listed in Table 1 show a wide range of orientations, and when graben were in spatial association with the maria they preferentially show orientations concentric or radial to these units. The fault systems comprising the graben range in length from ~ 43 to 453 km. Maximum displacements for the analyzed 14 graben range from 128 to 1115 m, with an average maximum displacement of 444 m. We also categorized dip-direction of the master fault (Table 1) for later interpretation (see implications for origin of graben). Graben widths were measured for each graben and also compiled in Table 1. Their maximum widths range from 1–5 km. Grabens were also assessed in terms of their cross-sectional symmetry, with structures showing symmetric, asymmetric, and variable geometries (Table 1).

Graben include highly segmented faults, as well as structures composed of long, single segments for both master and antithetic faults, ranging from two to up to 32 individual segments. The analyzed graben contain a total of 184 individual fault segments with individual fault lengths ranging from 3–166 km (Table 1). Rima Cardanus 1 (Fig. F) and Rimæ Plinius (Fig. 2.12) are the only graben that are composed of two single

oppositely dipping normal faults, all other systems show varying amounts of fault segmentation (Table1).

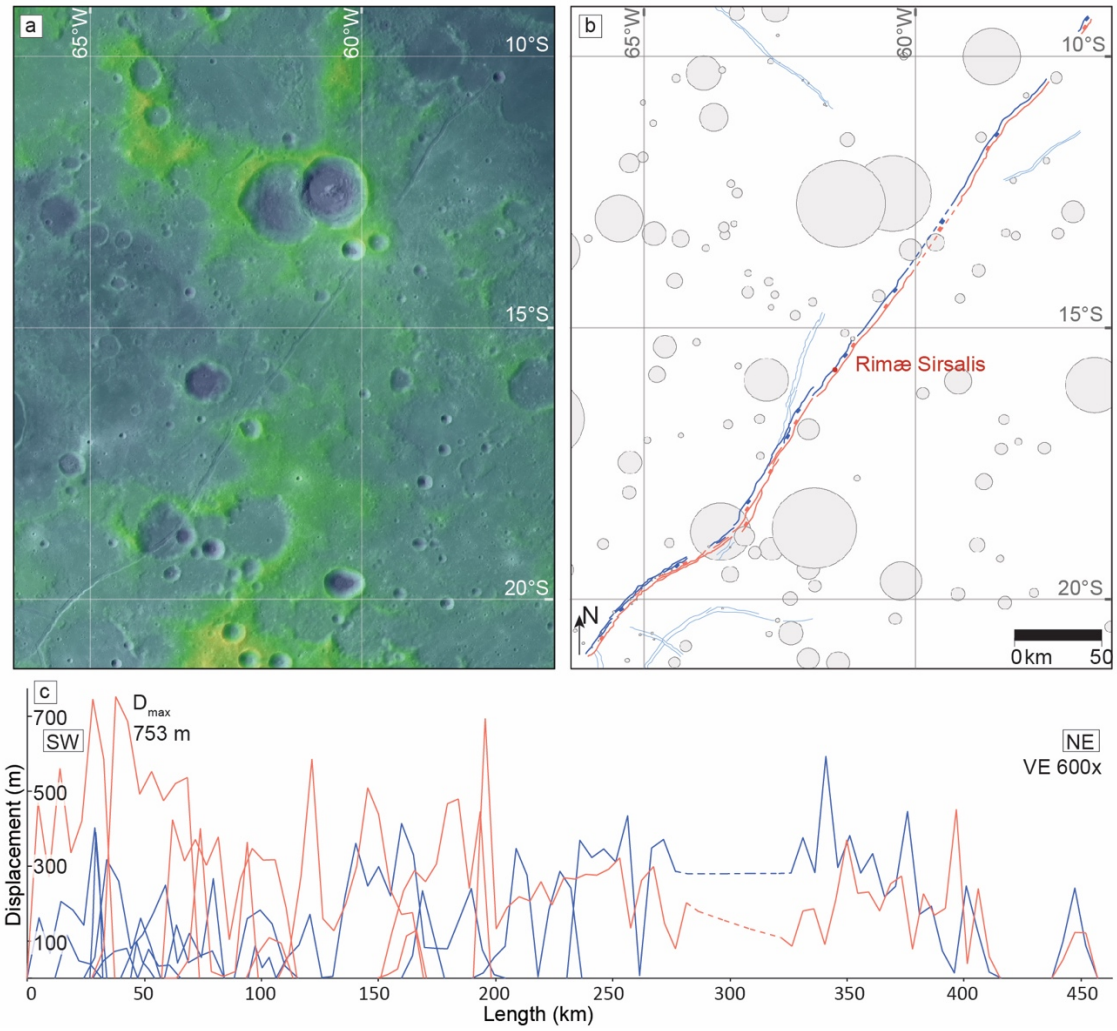

Figure 2.14 Structural analysis of Rimæ Sirsalis centered at 16°S, 059°W. (A) A LOLA DEM over LROC global image mosaic in equirectangular projection depicts Rima Sirsalis progressing further into the highland in a southwestern direction. (B) Abundant fault interaction is visible in the geologic map of the area. (C) Rima Sirsalis's slip

distribution is somewhat flattened higher displacement on the southwestern side in comparison to the northeastern graben portion.

All 14 graben systems show a high variability in the types of segment interaction and linkage. A total of 9 systems display at least one overlapping (i.e., soft-linked) fault segment, and many display more than three such overlap map patterns. Underlap between individual fault segments is found to occur for fault segments at Rima Flammarion and Oppolzer (Fig. 2.7), Rimæ Gerard (Fig. 2.8), Rimæ Goclenius 1 (Fig. 2.9), Rima Hesiodus (Fig. 2.10), and the graben in Schrödinger (Fig. 2.13). Fault jogs (i.e., hard-linked), are predominantly found in graben systems that also host overlapping or underlapping fault segments.

The fault throws and their resulting slip distributions for each graben in this research also display a wide range of displacement amounts and overall slip distributions along the fault strike. From all of our detailed slip distributions (Fig. 2.3-2.14), we compiled their general shapes of the master fault to better understand differences in slip distribution and to further classify them based on their shapes (Fig. 2.4). We extracted the profile shape by removing information on the individual faults to capture the overall slip distribution shape. These generalized slip distributions were then normalized for length and maximum displacement. This classification method reduces detail and allows us to better compare the general shapes of slip distributions for profiles composed of a single fault segment with profiles composed of 32 fault segments. Differences are still present in

a number of segments and can be attributed to this decrease in detail. The individual slip distribution shapes for each graben display a much higher level of detail, as well as show all individual fault segments, and their detailed descriptions and interpretations can be found in each corresponding figure.

Our displacement distribution analysis allows us to categorize that Rima Ariadaeus (Fig. 2.3), Rima Cauchy (Fig. 2.5), Rimæ Goclenius 1 (Fig. 2.9), and Rimæ Plinius (Fig. 2.12) have overall peaked slip distributions (Fig. 2.15A). Generally, the peak for these entire graben slip distributions is located near the center of the entire fault length. Displacement variations towards the tips are attributed to the influence of rough terrain, fault interaction, as well as the generalization of profile shapes.

We classify the overall shapes of Rima Cardanus 1 and 2 (Fig. 2.4), Rima Flammarion and Oppolzer (Fig. 2.7), Rimæ Gerard (Fig. 2.8), Rima Hesiodus (Fig. 2.10), Rimæ Mersenius (Fig. 2.11), and the graben in Schrödinger (Fig. 2.13) to have plateaued slip distributions (Fig. 2.15B). These slip distributions do not clearly indicate a single peak, but rather reflect small variations in displacement along a more constant slip distribution along the entire length of the graben. Unclassified slip distributions (Fig. 2.15C), Daniell (Fig. 2.7), Rimæ Goclenius 1 (Fig. 2.9), and Rimæ Sirsalis (Fig. 2.14) are grabens that are formed by a large number of individual fault segments (Table 1). These individual fault segments show a high variability of along-strike displacement (Fig. 2.15C) and they may be in various stages of fault interaction. Such stages of interaction are observed to include many underlapping segments with different amounts of maximum displacements, slip distributions of neighboring fault segments that show

displacement maxima skewed toward another, or multiple displacement maxima within one fault segment.

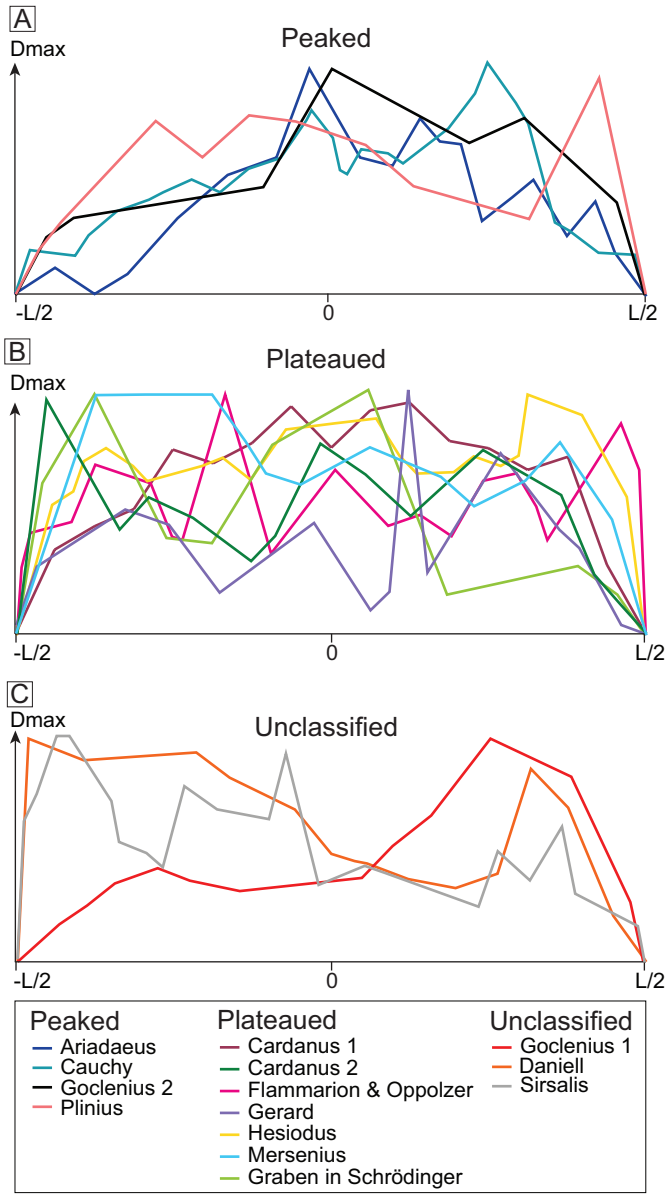

Figure 2.15 Slip distribution categories of all grabens normalized by fault length (L) and displacement. (A) Peaked slip distributions highlight a general peak near the center along graben fault length (0) and tapers towards the tips (-L/2) and L/2). (B) Plateaued slip

distributions reveal a much more flat-topped profile without a distinct central peak, which can be likely attributed to an intermediate stage of fault interaction. (C) Unclassified slip distributions do not clearly present either category and show a high variability in displacement.

Among the 14 different grabens, few displayed specific characteristics that stood out from our mapping and analysis. Grabens located in rough or elevated terrain frequently show high displacement along those regions. Both Rima Ariadaeus (Fig. 2.3) and the graben in Schrödinger basin (Fig. 2.13) display their maximum displacements of 1022 m and 1115 m, respectively, where it perpendicularly crosses a ridge of rough terrain. Rough terrain or elevated topography also produces relatively high maximum displacements in Rimæ Sirsalis. Those displacements are the highest displacements measured in this study, exceeding typical maximum displacements by a factor of two or three (Table 1). In situations, where the grabens was oriented parallel to a mare unit, the master fault scarp faced (dipped toward) the mare (Fig 2B). Rima Cardanus 1 (Fig. 2.4), Rimæ Daniell (Fig. 2.6), Rima Flammarion and Oppolzer (Fig. 2.7), Rima Hesiodus (Fig. 2.10), and Rimæ Plinius (Fig. 2.12) are all oriented circumferentially to their respective mare and display a master fault facing towards the mare center.

Displacement-to-length scaling

This study analyzed 14 predominantly segmented grabens with a total of 184 individual faults. First, we investigated all fault segments with their individual maximum

displacements and fault segment lengths, followed by an analysis of the maximum displacement and length of the entire graben system.

Displacement-to-length (D_{max}/L) scaling studies suggest a power-law relationship that depicts proportional growth of displacement and fault length (Cowie and Scholz, 1992a; Dawers et al., 1993; Clark and Cox, 1996; Schultz et al., 2006; Polit et al., 2009) that can reflect interaction and growth via fault linkage. Based on equation (1), a scaling exponent c=1 indicates linear scaling law, whereas any other number indicates scale-dependent (γ) geometry. The D_{max}/L scaling plot in Fig. 2.16A displays a range of three orders of magnitude of normal fault data from the 184 individual structures of this study. The data points are scattered broadly and indicate that fault displacements grow disproportionally to length. Scatter in the data is attributed to location specific controls, such as host rock type, fault driving stresses, and/or layer thickness. We find that individual D_{max}/L ratios range from 0.0012 to 0.135, with an average of 0.0121. Our regression analysis reveals a power-law relationship that exhibits a scaling exponent of c=0.45, γ value of 1.82, indicative of sub-linear fault growth. The great variability and poor fit of our D_{max}/L data is apparent in the low R^2 value of 0.37.

We also evaluated the D_{max} and total graben lengths for all 14 graben of our study in comparison to previously analyzed normal faults (Fig. 2.16B). Lunar fault length generally plots amongst the longest structures for which D_{max}/L data has been compiled. The D_{max}/L ratios fall between a γ of 10^{-2} and 10^{-3} and appear moderately scattered. The graben system D_{max}/L ratios are ranging from 0.0010 to 0.0048 (Table 1) with an average of 0.0023 and a median of 0.0018. Our regression statistics reveal a power-law relation of D_{max} = 0.17L0.64 with an R^2 value of 0.39.

Previously, D_{max}/L ratios for the Moon have been modeled by Schultz et al. (2006), which predicted lunar fault D_{max}/L ratios approximately ~0.04 times of terrestrial faults. Our results indicate that lunar grabens fall slightly higher than that predicted D_{max}/L ratio of ~0.001 (Schultz et al., 2006). A D_{max}/L ratio of ~ 0.0036 was determined from the average maximum displacement and length of six lunar grabens ranging in length from 34 km to 127 km (Watters and Johnson, 2010), scaling similarly to our results. In comparison to examples of terrestrial normal faults (Muraoka and Kamata, 1983; Walsh and Watterson, 1987; Krantz, 1988; Opheim and Gudmundsson, 1989; Peacock and Sanderson, 1991; Dawers et al., 1993; Cartwright et al., 1995), lunar grabens fault lengths are substantially longer than the compilation of terrestrial normal fault equivalents, and the displacement scales lower compared to examples from Earth.

Overlap and spacing analysis

To better understand fault growth and investigate the presence of multiple fault populations we analyzed the regions where fault overlap occurred. We selected all fault segments that had a section of the fault trace overlap with another fault segment. We measured the spacing (separation) and the amount of overlap between 43 faults. The actual overlap and spacing data tables can be located in Appendix A. The results of our overlap-to-spacing relationships are shown in a logarithmic plot, which revealed a wide range of fault overlap-to-spacing ratios (Fig. 2.16C). Observed normal fault spacing on the Moon occurs on the order of 100s of meters to kilometers, whereas overlap shows variability across two orders of magnitudes ranging from 100s of meters to 10s of kilometers. The statistical (power-law) fit of the overlap-to-spacing ratio is 5.88, a scaling exponent of 0.45, and a low R^2 of 0.26. In comparison to the compilation of terrestrial

overlap-to-spacing data by Long and Imber (2011), our data plots among of the largest spacings and overlaps (Fig. 2.16D). Our data plots within the same order of magnitude and thus shows similar overlap-to-spacing ratios as those from the terrestrial fault data, where overlap is ~3 – 3.6 times the spacing (Long and Imber, 2011; Fossen et al., 2016).

Implications for growth of normal faults on the Moon

Slip distributions can reveal information on magnitude and distributions of offset along-strike of a fault and, thus, have been used to gain a better understanding of growth and evolution of individual fault systems and fault populations (Cowie and Scholz, 1992a; Dawers and Anders, 1995; Willemse et al., 1996; Schultz and Fossen, 2002; Soliva et al., 2005). Specifically, slip distributions are commonly used as tools to understand driving stresses causing faulting, interaction and linkage of fault segments, as well as detection of fault confinement within a mechanical stratigraphy. Furthermore, slip distributions are the only means by which the accurate location of maximum displacements for faults are determined, and thus are a necessary tool for accurately determining and interpreting the displacement-to-length statistics. The D_{max}/L ratio relationship is one of the most important methods for interpreting fault growth and possible host rock properties. Additionally, the overlap-to-spacing relationships of faults allows us to further interpret fault linkage and serves as criterion to identify whether the investigated grabens are part of a single or multiple fault populations.

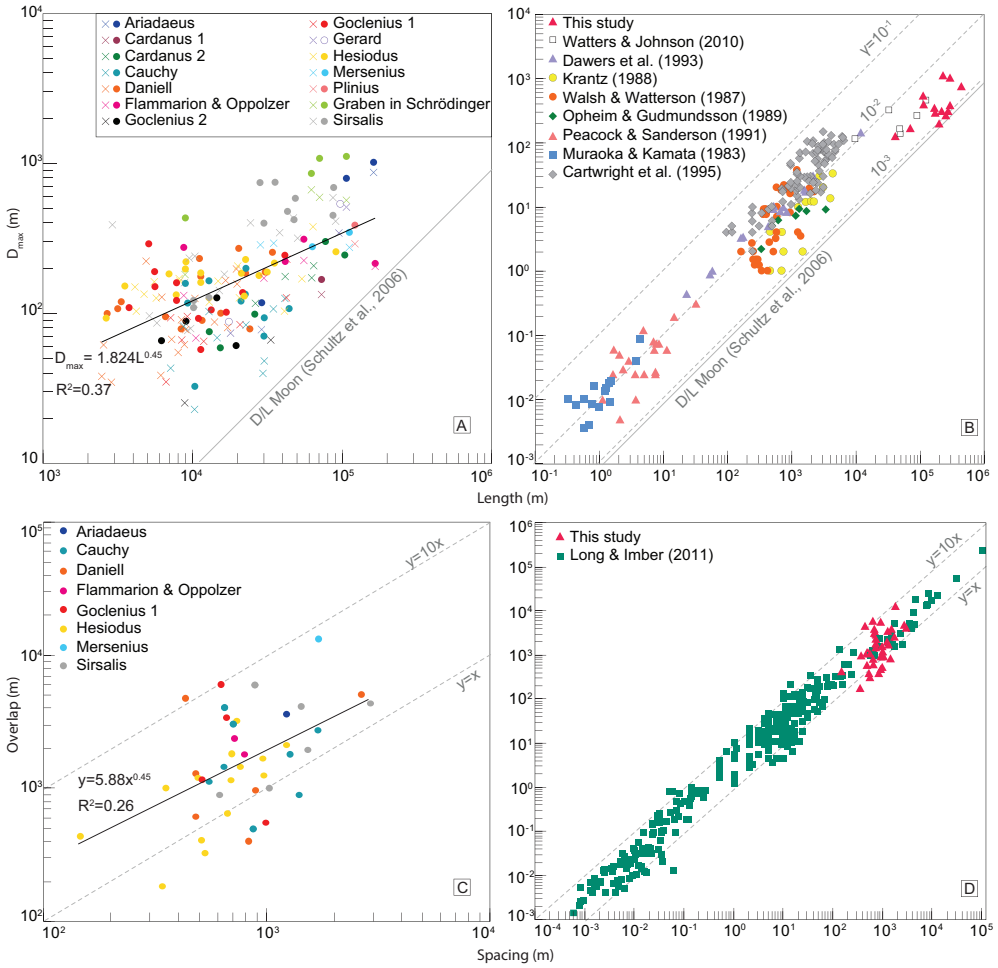

Figure 2.16 Displacement-to-length scaling and overlap-to-spacing data of lunar grabens. (A) Displacement and length plotted for all fault segments (184) including master (solid circles) and antithetic faults (crosses). The plot shows measurements with respect to model prediction for lunar normal faults from Schultz et al. (2006). (B) Comparison of the master faults of this study (solid triangles) to compilation normal faults on Earth and previously derived data for the Moon. (C) Overlap-to-spacing plot for all overlapping fault segments of this study. (D) Comparison of overlap-to-spacing data with compilation of Long and Imber (2011).

Implications arising from slip distributions

Among all analyzed grabens, we observe several trends among the slip distributions of the graben-bounding faults: 1) peaked slip distributions among all 14 grabens, 2) certain faults having much higher displacements than the rest of their neighboring faults, 3) individual faults displaying skewed displacements in areas where they interact or link with other faults, 4) plateaued slip distribution profiles among all grabens, and 5) variability in graben symmetry within all 14 grabens.

Approximately half of the individual fault segments (Fig. 2.5C-11C) and isolated graben-bounding faults (Fig. 2.4C) are found to have peaked slip distributions. In individual faults, a peaked slip distribution indicates isolated or unrestricted fault growth. A peaked slip distribution for a graben system may also be caused by unrestricted fault growth and the lack of individual fault linkage. Most fault segments of our study show peaked profiles, whereas only Rima Cardanus 1 (Fig. 2.4C), Rima Ariadaeus (Fig. 2.3C), Rimæ Goclenius 2 (Fig. 2.9) and Rima Cauchy (Fig. 2.5C) show cumulative peaked profiles (slip distributions of all segments added).

Several faults in this study display skewed slip distributions. This can be observed in several segments within the slip distributions of Rima Ariadaeus (Fig. 2.3), Rima Cauchy (Fig. 2.5C), Rimæ Goclenius 1 (Fig. 2.9C), Rimæ Plinius (Fig. 2.12C), and Rimæ Sirsalis (Fig. 2.14C). These asymmetric slip distributions are frequently indicative of fault interaction, as displacements of two neighboring fault segments are observed to be skewed toward one another. This phenomenon is observed here in fault segments that underlap, overlap, or at hard-linked faults that have two or more throw maxima. Such asymmetry in slip distribution is caused by interacting and overlapping stress fields

resulting in localized higher displacements near another fault segments (Gupta and Scholz, 2000).

We have identified seven grabens where the entire slip distribution is plateaued (Fig. 2.4). These include Rima Cardanus (Fig. Fig 2.4), Rima Flammarion and Oppolzer (Fig. 2.7), Rimæ Gerard (Fig. 2.8), Rima Hesiodus (Fig. 2.10), and Rimæ Mersenius (Fig. 2.11). The plateaued shapes of these graben systems can be attributed to abundant fault interaction or related to mechanical layer thickness. The plateaued slip distribution shape may also indicate fault restriction to a mechanical layer, causing the faults to grow in length while the depth of faulting and displacement are not increased (Soliva et al., 2005; Soliva et al., 2006).

Our study has found 7 symmetric grabens, four asymmetric grabens, and three grabens that show high variability within their symmetry (Table 1). Symmetry reveals information on maturity of the graben system. At the very first stage of graben formation, a single master fault is purely asymmetric due to the lack of another fault. A flexure of the layering towards the fault occurs, producing a rollover anticline. As fault growth continues, an antithetic fault is produced along the rollover anticline of the master fault and asymmetry decreases. Symmetric graben are interpreted as mature, evident in their similar displacements across master and antithetic faults. Asymmetric graben, where antithetic and master fault displacements are found to be substantially different, are interpreted as less mature. The graben with variability in symmetry predominantly start out as asymmetric at the end of the graben system and become more symmetric along strike. This finding, and the fact that symmetric and asymmetric graben occur on the Moon, indicates that the timing and rate of tectonics involved in graben growth may have

varied across the lunar surface, producing graben of various maturity stages. Additional evidence for that can be found in some asymmetric graben, such as Rima Daniell (Fig. 2.6), where there is a half-graben.

Implications arising from D_{max}/L scaling

The relationship between maximum displacement and fault length can reveal information on fault growth, interaction, and material properties of the host rock. Our analysis showed a wide range of D_{max}/L ratios, which is likely related to fault system maturity and represents different stages of fault growth and linkage (Peacock and Sanderson, 1991; Walsh et al., 2002). It also showed that growth follows a sub-linear path, indicating fault length accumulated faster than displacement. Isolated faults, which are somewhat rare (only two out of 14 graben systems in this study), account for the lowest D_{max}/L ratios. Soft-linked faults are found to have higher displacements and lower length due to the temporary fault arrest (Willemse et al., 1996).

In contrast, hard-linked faults are found to show a high displacement and thus higher D_{max}/L ratios. While soft-linked faults are present in nearly every graben system in this data set hard-linked faults are present in only three systems and represent additional high displacement ratios. The D_{max}/L statistic for this study show a sub-linear relationship with a lower D_{max}/L ratio, indicating that fault lengths are disproportionally longer than their displacement. This can be tied to the abundance of plateau-shaped slip distributions, which are found to occur as one phenomenon of fault growth by segment linkage (Cartwright et al., 1995). This interpretation also correlates well with the observed overlap and spacing map patterns, indicating that long faults are mainly formed by linkage.

In comparison to terrestrial normal faults (Muraoka and Kamata, 1983; Walsh and Watterson, 1987; Krantz, 1988; Opheim and Gudmundsson, 1989; Peacock and Sanderson, 1991; Dawers et al., 1993; Cartwright et al., 1995) our data reveals the presence of longer faults, but yet similar D_{max}/L ratios. Terrestrial faults used for a comparison are from different fault populations, but yet plot in a narrow region (Fig. 2.5B). The previously analyzed, smaller lunar graben-bounding normal faults and their respective D_{max}/L ratios (Watters and Johnson, 2010) are comparable to the values revealed in our study. Our D_{max}/L ratios plot above the calculated D_{max}/L ratio proposed by Schultz et al. (2006) (Fig. 2.5B). The difference in scaling relations between our study and the predictions from Schultz et al. (2006) is likely due to the assumptions for their conceptual modeling. The scatter within our data set also may be attributed to the presence of multiple fault populations. Lunar normal faults may occur within one or multiple populations, which can be further investigated with overlap-to-spacing ratios of interacting normal faults.

As described as part of the results, Rima Ariadaeus (Fig. 2.3), the graben in Schrödinger basin (Fig. 2.13), and Rimæ Sirsalis (Fig. 2.14) display much higher maximum displacements than other faults of this study. We find that these higher maximum displacements correlate with rough terrain and with regions that have higher elevations. In contrast, grabens located in smooth terrain generally have lower displacements. The grabens contained in smooth mare or mare-highland transition zones show displacements ranging between 169–538 m, whereas the grabens located in rough highland terrain can show displacements upwards of 1000 m. Additionally, crosscutting of features with positive topography, such as rims of ancient craters, appear to cause an

increase displacement of lunar graben-bounding faults. The influence of rough terrain on fault displacement may be linked to a change in mechanical properties or layer thickness in these areas. Rough or highland terrain may have mechanical properties or an increased layer thickness, both of which may lead to an increased fault displacement. Faults with lower displacement, located in smoother terrain, could by analogy reflect substantially different mechanical properties and/or a thinner mechanical layer than those found in the rougher highlands. Mechanical properties of the faulted lunar lithosphere and mechanical layering are further discussed in the next section.

Implications from overlap and spacing

Overlap-to-spacing ratios of faults can shed light on fault interaction and the presence of multiple fault populations. Our analysis of fault overlap and spacing among lunar normal faults revealed a wide range of these fault characteristics and their relationship to one another (Fig. 2.5C). This may be attributed to the diversity of lunar fault geomorphology. The average overlap-to-spacing ratio for our study is 5.5−6, higher than terrestrial equivalents. The average overlap-to-spacing ratio for all compiled terrestrial data sets is 3−3.5 (Long and Imber, 2011; Fossen and Rotevatn, 2016;).

Generally, our data set of lunar graben faults plots within the range of terrestrial overlap-to-spacing ratios compiled by Long and Imber, (2011). The effect of surface gravitational acceleration that has been proposed to cause a lower D_{max}/L scaling ratio for lunar faults (Schultz et al., 2006) is not apparent in the overlap and spacing relationships (Fig. 2.5B). Thus, it can be deduced that overlap-to-spacing relationships of lunar normal faults behave similarly to terrestrial normal faults, and the scatter displayed in our data is due to similar reasons of those in the terrestrial data sets. Scatter in the data is attributed

to location specific controls, such as host rock type, fault driving stresses, and/or layer thickness.

Mechanical layer thickness can be a strong factor controlling many aspects of a fault population, and previous observations have indicated a relationship exists between layer thickness and fault spacing. A characteristic fault spacing of ~ 0.5 times the layer thickness is found for fault populations on Earth. (Soliva et al., 2006). Based on the layer thickness and spacing relationships proposed by Soliva et al. (2006), and under the assumption that this relationship can be extrapolated to faults on the Moon, our data reveals a layer thickness range of 0.5 to 5.8 km, with an average layer thickness of 1.86 km. Potential candidates for the layers that could be considered mechanical units are either the mare basalts or the megaregolith. Recent studies of the mare basalt thicknesses revealed values ranging between 0.4–1.9 km (Michaut et al., 2016), 1.5–2 km along basin margins (Thomson et al., 2009), and 0.1–1.62 km with some of the thickest sequences to be estimated at average of 2.86 km (Gong et al., 2016) using various different types of methodologies.

The megaregolith thickness has equally been the subject of discussion and previous estimates have varied a lot. In recent studies, the megaregolith thickness has been suggested to range from ~100 km thick (Gillet et al., 2017), more conservative estimates at 25 km, with a structural disturbance at ~10 km depth (Jaumann et al., 2012), and the presence of a 34–43 km highly fractured crust (Wieczorek et al., 2013). Based on these studies, the megaregolith is found to be much thicker than our estimate of mechanical layer thickness. This implies that the grabens studied here are likely fully contained in a layer with rock-mechanical properties governed by those of the

megaregolith and thus it likely did not have a direct impact on the variability of scaling behavior of the faults investigated here. However, the thickness estimates for mare basalts coincide to first order with the mechanical layer thickness range derived from fault spacing. Therefore, the mare basalts may have formed a mechanical layer that influenced the scaling properties of the graben-bounding normal faults.

Although the overlap-to-spacing relationships display a scatter in the data, we do not detect any data clusters that would indicate if more than one normal fault population exists on the Moon or whether all normal faults are part of a single population. The scaling relationships derived in this study do not reveal if lunar normal faults are genetically linked to the same tectonic process or whether multiple tectonic processes could have formed them (see next section).

Implications for origin of grabens

Our data shows that lunar grabens in spatial association with the maria show two preferred orientations with respect to them. Most commonly they are either concentric or radial with regard to the nearest mare-filled basin. If a graben is concentric to a mare basin, we have found that the master-fault dip direction points toward the mare unit, indicating that some lunar grabens are closely tied to the emplacement of mare units or tectonics associated with basins and lowlands that are mare-filled. Most grabens dissect the lunar maria and surrounding highlands around them, but no grabens are found to be superposed by mare units. This is observed for Rima Hesiodus (Fig. 2.10), Rima Flammarion and Oppolzer (Fig. 2.7), Rimæ Daniell (Fig. 2.6), Rimæ Goclenius (Fig. 2.8), and Rima Cauchy (Fig. 2.5) and many other grabens that were not included in our detailed topographic assessment (Figure 2B). After emplacement of the mare units, they

must have cooled and contracted (Melosh et al., 2013), placing these units in an extensional stress state. Mechanically weaker zones, such as the mare-highland transitions, served as areas where faults localized.

The intrusion of dikes and topographic adjustment to mare loading of basins likely are additional factors contributing to the formation of lunar grabens and thus may have acted in concert or succession with mare cooling. It has been proposed that igneous dikes at depth are required to form lunar grabens (Head and Wilson, 1993; Wilson et al., 2011; Klimczak, 2014;). The dikes are likely correlated with the length of the graben and may have stalled at depths as shallow as 100-500 m of the lunar surface (Klimczak, 2014). In order for igneous dikes to form, the lunar lithosphere would also have to be under extension, and thus this tectonic regime is conductive to both dike and graben formation. Based on the methodology used here, we cannot distinguish between graben formation with or with no dike intrusion, as both processes have the potential to produce all of the geomorphologic characteristics of normal faults described in this study. Further research comparing dike-related topography, dike dimensions, and fault slip distributions would allow us to further distinguish the formation mechanisms of graben formation.

Conclusions

We mapped the extent of lunar grabens surrounding the maria and analyzed topographic variations of 14 lunar grabens that consist of 184 individual fault segments. We constructed structural maps, derived fault slip distributions, and performed displacement-to-length scaling and overlap-to-spacing analyses on the faults considered in this study. Our study shows that displacement scales disproportionally with length for

grabens on the Moon and that slip distributions first and foremost reflect fault interaction between fault segments of the graben.

Individual slip distributions in this study reveal peaked displacement reflecting uninhibited growth of fault systems, skewed displacement that highlights fault linkage, and plateaued slip distributions that may suggest a mechanical restriction at depth. Additionally, we found that three graben systems have substantially higher displacements than the other 11 graben systems, which we attribute to differences in mechanical properties, such as thickness of mechanical units or degree of fracturing between the anorthositic highlands and the basaltic maria. Graben symmetry displays several stages of maturity, where some grabens have not reached full symmetry.

Our study presents an in-depth study of long lunar grabens that brings new insights on their fault scaling relationships. D_{max}/L scaling shows that the ratio for individual faults is higher (0.012) than the ratio for the cumulative graben population (0.0023). The best-fit power-law relationship for the cumulative graben is $D_{max} = 0.171L0.64$. These relationships point to various stages of fault interaction and linkage and show that lunar normal have lower displacements when compared to equally long terrestrial faults. However, normal faults on the Moon have higher D_{max}/L ratios than previously predicted from modeling (Schultz et al., 2006) and also reveal a relationship between displacement and terrain type. Furthermore, overlap-to-spacing ratios suggest that overlap scales to spacing by 5−6. These statistics do not help us understand how many normal fault populations are present on the Moon, and thus they cannot be used to distinguish between different tectonic processes responsible for graben formation. However, information from displacement paired with map patterns show that long lunar

grabens are either concentric or radial to the maria, where mare-concentric grabens, in particular, show the master fault dipping toward the mare center. Therefore, we interpret that formation of these grabens is linked to cooling of the lunar maria.

In the future, our results can be used to better understand fault growth mechanisms on the Moon, as well as to better constrain mechanical properties of various types of host rock on the Moon. The data set will also enable us to further investigate the relationship between graben orientation, normal fault morphology, and the presence or absence of underlying dikes.

Acknowledgments

We thank the editor Kurt Stuewe and two anonymous reviewers for their constructive comments on this research. This work was supported by the Lunar Data Analysis Program under grant NNX15AP91G.

CHAPTER 3

EVOLUTION OF GEOMETRIC AND STRENGTH PROPERTIES OF LARGE LUNAR NORMAL FAULTS

[1] Callihan, M. B. and Klimczak. To be submitted to *The Journal of Structural Geology.*

Abstract

Lunar grabens have previously been analyzed for their geomorphological character and topographic expressions. Individual normal faults producing these grabens have been investigated for their displacement-to-length relationship using slip distributions, which display how fault displacement plots along fault length. While these investigations brought detailed insights into the distribution, extent, and growth patterns of lunar grabens, there is no research that works toward understanding the growth mechanism, loading conditions, and host rock and fault rock strengths that played a role in forming these structures. In order to specifically address these outstanding questions, we used a post-yield fracture mechanics modeling approach on 14 graben systems that we previously studied to constrain loading conditions and strength properties in the lunar lithosphere required for fault formation. This model has not yet been tested against natural observations. Model solutions reveal that graben systems and the individual faults that form them either (1) exhibit constant loading conditions and rock strength throughout the time of fault growth, or (2) that loading conditions and rock strength both decrease over the lifetime of the faults. We find 9 grabens that display growth consistent with scenario (1), and five grabens to display growth consistent with scenario (2). Fault growth for scenario (1) highlights that fault length and displacement grow proportionally over time, whereas for scenario (2) faults evolve disproportionally, displaying decreasing fault displacement over the time.

Introduction

Fault growth

Normal faults are defined as a planar discontinuity with shear displacement accommodated by frictional sliding, where the hanging wall is downthrown in relation to the footwall. Normal faults tend to evolve into grabens over time. A single isolated normal fault can be used as an analogy as one half of a graben, i.e., a half-graben. The lateral extent of a single (isolated) fault corresponds with the total length of the fault terminating in the fault tips. Displacement, which is the (shear) offset created during faulting, gradually changes along the length of the fault and typically has the maximum displacement (D_{max}) in the center, tapering toward the tips. Normal fault growth in particular has been studied by many structural geologists and aids in the understanding of the complex nature of graben systems (Peacock and Sanderson, 1991; Trudgill and Cartwright, 1994; Cartwright et al., 1995; Willemse, 1997; Cartwright and Mansfield, 1998; Gupta and Scholz, 2000; Mansfield and Cartwright, 2001; Peacock, 2002).

Individual normal faults grow in length by the propagation of fault tips during slip events along with an accumulation of displacement along the fault plane. Displacement and length both grow larger each successive slip event (Cowie and Scholz, 1992a; Shipton and Cowie, 2003) as well as fault linkage (Peacock and Sanderson, 1991; Cartwright et al., 1995; Mansfield and Cartwright, 2001). It is uncommon that just one single isolated fault forms and grows via slip, rather a region experiencing stress will nucleate multiple small faults in different locations, creating a fault population of similarly striking faults (Schultz and Fossen, 2008; Fossen, 2009).

In this case, some faults can increase their length and displacement over time by linking or coalescing with other faults in the region (Cartwright et al., 1995; Willemse, 1997; Fossen et al., 2010). In particular, two approaching segments that have not linked are said as underlap. Underlap reaches a critical point when fault segments and their stress fields start to interact with each other (Willemse, 1997). When fault tips have moved past one another, the faults are considered to be overlapping. Once the interaction between segments begins, the fault tip propagation will temporarily arrest, and fault tips begin curving toward each other (Peacock and Sanderson, 1991; Willemse, 1997; Fossen and Rotevatn, 2016). Overlapping and underlapping segments are considered to be soft-linked until continued faulting internally deforms the region between, creating a hard-link. The linkage of smaller segmented faults in a population can lead to the formation of complex structures.

Graben that have grown by linkage of smaller segments can exhibit a much more complex set of structures and variety of map patterns. These map patterns are influenced by the variable spacing and overlap within the initial approaching fault segments (Allken et al., 2013; Fossen and Rotevatn, 2016). Overall the length of the fault is indicative of its age. The longer a fault or a fault system is, the more time has passed, and the higher number of slip events occurred.

As faults grow larger, not only their length and displacement evolve, but also the fault rock. The fault slip surface, also referred to as fault core, is the central plane along which most of the displacement is accumulated and consists of intensely crushed or sheared rock (Caine et al., 1996; Schultz and Fossen, 2008; Fossen, 2009). Resulting fault cores can be very different, which depends on the type of host rock, its lithology,

porosity, and kinematics during fault propagation. Unconsolidated, crushed fault rock with less than 70% matrix is termed fault breccia and can be cohesive or non-cohesive in fault cores (Fossen, 2009). In non-cohesive rocks the formation of fault gouge can occur, which is strongly ground host rock with a higher matrix to fragment ratio. With ongoing faulting, the fault core develops shear fabrics, which create preferentially aligned minerals along the slip surface, further changing the rock properties along the fault slip plane (Kim et al., 2004; Fossen, 2009). The rock damage that occurs during the initiation, propagation, interaction, and slip build-up extends beyond the fault core into the damage zone (Kim et al., 2004) and encompasses areas of fracturing surrounding the fault. The fault core and damage zone are complex areas of deformation, that change host rock characteristics and influence future fault slip.

One way to analyze fault growth is to use slip distributions, which highlight how fault geometry varies with length, describing the relationship between fault length and displacement. A slip distribution for a single fault shows displacement increasing from the fault tips, along the fault length, until it reaches its maximum at the fault center. General slip distributions can be bell-shaped, peaked, or plateaued. Slip distributions also reveal the complexity along a fault, where linked or interacting faults display higher displacements which are often skewed towards the interacting fault segments. They reveal information on fault growth patterns, where plateaued slip distributions can be attributed to an intermediate growth stage and peaked slip distributions reflect initial or advanced stages of faulting (Peacock and Sanderson, 1991; Cartwright et al., 1995; Kim and Sanderson, 2005) These slip distributions are a representation of all slip events that integrated over the lifetime of a fault, not a single slip event.

Previous studies have suggested that a linear correlation between the length, and maximum displacement of a fault exists, where fault displacement increases proportionally with fault length (Cowie and Scholz, 1992b, 1992a). This relationship is influenced by rock type and regional stress environment. Isolated faults have shown scaling between length and displacement that is near one, whereas fault linkage and mechanical layer restriction at depth influence this relationship and result in lower numbers. This relationships has been studied and revealed ratios of 0.001–0.05 (Muraoka and Kamata, 1983; Walsh and Watterson, 1987; Krantz, 1988; Opheim and Gudmundsson, 1989; Peacock and Sanderson, 1991; Cowie and Scholz, 1992a; Dawers et al., 1993; Cartwright et al., 1995; Dawers and Anders, 1995; Clark and Cox, 1996; Watters et al., 2000; Mansfield and Cartwright, 2001; Schultz and Fossen, 2002; Schultz et al., 2006; Polit et al., 2009; Watters and Johnson, 2010; Gudmundsson et al., 2013; Roggon et al., 2017).

Even though slip distributions and displacement length relationships reveal an abundant amount of information of fault growth patterns, we can further investigate the regional stress environment and strength properties in the lunar lithosphere required for fault formation using fault growth models. Multiple fault growth models exists and are used to describe how faults grow. Each predicts a different shape for fault distributions that can be matched to observed slip distributions. Symmetric Linear Stress Distribution models, Linear Elastic Fracture Mechanics models, and Post Yield Fracture Mechanics models predict peaked, elliptical, bell-shaped profiles, respectively. All models consider the elastic properties of the lithosphere and relate frictional strength and remote stress affecting the fault plane to the host rock strength. Using these type of growth models, we

can obtain information loading conditions and strength properties in the lunar lithosphere required for fault formation.

Fault growth in complex systems on the Moon

Long lunar grabens are predominantly located peripheral to the lunar maria (Golombek, 1979; Hiesinger and Head, 2006; Smith et al., 2010; Klimczak, 2014; French et al., 2015; Nahm, 2016; Nahm et al., 2016,). These grabens can also be found in floor-fractured craters (Schultz, 1976; Jozwiak et al., 2012, 2015), large impact basins (Wilhelms et al., 1979; Nahm, 2016). They occur in distinctive lunar terrains, such as basaltic mare, anorthositic highlands and mare-highland transitions. Low erosion rates on the Moon preserve fault related topography used to study fault extent, offsets and displacement from accrued slip events.

We previously conducted a detailed analysis on 14 segmented lunar grabens revealing the relationships between displacement and length, overlap and spacing, and their implications for the evolution and origin of grabens by systematically analyzing the associated slip distributions (Callihan and Klimczak, 2019). As with most long fault systems, grabens appear as complex systems and likely have complicated zones of deformation surrounding the fault slip surface itself. We showed that sub-linear growth of 184 individual faults predominantly occurs via segment linkage (Callihan and Klimczak, 2019, Chapter 2). Generally, higher displacement length scaling ratios than previously suggested are present on the Moon and regional differences in topographic expressions of faults were both ascribed to variations in host rock properties and mechanical stratigraphy. In particular, the produced slip distributions were interpreted to reflect uninhibited fault growth, vertical growth restriction, and an abundance in fault linkage.

Slip distributions displayed several stages of symmetry indicating different levels of graben maturity. Furthermore, three analyzed graben, Rima Ariadaeus, Rima Sirsalis, and the graben in Schrödinger, displayed higher topography than the other structures. We attributed this finding to differences in mechanical host rock properties, including but not limited to mechanical unit thickness and degree of fracturing between different types of lunar crust. Information from the slip distribution combined with map patterns revealed that mare-concentric grabens are oriented such that the master fault dips towards the center of the mare. Further detail on the graben geomorphology and slip distributions can be found in Callihan and Klimczak (2019, Chapter 2). Even though we elucidated the growth of graben on the Moon in the previous study, many questions tied to mechanical properties and fault growth remained open. To better understand fault growth and the response of lunar rock to faulting, we modeled lunar fault growth using Post Yield Fracture Mechanics (PYFM) and matched the modeled solutions with our previously observed slip distributions to gain a better understanding of the evolution of loading conditions as faults grow larger and the mechanical properties of the fault-, and host rock.

Modeling methodology

Several models exist to explain fault growth, but only the Dugdale model used in Post-Yield-Fracture-Mechanics (PYFM) considers the inelastic deformation that occurs during fault growth (Cowie and Scholz, 1992b). The PYFM model produces fault slip distributions of plane strain conditions using material strength, elastic properties and fault length. Using these models allows us to gain a better understanding of the required loading conditions and strength properties that enable the growth of faults in the lunar lithosphere. By matching the modeled PYFM profiles to the existing slip distributions we

will extract model parameters, remote stress and yield strength, and compare them with all faults in the same fault zone (for each graben) and finally across all modeled lunar normal faults. This methodology will specifically allow us to relate fault shape and strength properties as a function of fault length, which is analogous to time.

Figure 3.1 shows the Dugdale model in a crack and its resulting displacement profile. This model considers Mode I cracks caused by tensile remote stress, σ_r. Counteracting fracture opening is the yield strength, σ_y of the material, that, when overcome (Fig. 3.1A), will give way to plastic deformation at the tip of the crack with length *s* (length of inelastic zone) (Fig. 3.1B). Due to the nature of a plane strain model, deformation occurs only in the x and y directions of the fault that are defined parallel to the fault length, *L*, and displacement, *d*, respectively, and not extending into the third dimension (Cowie and Scholz, 1992b). Applying this Mode I growth model to faults provides a simple technique to analyze a complex process. Cowie and Scholz (1992a) show that the characteristics of the Dugdale model for cracks can be applied to faults since they are consistent with specific fault observations. Foremost, because large faults grow by increasing fault length with approximately constant down-dip width and are considered two-dimensional structures that can be modeled using plane strain (Cowie and Scholz, 1992b). Additionally, faults meet the other criteria required by the Dugdale model including, producing displacement shapes in which displacement tapers off to the fault tips, which must be attributed to the inelastic zone at the tip, peak stress at the tips equals σ_y, material beyond the tip deforms elastically, and finally that the inelastic zone decreases with increasing σ_y.

The modeled displacement distribution along the fault length will result in a bell-shaped curve, with maximum displacement, D_{max}, in the center of the fault, and displacement tapering towards the fault tips (Fig. 3.1B). The modeled fault tips have the length s and displacement of d_o at the location where the inelastic zone becomes plastic (Cowie and Scholz, 1992b). Furthermore, the model takes into consideration the elastic rock properties of the lithosphere. The deformation modulus, E, shear modulus, μ, Poisson's ratio, ν, were adopted from previous studies.

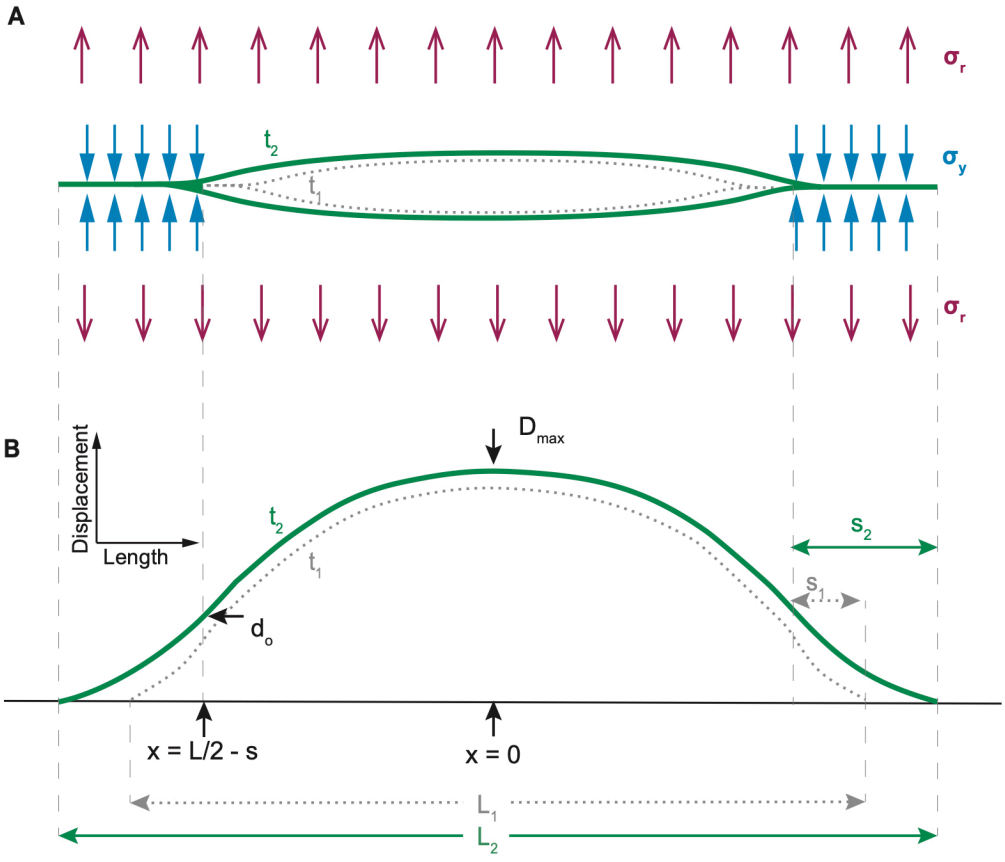

Figure 3.1 Overview of the Dugdale model changing over time. Adapted from Cowie and Scholz (1992b). (A) A crack with a length L, remote stress acting on crack opening, yield

strength counteracting at fault tips. Crack grows larger over time (t_1-t_2). (B) Bell-shaped slip distribution for the crack over time, maximum displacement is located at center of the fault length (x=0). Inelastic zone length, s, begins at length x=L/2-s and marks the inflection point for the curve, its magnitude at that location is d_o. Parameters L, s, and d_o become larger over time.

We used the framework outlined by Cowie and Scholz (1992b), to determine and produce PYFM fault model solutions that can be matched to observed slip distributions. We assumed bulk elastic conditions without regional deviations for the lunar lithosphere during continued fault growth. We calculated following parameters to derive the shape of the slip distribution: *d,* as a function of position along fault length, D_{max}, the maximum displacement, *s*, the length of the inelastic zone and d_o, yielding the displacement magnitude at the inflection point at the beginning of the inelastic zone (Cowie and Scholz, 1992b; Eqns. 8, 5, 2, 9, respectively). Under the assumption that the elastic properties of the host rock surrounding the fault plane remained constant, we used the same deformation modulus, shear modulus, and Poisson's ratio for all faults in this study. A previous study assessed the brittle strength of lunar lithosphere considering the degree of rock mass fragmentation and fracturing using the Rock Mass Rating System (Klimczak, 2015). We used their research to determine the deformation modulus of 25 GPa, which based on a lunar rock mass rating of 65 falls into the acceptable range of 50 – 80 and reflects the nature of –substantially fractured upper lithosphere (Schultz et al.,

2006; Klimczak, 2015). The Poisson's ratio of 0.25 for the Moon was adopted from Klimczak (2015). Assuming bulk rock conditions for the lunar lithosphere simplifies the analysis but has to be considered as a caveat for interpretation because realistically conditions are non-uniform. The fault length, *L*, corresponds to the observed fault length of each individual fault trace in map view, and *L/2,* the half-length of the individual faults. The remote stress, σ_r, and the uniform closing stress, or yield strength σ_y, were varied for each individual graben system, and σy relates to σ_r by a factor of up to four. Each unique combination of remote stress and yield strength applied over a specific fault length produces differently shaped PYFM models, with different D_{max} magnitudes and ellipticities. Modeled loading conditions and strength properties are cumulative, accounting for the total number of slip events necessary to produce the observed fault lengths and displacements (Cowie and Scholz, 1992b; Gupta and Scholz, 2000). They do not reflect the individual slip events although the PYFM model was originally intended for a single slip event. Yet this model can be applied to slip distributions since all required characteristics of the model are fulfilled and behavior remains the same.

For each graben complex, we modeled and matched the slip distributions for all faults comprising the master fault. We then modeled the individual displacement profiles by varying the σ_r and σ_y until the modeled D_{max} provided a match to the observed D_{max} (Fig. 3.2). The best matches between the observations and our modeled solutions were visually determined. We chose a visual comparison of observation to model rather than statistical methods, because statistical best fit models would not allow to accurately capture the complexities, we observe in the slip distributions. Calculating the PYFM that

yielded the lowest standard deviation (SD) instead of determining visual best fit would have resulted in model solutions that would not reflect the displacement characteristics of the profiles. Regions that show elevated or skewed displacement caused by linkage would not be reflected in a best fit determined by its lowest standard deviation. In such scenarios a best fit calculated via SD would yield a model solution with highly elevated displacement that does not fit the observed slip distribution.

Even though a visual best fit better captures the complex shapes of slip distribution, it is important to provide a measure how well these models capture observations to establish that the models are a good representation overall. To quantify the fit, we determined the SD using residuals between the observed and modeled displacements (Fig. 3.2). The nodes along the observed slip distribution represent the actual recorded displacement extracted from the lunar surface. We calculated the displacement deviation of the model along the exact same position along the length of the fault and produced the total SD for each individual fault, as well as the total SD for each graben master fault. A range of statistical parameters for each fault has been provided in Appendix B.

Results

Post Yield Fracture Mechanics model solutions

Of the 14 graben master faults, we investigated 89 individual faults that were part of the master fault system and produced PYFM model solutions for each individual structure (Figs. 3.2, 3.3) within the system. In general, we were able to produce suitable matches for the PYFM modeled faults to the observed slip distributions (Table 3.1).

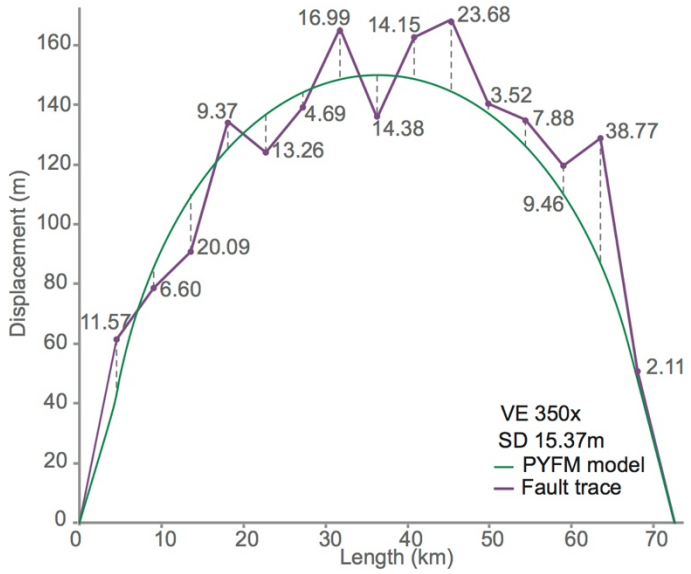

Figure 3.2. Observed and modeled slip distribution for Cardanus 1. The observed slip distribution (purple line) shows the actual slip distribution profile for the exposed fault surface. Locations along the fault where displacement was originally measured are marked (nodes). The PYFM model (green line) closely matches the observed profile and displays the typical bell-shaped profile. Standard deviation (dashed lines and numbers) between observed profile and model was quantified along locations where displacement was measured.

We began by applying the same remote stress and yield strength for each individual fault within a graben complex and varied these two parameters until a good visual fit was achieved for the entire system. This approach worked well for Rima Ariadaeus (Fig. 3.3), Rima Cardanus 1 and 2, Rima Gerard, Rimæ Mersenius, Rima

Cauchy, Rimæ Daniell, Rima Flammarion and Oppolzer, Rimæ Goclenius 2 (Fig. 3.3). Although each of these graben systems have their own individual loading conditions, the faults within each of these graben systems have the same remote stress and material yield strength (Table 3.1). When matching PYFM models to observed slip distributions, occasionally it was necessary to split a long fault into two shorter faults, or combine shorter faults into a longer one to reflect the general character of the slip distribution, which yielded a different number of PYFM models than the originally mapped fault segment (Callihan and Klimczak, 2019, Chapter 2). This was only done in areas where overlaps, jogs, or underlaps are observed and indicate fault interactions that justify splitting or merging faults for improving the PYFM model fits. Subdivision or merging of faults was based on map view interpretations of fault interaction.

When applying the same process to the five remaining graben systems we investigated, the PYFM models only matched some of the faults but yielded poor fits for others. Regardless of changing remote stress or yield strength, we were unable to produce suitable matches between PYFM models and observed slip distributions that used the same loading conditions for the entire graben. Therefore, in the cases of Rimæ Goclenius 1, Rima Hesiodus, Rimæ Plinius, the graben in Schrödinger, and Rimæ Sirsalis, we had to change the loading conditions for each individual fault within the fault system to achieve better fits. The following discussion describes the model and observed slip distributions in detail, in order as they appear in Figure 3.3.

Rimæ Plinius was originally mapped and reported as one individual graben-bounding master fault, but to produce suitable PYFM matches, we divided the fault into two fault segments. The location of the division is along a point of change in graben

Table 3.1 Observed graben parameters and PYFM model solutions of loading conditions and fault strength.

Graben system	**Length of system (km)**	**D_{max} Observed (m)**	**Fault segments modeled**	**D_{max} Model (m)**	**σ_r (MPa)**	**σ_y (MPa)**	**Loading conditions**
Rimæ Plinius	121.2	388.9	2	307	50 – 80	190 – 312	evolving
Rima Cardanus 1	72.5	168.5	1	149	30	114	constant
Rimæ Gerard	115.3	538.3	5	157	65	253	constant
Rimæ Mersenius	173.0	348.7	3	396	65	253	constant
Rima Cardanus 2	223.2	302.5	6	196	35	140	constant
Rimæ Goclenius 1	179.3	291.4	4	158	78	257	evolving
Rimæ Goclenius 2	42.9	127.5	9	109	42 – 130	164 – 507	constant
Rima Cauchy	204.8	200.2	6	145	35	139	constant
Rimæ Daniell	264.7	272.4	14	188	58	225	constant
Rima Flammarion & Oppolzer	282.9	313.5	6	207	45	175	constant
Rima Hesiodus	303.7	381.4	16	233	50 – 230	195 – 897	evolving
Schrödinger graben	234.1	1115.1	4	539	65 – 200	256 – 783	evolving
Rima Ariadaeus	304.8	1022	3	566	51	167	constant
Rimæ Sirsalis	453.3	752.6	10	634	50 – 250	195 – 975	evolving

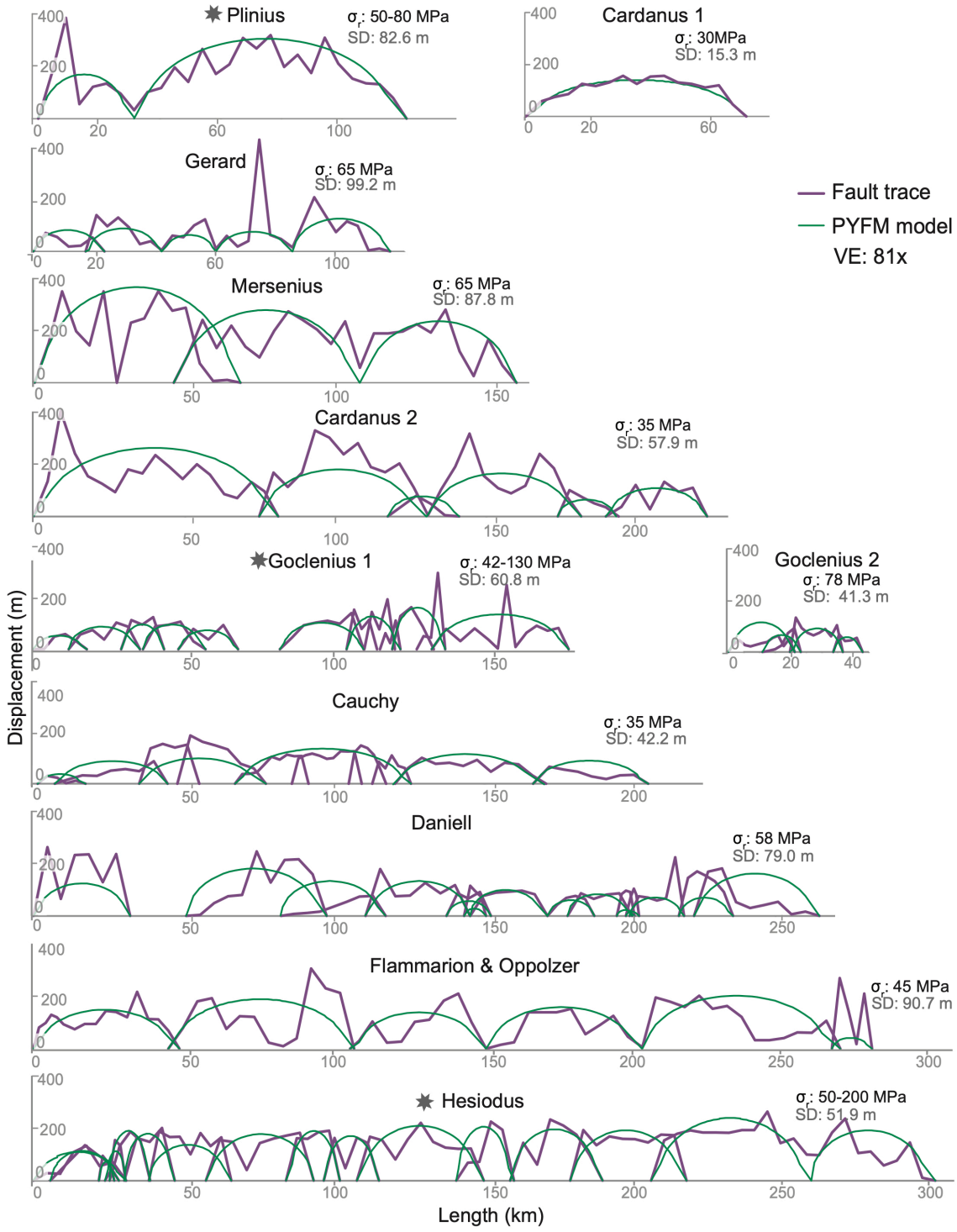
Plinius
σr: 50-80 MPa
SD: 82.6 m
Cardanus 1
σr: 30MPa
SD: 15.3 m
Gerard
σr: 65 MPa
SD: 99.2 m
Fault trace
PYFM model
VE: 81x
Mersenius
σr: 65 MPa
SD: 87.8 m
Cardanus 2
σr: 35 MPa
SD: 57.9 m
Goclenius 1
σr: 42-130 MPa
SD: 60.8 m
Goclenius 2
σr: 78 MPa
SD: 41.3 m
Cauchy
σr: 35 MPa
SD: 42.2 m
Daniell
σr: 58 MPa
SD: 79.0 m
Flammarion & Oppolzer
σr: 45 MPa
SD: 90.7 m
Hesiodus
σr: 50-200 MPa
SD: 51.9 m
Displacement (m)
Length (km)

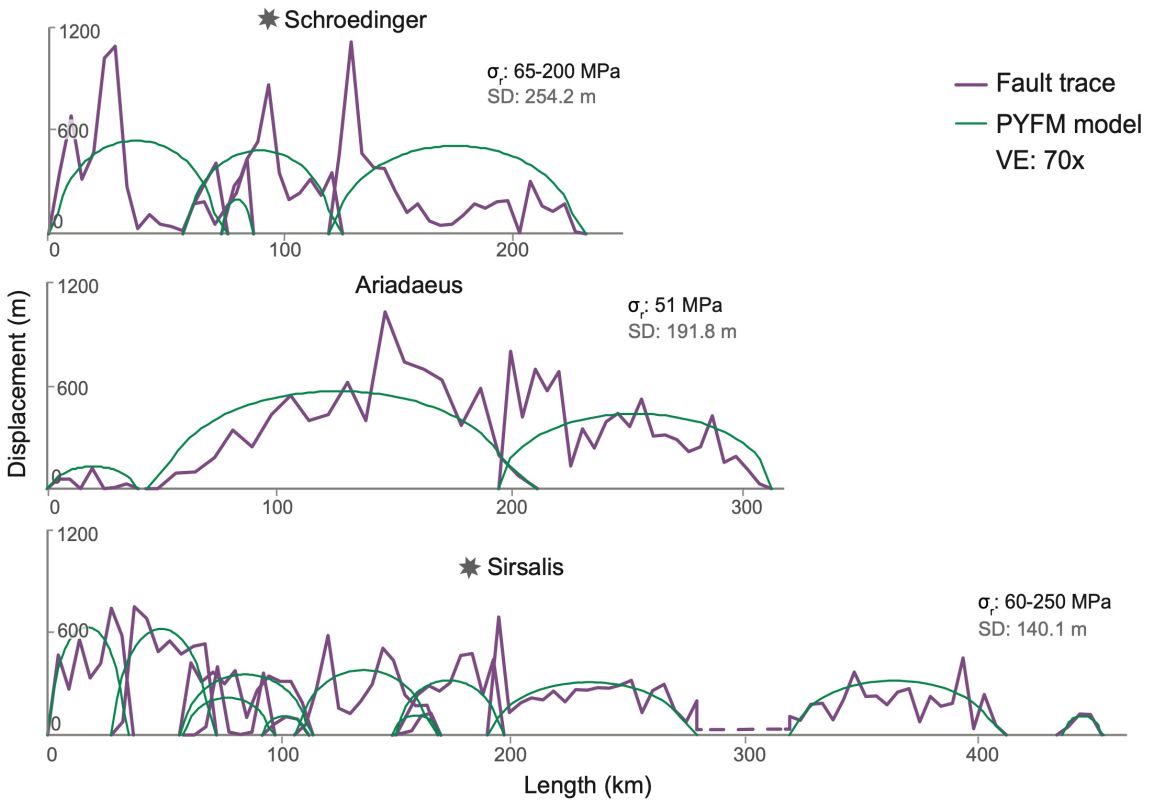

Figure 3.3 Slip distributions with matched PYFM predictions. Observed slip distributions (purple lines) and their respective matched PYFM models (green lines) for low to moderate displacement systems. Standard deviation between models and observed displacement for the graben are shown in grey. Each graben system required different remote stress for faults to propagate, faults with evolving loading conditions are marked with a star. Vertical exaggeration is displayed in each figure.

orientation that coincides with a local slip distribution minimum, which was previously interpreted as location of fault linkage (Callihan and Klimczak, 2019). By splitting the

fault into two and varying the loading conditions between them, we were able to produce good visual fits, with a remote stress of 50-80 MPa and a yield strength of 190- 312 MPa.

Rima Cardanus 1, a single fault, displays the best match between model and observations out of all grabens investigated here (Figs. 3.1, 3.2). The PYFM model matches observed slip distribution with a low SD (< 50m). The inelastic zone was modeled to display well matched fault tips between model to observed slip distribution. To produce this PYFM fit, we required a remote stress of 30 MPa and a yield strength of 114 MPa over a length of 72.5 m.

Rimæ Gerard, a comparatively short graben system of 115.3 km, with originally two individual faults (Fig. 3.3), was split into a total of five faults. Faults 2 – 5 (from the left) were in map view designated as 1 fault. Modeling the fault like this would have resulted in a model with extreme outliers and very high SD, leading us to split the fault into smaller faults that better reflect the observed displacements. We imposed the fault splits in locations where displacement was observed to be at local minima. All faults split locations coincides with jogs where faults linked. The structural map and previous findings are reported in Callihan and Klimczak (2019). The model solutions required a remote stress of 65 MPa and 253 MPa yield strength. One very large peak contributes the high SD of 99.2 m for the entire system, whereas the other faults have SD ranging from 37.0 m to 71.9 m.

Rimæ Mersenius, a 173.0 km long graben with two individual faults, were matched with three PYFM models (Fig. 3.3). The second fault in the system, stretching from fault length ~45 km to 173 km, to was split into two faults. The fault split location coincides with fault jogs in map view (Callihan and Klimkczak, 2019). The models

match the general overarching shape of the observed slip distribution and reflect the inelastic zone at the fault tips. Remote stress was constant for all faults at 35 MPa remote stress and a yield strength of 253 MPa. The overall standard deviation was 87.7 m.

Rima Cardanus 2, which is connected to Rima Cardanus 1 (Callihan and Klimczak, 2019), is a larger graben with a total length of 223.2 km, composed of 6 individual faults. The models for these short faults are particularly well-matched to the slip distributions. We produced three large fault model where the inelastic zone at the fault tips describes the slip distribution and produces a good agreement between model and observed slip distribution. The model displays three large SD of 188 m, 116 m, and 129 m respectively, which lie above the observed slip distribution and coincide with locations where fault linkage was suggested (Callihan and Klimczak, 2019). A remote stress of 35 MPa and yield strength of 140 MPa provided the best solution for this graben system and yielded a deviation of 57.9 m.

Rimæ Goclenius 1 (Fig. 3.3) with a total length of 1793 km has 9 individual overlapping faults. The slip distributions are well matched by the PYFM models. The inelastic zone at the fault tips was modeled to produce very good matches to the observed slip distribution. In order to achieve this fit, the remote stress was held between 42 – 130 MPa, and yield strength ranged from 164 – 507 MPa. The SD for this graben system from the produced model was 60.8 m.

Rimæ Goclenius 2 is a short graben system with a total length of 42.9 km and has predominantly short faults and low displacements. The models are generally well matched to the observed sip distributions. The model produced for the first slip distribution (on the left) has a maximum SD of 82 m in respect to the observed profile.

All loading conditions for this short graben were held constant at 78 MPa remote stress and a yield strength of 257 MPa. Standard deviation was recorded to be 41.3 m across the graben.

Rima Cauchy (Fig. 3.3), has a total of 10 individual recorded faults, with a total fault length of 204.8 km. Here we merged multiple fault lengths to produce a matching PYFM to collect the loading conditions at this graben. Two faults, near fault length 50 km, as well as the three faults adjacent to them were merged into a larger fault. The faults display individual segments in map view, but displacement profiles reflect mature displacement with D_{max} in the center of the total fault length (Callihan and Klimczak, 2019). The best-match model required a remote stress of 35 MPa and yield strength of 139 MPa, resulting in a 42.2 m SD from the observed slip distribution.

Rimæ Daniell, a highly segmented graben system with 13 individual faults (Fig. 3.3), has a total length of 264.7 km. Each individual fault segment has a best-match PYFM model. Shorter fault lengths reveal the best matches, whereas longer faults have slightly higher standard deviations. Multiple short, overlapping, faults are present between fault length 125 km and 250 km. Some large differences between model solution and observed slip distribution are located at the respective ends of the fault system. To produce a matching model to the observed profile, a remote stress of 58 MPa and yield strength of 225 MPa was necessary. A SD of 79.0 m was recorded for the entire graben system.

Two linked graben, Rima Flammarion and Oppolzer (Callihan and Klimczak, 2019), have a combined length of 282.9 m with this system representing one of the more complex PYFM arrangements (Fig. 3.3). Individual fault lengths are fairly similar to one

another here, except for the last fault in the slip distribution which comprises the last 13 km of the graben system. Even though individual fault lengths are generally similar, the displacement is different for each fault. Solutions to PYFM were specifically modeled to match the average displacement, resulting in values for remote stress of 45 MPa and yield strength of 175 MPa. Due to the irregularly shaped displacement profiles, a 90.7 m SD is recorded for the entire graben system.

Rima Hesiodus, the second-longest graben in the study has 15 individual faults and we produce 16 PYFM models to investigate loading conditions (Fig. 3.3). The last fault in the system (near graben length ~300 km) as split into two faults at the location of a jog in map view (Callihan and Klimczak, 2019), indicative of a location where fault segments coalesced. Any model solutions produced by the initially longer fault required displacements far beyond of our observations. All models closely match their specific observed slip distribution along general displacement. The remote stress required for the model solutions ranged from 50 to 230 MPa and a yield strength between 195 and 897 MPa. The overall SD for the 16 PYFM models was 51.9 m.

The graben in Schrödinger basin has three very large peaks that sit well above the average displacement (Fig. 3.3), influencing the model shape. Models for this complex fault system were challenging to produce, and we selected four PYFM solutions that best fit the overall fault shape, generally disregarding the extreme peaks found along the faults. To reflect these sharp peaks in the slip distribution we chose models that are higher than the remainder of the observed displacement. Remote stress was varied from 65 to 200 MPa, with a yield strength of 256 to 783 MPa. The presence of these peaks affected the he SD, which was the highest of all models with 254.2 m.

Rima Ariadaeus (Fig. 3.3) has one of the highest displacements found amongst these graben, with a maximum displacement of 1022 m. We found that a yield strength of 167 MPa and a remote stress of 50 MPa produced the best-matched PYFM model. Each individual fault in the system displays a generally matched model with the observed slip distributions. At the start of the graben system, the first observed fault slip distribution lies slightly below the PYFM model, whereas the two subsequent faults larger faults reflect the general model shape. It's possible to produce a model for the entire graben system, by combining all faults into a large complex, but that produces a model with extremely high SD. In the overlap zone between the two long faults, displacement is higher and skewed, resulting in the observations departing from the model. For all three faults the SD is 191.8 m, which is large compared to most other graben systems, but was produced to reflect the higher fault offset where linkage occurred, as well as the overall large amount of displacement.

The longest graben system in this study, Rimæ Sirsalis, has a total of 10 faults recorded from map view and we produced 11 corresponding PYFM model solutions (Fig. 3.3). The longest fault in the system (at graben length of ~200 – 400 km) was originally recorded as one long fault, in which a section was covered by ejecta blankets from adjacent craters (Callihan and Klimczak, 2019). The best-suited model required the split of this fault. The model required a remote stress ranging from 50 to 250 MPa, with a host rock yield strength of 195 – 975 MPa. Overall, the models provide good matches to the observed slip distributions, and only two faults, between fault length 100 – 200 km, display higher deviation between the two. The SD for this system is 140.1 m.

In summary, all of the PYFM model solutions we produce generally match the shape of observed slip distributions. The inelastic zone is modeled such that it produces very good agreements along the fault tips for observed slip distributions and models. Generally, deviations from the model occur where faults show peaks in displacement. This occurs where faults link or topography or mechanical layer thickness influences displacement (Callihan and Klimczak, 2019, Chapter 2). We also observe that some faults had to be split into multiple faults and others had to be merged to produce fits that are representative of the general graben. This means that some of these faults could be reinterpreted on their fault length. The faults that were merged, are interpreted to be longer, indicating that they may be linked. The faults that had to be split into smaller sections may need to be reinterpreted as individual faults. Overall, we produced 89 individual models to fit the observed slip distributions, which inform loading conditions and rock strength properties that can be further investigated. Loading conditions ranged from 30 – 350 MPa, and rock strength properties ranging from 114 – 975 MPa over the life of these faults. Using this information, we can further investigate the evolution of these faults and the host rock surrounding the fault plane.

Evolution of fault growth

By producing individual PYFM model solutions for each fault, we observe not only how the fault systems bounding lunar graben evolved, but also how the loading conditions change as a function of fault segment length for different locations. We fitted 89 models, and from there were able to extract σ_r and σ_y for each individual slip distribution, model pair. Combined with their respective fault segment lengths, we can further analyze this data and describe how conditions change with fault growth. We are

able to apply this methodology for fault evolution because, fault length represents a measure of time. Faults grow via accumulation of slip events, meaning that faults grow longer over time from short to long faults, implying that short faults can be interpreted as young faults, whereas long faults are older. This relationship can be affected by impediments to fault growth, such as strain partitioning and localization, but the general relationship remains.

The PYFM model analysis reveals that 9 out of 14 graben-bounding master fault systems achieved good fits by applying constant remote stress on rocks of constant yield strength within the fault system. Figure 4 displays remote stress and yield strength of individual faults for constant loading conditions (Fig. 3.4A) and loading conditions that evolve over time with increase in fault length (Fig. 3.4B). Individual faults experienced a remote stress of 30 to 78 MPa for faults slip to occur and displayed a yield strength of 114 MPa to 257 MPa (Fig. 3.4A). We observe that model solutions of shorter faults require higher remote stresses (Fig. 3.4, e.g., Gerard) in comparison to faults of longer lengths (Fig. 3.4, Cardanus 2).

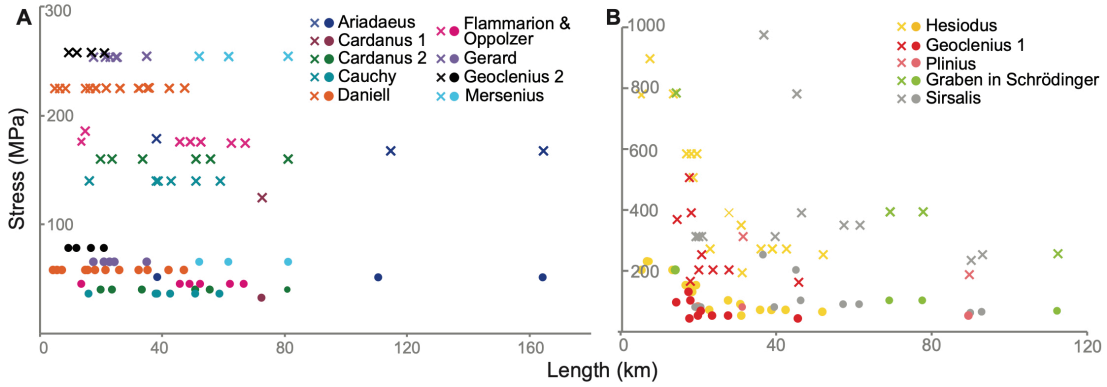

Figure 3.4 Modeled loading conditions plotted for 89 lunar graben-bounding normal faults, color-coded by fault system. (A) All individual fault segments, where yield

strength (crosses) and remote stress (circles) were constant to produce PYFM model solutions to match observed slip distributions. (B) Fault segments that display remote stress and yield strength decreasing with increasing fault length.

These loading conditions occur independent of total master fault length, which ranged from 72.5 km to 304.8 km. Rimæ Gerard, Rimæ Daniell, and Rimæ Goclenius 2 display short individual faults (<40 km) and have the highest remote stresses associated with fault growth (Fig. 3.4A, Table 3.1). Rimæ Mersenius, with slightly longer individual fault length, requires as similarly high remote stress for propagation as Rimæ Gerard, Rimæ Daniell, and Rimæ Goclenius 2. Rima Ariadaeus requires a remote stress of 50 MPa for continued fault slip, but also represents the longest graben that exhibits constant loading conditions. Rima Flammarion & Oppolzer, Rima Cardanus 1 & 2, and Rima Cauchy range in remote stress from 30 MPa to 45MPa (Table 3.1). The faults that propagated under constant conditions are located across the lunar highlands, mare, and transitional terrain types and display mare-concentric and mare-radial orientations. We previously identified systematic relationships across lunar terrains, especially with respect to graben orientation surrounding lunar mare, but those relationships are not reflected in the loading conditions.

The remaining 5 out of 14 graben-bounding master fault systems achieved matches by applying decreasing remote stress and material yield strength with increasing fault length (Fig. 3.4B). These individual faults require very high remote stresses for short faults and decrease in yield strength considerably as faults grow longer. Rimæ

Goclenius 1, Rima Hesiodus, Rimæ Plinius, the graben in Schrödinger basin, and Rimæ Sirsalis, display host rock yield strengths ranging of up to 975 MPa for short faults under 40 km, decreasing to yield strengths of 165 MPa as fault length increases (Table 1). These are cumulative values calculated for the lifetime of the fault. The remote stress required for short faults averages around ~70 MPa and is as high as 250 MPa. As fault length increases remote stresses decrease to as low as 42 MPa. We note that there is a smaller number of long faults in each individual graben system. For Rima Hesiodus and Rima Goclenius 1, more than 80% of faults are shorter than 40 km, and only a total of three long faults over 40 km lengths exist in the master fault system of both of these grabens. The fault segments within the master fault system for graben in Schrödinger basin are predominantly long, but a decrease in loading conditions with increasing fault length is apparent from the PYFM modeling. Rimæ Plinius has only two faults and displays the same inverse relationship of increasing fault length and decreasing loading conditions. These grabens are found in highlands, basins, mare terrain, but do not occur in highland terrain (Callihan and Klimczak, 2019). They are oriented perpendicular, as well as concentric, around mare basins, but yet do not reflect systematic relationships identified in our previous study (Callihan and Klimczak, 2019, Chapter 2).

Fault rock evolution

Faulting occurs when two fracture planes are loaded such that the frictional resistance to sliding is overcome. Furthermore, fault growth, i.e., the growth in shear displacement and length, involves the formation of small fractures at the fault tip that gradually merge to form an immature, discontinuous, irregular slip surface. This fault growth, also analogous with time, allows us to draw conclusions over the lifetime of a

fault. Loading conditions identified here, represent the averaged values over the lifetime of the fault segments. We assume that longer faults and short faults within the same graben represents different stages of fault evolution, but we are unable to discern individual slip events.

With continued slip events, this slip surface begins to smooth, and fault gouge forms (Cowie and Scholz, 1992b). As time progresses and further slip occurs, the fault plane becomes more developed, as does the fault gouge. The frictional resistance to sliding is highest at the immature fault tips, where the gouge is not or poorly developed, and decreases towards the mature parts of the fault, which is commonly found at or near the location of maximum displacement where gouge may be well developed. In an established fault plane the frictional properties are largely influenced by the fault gouge (Scholz, 2002). As faults grow larger, slip across the fault plane can be accommodated easier. Fault gouge can affect friction, by influencing state or rate of friction, which depends on the actual character of the gouge itself, such as grain shape, size and amount of interlocking or uniform grain size (Schultz, 2019). Ultimately, fault gouge can either promote or impede friction on a fault surface.

During faulting the slip velocity (rate of slip) plays a role on rock friction (Scholz, 2002; Ikari et al., 2011, Schultz, 2019). When slip velocity is increased, the rock experiences an immediate increase in friction. Friction can also experience a healing effect, where friction assumes a steady state value after re-initiation of sliding with higher frictional parameters. Fundamentally, friction depends logarithmically on sliding velocity. For fault growth this means that initially friction will increase, inhibiting slip, but once frictional resistance has been overcome, friction lowers and makes it easier for

faults to slip. Once faults have formed, they represent planes of weakness that display less frictional strength than was required to form them (Scholz, 2002). Faults can experience both velocity weakening and velocity strengthening. The physical state of the fault plane and slip velocity effect lunar fault growth, and both are tied to frictional strength of the fault plane. Applying the PYFM model enables us to better understand not only the loading conditions, but also the rock strength surrounding the fault plane.

Previously, Cowie and Scholz (1992) suggested four end member solutions to fault growth as explained by PYFM and our study represents the first test using natural observations. These end members directly link the remote stress acting on the fault plane, the yield strength immediately surrounding the fault, and the shape of the fault including that of the inelastic zone as a function of fault size. The first end member exhibits σ_y constant, whereas σ_r decreases with increasing fault length, s and d_o decrease over time. A second end member also shows constant σ_y, but σ_r increases with fault lengths, resulting in s and d_o increase over time. For the third end member, σ_y show linear increase and σ_r is held constant, also causing s and d_o to decrease over time. The last end member solutions is under constant σ_y and σ_r, with linearly increasing trends of s and d_o *with* increasing fault length. Their most physically reasonable solution, the fourth end member, corresponds to our PYFM model solution of constant stresses (Cowie and Scholz, 1992b). Additionally, in our study we identified an additional, new, PYFM model solution, where stress conditions decrease over time. Both scenarios are further interpreted below.

Overall, we have found that PYFM solutions from this study reveal host rock material strengths of 100s of MPa, which is consistent with previous predictions (Cowie and Scholz, 1992b). Figure 3.5 displays both PYFM model solutions that are present in

the graben studies here utilizing Rima Cardanus 2 and Rima Hesiodus. The left column (Fig. 3.5A, D) highlights how loading conditions and yield strength for the fault systems change over time, the center column (Fig. 3.5B, E) shows their respective D_{max}/L scaling relationship. The last column on the right (Fig. 3.5C, F) shows how s, d_o, and overall displacement change over increasing fault length from time 1, t_1, to time t, t_2. The new parameters introduced in Fig. A, D, relate to σr and σ_y and account for applying this model initially intended for cracks on faults (Cowie and Scholz, 1992b). The yield strength is equated to the macroscopic shear strength, σ_o, which is related to the stress at which rock begins to fracture. The frictional resistance, σ_f, is the resistance to sliding, which is largest at the fault tip, but beyond fault tips the σ_f is determined by the fault gouge. The remotely applied shear stress loading the fault is equivalent to σ_a. Using these parameters, σ_r now becomes $(\sigma_a - \sigma_f)$ and σ_y becomes $(\sigma_o - \sigma_f)$. Using these parameters allows us to interpret the evolution of frictional stability of the fault zone.

For the PYFM model solutions, where remote stress and yield strength remain constant across all fault lengths, such as represented by PYFM solutions of Rima Cardanus 1 (Fig. 3.5A), the relationship between D_{max}/L is constant, linear, and displacement increases with fault length (Fig. 3.5B). In the example of Rima Cardanus 1, the modeled scaling exponent for displacement to length is 1.24 and an R^2 value of 0.91, indicating linear growth. Considering the individual PYFM model solutions (Fig. 3.5C), the dimensions of the inelastic zone, including d_o and s, increase linearly with fault length over time. Based on the linear growth in Fig. 3.5B, we can interpret that all faults, small and large faults are similar in shape (fractal behavior), meaning that displacement and length grow relative with another. This means that these faults exhibit the behavior that

shorter faults represent shorter growth (t_1), whereas longer faults require longer time to grow (t_1).

From this analysis we deduce that the frictional properties on the fault remain constant as fault growth continues over time. We interpret that this type of fault growth on the Moon is driven by stable sliding, where displacement accumulates at a constant rate and fault slip occurs continuously. This also may suggest that friction during sliding may be constant, and friction likely undergoes velocity strengthening. Stable slip would not require a high loading stress for fault growth and likely suggests that the material strength of the host rock is consistently low.

For the PYFM model solutions, where loading conditions and host rock change with fault length, and hence fault age, the fault system exhibits an inverse relationship to fault length (Fig. 3.5D). Both, the remote stress and yield strength decrease with increasing fault length (Fig. 3.5D). The relationship between D_{max}/L is sublinear, with a scaling exponent of 0.25, and, in the example of Rima Hesiodus, has an R^2 value of 0.42 (Fig. 3.5E). Again, with increasing fault lengths, and thus time, displacement increases, and the size of the inelastic zone increase, but at an increasingly slower (sub-linear) rate. Based on the growth profile we observe in Fig. 3.5B, we interpret that small and large faults are not similar in shape (non-fractal behavior). Shorter faults will display a higher displacement in comparison to displacement in long faults. Of course, faults with longer displacement will overall have a higher displacement, but the fault growth itself with increase in fault length will be disproportionate. If short faults represent shorter growth time and long faults require longer time to grow, then this is how they compare in shape. This also highlights that short faults represent early stages in fault evolution.

Additionally, to all these parameters, frictional resistance to sliding is also changing as a function of fault length, and thus time.

The behavior exhibited by these faults suggests that frictional properties behave in two ways. Frictional properties remain constant over the lifetime of a fault, or frictional properties may evolve. We cannot make any assumptions on how these properties evolve, But our interpretation allows for changes in fault rock strength (e.g. frictional stability).

The general relationship between frictional stability and fault strength has been studied with laboratory experiments by Ikari et al. (2011). These authors proposed that a systematic relationship between the absolute frictional strength and the potential for unstable fault slip exists. In their laboratory results, weak fault gouges exhibit only stable slip and appear to experience velocity strengthening, whereas strong gouges experience stable, as well as unstable, slip under velocity weakening (Ikari et al., 2011).

Overall this implies for the lunar normal faults that grow in the observed ways, that there are two different responses of the fault host rocks that could lead to different types of fault gouge formation. Fault growth under constant loading conditions and yield strength indicates that the fault gouge develops systematically across the fault over time, where generally fault gouge properties do not affect growth further. Fault growth under loading conditions and yield strength that decrease with time indicates that some change along the fault gouge may occur. First the fault may experience higher frictional resistance, hindering fault slip and promoting strong stick-slip conditions. Then the fault surface would wear over time, producing fault gouge that allowed for continued slip under lower loading conditions. Frictional resistance on the Moon might already be high due to the fractured nature of the lithosphere (Klimczak, 2015).

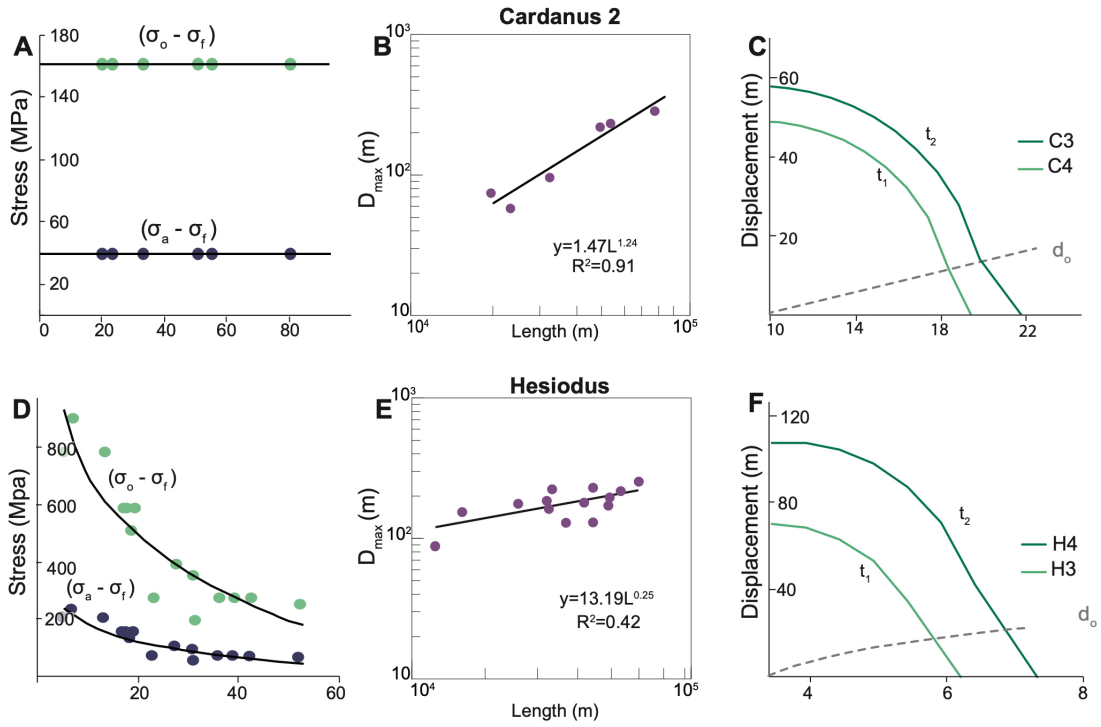

Figure 3.5 Solutions to PYFM model for lunar normal faults. The top row (A, B, C) show data collected from Rima Cardanus 1, whereas the bottom row (D, E, F) shows an example of Rima Hesiodus. (A) shows constant loading conditions and yield strength for Rima Cardanus 2, and (B) the linear D_{max}/L relationship for the same graben. (C) PYFM models for faults 3 & 4 in the system highlight a linear increase of s and d_o for Rima Cardanus 2. (D) shows decreasing loading conditions and yield strength for Rima Hesiodus with continued fault growth, while (E) displays the power-law D_{max}/L relationships for all faults in this graben. (D) PYFM model solutions highlighted using faults 3 & 4 in this graben shows an increase in s and d_o with increasing fault length over time.

Our study did not reveal any systematic patterns that would suggest that one mode is more prevalent in anorthositic highland vs. basaltic mare materials or transition zones with the exception that fault growth where stress and rock strength are decreasing over time is not found in any highland graben of our study. This implies that these types of fault growth may be influenced locally by different host rock characteristics such as mineralogy, degree of lithospheric fracturing, and size distribution of the fractured rock. Additionally, the grabens are widely distributed across the lunar near-side and may not be part of the same fault population (Callihan and Klimczak, 2019).

In addition, remote stresses may have been caused by a multitude types of tectonics across the lunar surface. Grabens have been interpreted to have formed during extension likely linked to the cooling of lunar maria (Lucchitta and Watkins, 1978; Watters and Johnson, 2010; Klimczak, 2014) leading to contraction of the mare units, forcing the surrounding regions into an extensional stress regime (Melosh et al., 2013). These regions generally correlate with the locations of the graben investigated in this study. Overall, the identified that none of the grabens located in the highland terrains display fault growth via decreasing loading conditions and yield strength. Beyond that we were not able to detect any systematic patterns with respect to spatial distributions of the graben vs. fault growth behavior categories.

Graben formation has been linked with and suggested to be a direct consequence of dike intrusion (Head and Wilson, 1993; Wilson et al., 2011; Klimczak, 2014; Callihan and Klimczak, 2019). Multiple mechanisms have been suggested to create favorable extensional tectonic stresses for dike intrusion, which may also be linked to graben formation. Graben analyzed by Klimczak (2014) that have been suggested to display dike

signatures and are also discussed in this study are Rima Ariadaeus, Rimæ Daniell, Rima Hesiodus, and the graben in Schrödinger. These graben equally fall into both categories of fault growth discussed here and we currently cannot observe a relationship between fault growth modes and dike intrusion.

Lunar mascons and mare-imposed loads (McGovern and Litherland, 2011; Thomas et al., 2015), lithospheric loading caused by a flexural response due to shield volcanos (Spudis et al., 2013), and deformation caused by mare loading combined with local crater stress fields (Michaut et al., 2016) have also been used to explain regional extensional tectonic stresses that would aid in graben formation. Any of these factors may have acted individually, or in concert, to produce combination of remote stresses for the observed fault growths. Currently, there is no relationship apparent from the visual assessment of mascon locations in relation to faults. Future careful geospatial analysis may provide answers on and if these mascon and mare-imposed loads and fault growth are linked.

Conclusion

Our study is the first study that has modeled a total of 89 fault slip distributions and matched them to previously collected observations of normal fault systems for 14 graben systems on the Moon using a post yield fracture mechanics (PYFM) approach (Cowie and Scholz, 1992b) to better understand the loading conditions and host rock strength of the faults and explore implications that arose for the fault rock evolution. We find that short faults require higher remote stress to propagate in comparison to longer faults and the faults studied here grow in two different manners. Out of 14 grabens, 9 master fault systems exhibited constant loading conditions and yield strength, regardless

of fault length, whereas five these master faults systems are found to decrease loading conditions and yield strength with increasing fault length. First and foremost, this means that there are two ways fault slip distribution changes over time. The slip distributions either have the same shape over time, from short to long faults, growing proportionally, or the shape of fault slip distributions changes over time. In that case, short slip distributions will have a different shape because of disproportionate growth, where shorter faults will have a respectively higher displacement than longer faults. We suggest that frictional properties during fault growth change or remain the same for long lunar graben. This may imply that fault gauge either forms systematically, not affecting fault growth, or that it fault gouge properties evolve over time to facilitate further slip.

In the future these results can be used to further interpret faulting on planetary bodies and aid in the understanding of how fault growth is affected by host rock strength properties.

Acknowledgements

This work was supported by the Lunar Data Analysis Program under grant NNX15AP91G.

CHAPTER 4

INVESTIGATION OF TOPOGRAPHY ACROSS THE KING'S BOWL RIFT, CRATERS OF THE MOON NATIONAL MONUMENT AND PRESERVE, IDAHO

---

[1] Melanie B. Callihan, Christian Klimczak, Roger C. Lowe III, Cash A. Owens, Paul K. Byrne. To be submitted to *GSA Bulletin.*

Abstract

The formation of the 10 km long King's Bowl rift system and basaltic field, part of the Craters of the Moon National Monument and Preserve, Idaho, has long been attributed to the intrusion of a subsurface dike. Hundreds of fractures parallel a north-south oriented eruptive fissure symmetrically to the west and east. Newly collected field measurements provide evidence for the formation of fractures during continued intrusion and uplift of the region and before the eruption of magma from the central fissure. Data collected in the field highlights seven locations where fracture/lava interaction occurred, showing lava flow into fractures, lava flow surface deformation, and lava squeezed up through fractures. Orthographic images collected by an Unpiloted Aerial Vehicle were used to build high resolution orthographic image mosaics and Digital Elevation Models to further analyze the lava-fracture interaction and dike intrusion. These data products enabled us to extract and interpret the long-wavelength topography across the region, at a much finer scale than previously possible. We observe a 10 m rise with widths between 1.5 and 3 km that stretches across the general rift zone, which is indicative of the presence and extent of a subsurface dike. Numerical outputs of ground displacements of dike intrusions—modeled using the open-source USGS COULOMB code—are used for comparison with our observed topography to assess dike geometries. Results indicate that topography produced by dikes with previously inferred dimensions do not produce the observed rise. However, dike dimensions that produce fits to the topography require invoking surprisingly large dike apertures at shallow depth, which suggests a more complex subsurface arrangement of intrusive structures than previously thought.

Introduction

Dikes, near-vertical, magma-filled opening-mode fractures, cause very distinctive ground displacements and are commonly accompanied by additional structures, such as fractures, faults, and fissures. Evidence of this has been found across numerous locations on Earth (Pollard et al., 1983; Mastin and Pollard, 1988; Rubin and Pollard, 1988; Kuntz, 1992; Rubin, 1992; Kuntz et al., 2002; Holmes et al., 2008), but also on planetary bodies such as the Moon, Venus, and Mars (Head and Wilson, 1993; Ernst et al., 2001; Schultz et al., 2004; Head et al., 2009; Wilson et al., 2011; Klimczak, 2014; Callihan and Klimczak, 2019). Those dikes are frequently found to be associated with rift systems, highlighting the interplay of tectonic regime and igneous activity. The surface deformation is found to reflect specific dike characteristics, such as width, depth to intrusion, depth to magma source, etc., which can reveal estimated reservoir volumes and eruption mechanisms (Pollard et al., 1983; Mastin and Pollard, 1988; Rubin and Pollard, 1988; Holmes et al., 2008). In order to better understand these dike-related fracturing and eruption processes, and to apply them to other worlds in our Solar System, field investigations are key.

One of the best locations to study the effects of a shallow, surface-breaching dike on topography, fractures, pits, and faults is the King's Bowl (KB) rift, part of the larger Craters of the Moon National Monument and Preserve. Located in the Eastern Snake River Plain (ESRP) in southeastern Idaho, these volcanic units and structures are well preserved due to the arid climate and young (Holocene) age of the basaltic field, revealing a ~10-km-long rift zone. The KB rift is oriented ~10° NNW and lies within the much larger Great Rift, oriented parallel to extension in the Basin and Range province.

Previous studies have established the extent, character, and distribution of the field and its volcanism (Kuntz et al., 1986, 2007; Kuntz, 1989; 1992), most of which tied the existence of the rift and fractures to dike intrusion (Kuntz et al., 2002; Holmes et al., 2008, 2018). The basaltic lava flow extent varies across the area and total area extent covers ~ 3.2 km^2 (Kuntz, 1992; Hughes et al., 2018). This area is interpreted to represent the current record and extent of multiple fissure-fed magma eruption stages that formed and drained lava lakes and diverted flow lobes, leaving behind clear outlines of lava flow. Lava outflow lobes are identified across the region and tied to pressurized lava breaching existing levees (Hughes et al, 2008). Recent studies have updated volumes of estimated eruption amounts based on lava flow thickness measurements determined via topographic profiles. (Hughes et al., 2018). In general, the majority of eruption occurred near main rift near KB pit forming a large lava lake (Hughes et al., 2018) and smaller volumes of magma erupted near the northern and southern extent of the rift.

Numerous fractures along the rift seem to terminate at areas covered by lava flow or in places parallel them, bringing into question if lava flowed over existing fractures, if fractures post-date the lava flow but their propagation was impeded by the lava flow, or if they occurred contemporaneously. In the literature these fractures are also referred to as tension cracks, extension fractures, or joints. Previously these fractures have been studied in respect to rift kinematics tying into subsurface dike geometry. Kuntz et al. (2002) assumed that an ascending dike formed fractures followed by further upward dike emplacement and fissure eruption based on stresses inferred from emplacement models by Pollard et al. (1983). Even though this area has been the subject of multiple field

studies, we have not yet identified work that has specifically addressed the interactions between fractures and lava flow to investigate this hypothesis.

In recent investigations specific dike dimensions for KB have been proposed based on boundary and buoyancy equilibrium modeling (Holmes et al., 2008), but have not yet been tested by analyzing long-wavelength topography at KB. Up until now, the existing DEMs have been unable to reflect fine-scale topographic variations, but with the advancement of data collection using UAV new avenues of exploring long-wavelength topography have opened up.

In this paper we use field observations combined with UAV data to reveal new information on (1) timing relationships between fracture formation and volcanic eruptions, (2) if dike emplacement resulted in the structures and topography we see today, and (3) if previously hypothesized dike dimensions are reflected in long-wavelength topography. We use the results of this study to expand upon the known sequence of geologic events that include the fracture formation as linked to intrusion and eruption events. The observations from this study are directly relevant for and will aid in the understanding and future analyses of graben formation in other rift systems on Earth as well as other planetary bodies.

Geologic setting

The ESRP is located in the northeastern extent of the Basin and Range province and represents a structural and topographic depression. Here, Miocene deposits of rhyolite tuffs, ignimbrite, and tephra are overlain by ~ 1 km thick sequence of stacked basalt flows covered with sediments of Pliocene age. Since the Pliocene, the basaltic flows have been covered by a veneer of lacustrine, aeolian, and alluvial deposits (Greeley

and Schultz, 1977; Greeley, 1982; Kuntz, 1992). Different stages of basaltic volcanism were first proposed by Kuntz (1992), ranging from short term eruptions to fissure-type eruptions, intermediate, lava cone-forming eruptions and finally long-term shield forming eruptions (Kuntz, 1992).

Generally, fissure type eruptions in the ESRP are part of major linear volcanic rift zones, ranging from 30 to 100 km in length with widths between 3 to 15 km (Greeley, 1982; Kuntz, 1992). Fissure systems in the ESRP are generally oriented perpendicular to the Basin and Range province, but likely reflect local stress fields (Hughes et al., 2018). Throughout the ESRP, 8 Holocene lava fields are exposed at the surface, three of which, including KB, are located along the 85 km long Great Rift (Kuntz, 1992; Kuntz et al., 2007). Overall, the Great Rift represents an alignment of volcanic vents, fissures, fractures, and eruptive cones. The Craters of the Moon, King's Bowl, and Wapi basaltic fields are remarkably well preserved and easily recognizable in any satellite imagery because their basaltic composition is readily identifiable from the surrounding vegetated units (Fig. 4.1). The Craters of the Moon and Wapi basaltic fields are two larger basaltic flow fields to the north and west of KB rift, respectively. The KB rift is the smallest basaltic field along the Great Rift (Fig. 4.1).

The KB rift system is suggested to be part of an early stage of a low volcanic shield within the ESRP (Greeley and Schultz, 1977; King, 1977; Greeley, 1982; Kuntz, 1992; Hughes et al., 1999). The rift system is composed of a 7 km long central fissure and bound by parallel fracture sets to the west and east, spanning a total of 10 km (Fig. 4.1). The most recent lava flow of the KB rift system is dated to an approximate age of 2220 ± years (Kuntz et al., 2002), which is contemporaneous to the Wapi field along the

Great Rift (Kuntz, 1992; Kuntz et al., 2007). Eruption of basaltic lava occurred along the majority of the fissure and spread across the terrain with the total volume of lava estimated to be ~0.0125 km^3 (Hughes et al., 2018). Earlier lava eruptions from Inferno Chasm, a low basaltic low shield vent and channel, filled the topographically lower regions near KB, and resulted in formation of a topographic ridge ~3 km to the east of KB rift (Fig. 4.1) (Greeley and Schultz, 1977; Hughes et al., 2018).

At KB, 12 en echelon fissure segments are proposed to have erupted lava over a short period of time (Kuntz, 1992). The largest volume of lava extruded near the KB pit (Fig. 4.1), a 35-m-deep and 80-m-wide pit, located in the center of the main fissure, the origin of which is attributed to late-stage phreatic explosions and fissure wall collapse (Greeley and Schultz, 1977; King, 1977; Greeley, 1982; Kuntz, 1992; Hughes et al., 1999; 2018). Two small remnant spatter cones, Creons Cave and South Grotto exist to the north and south (Fig.4.1). Ejecta blocks can be found predominantly on the western side of the fissure, whereas fine tephra has covered portions of the eastern lava flow section near KB pit, as well as along a pit on the northern section of the KB rift (Fig. 4.1).

Dike geometry and topography

Numerous studies describe dike related topography and fracture or graben formation directly above them (Pollard et al., 1983; Mastin and Pollard, 1988; Rubin and Pollard, 1988; Rubin, 1992). The intrusion of a single, blade-like dike will result in the uplift of the region right above the dike, creating a rise that slopes away to both sides and produces faulting or fracturing along a narrow zone above the dike (Pollard et al., 1983; Rubin, 1992).

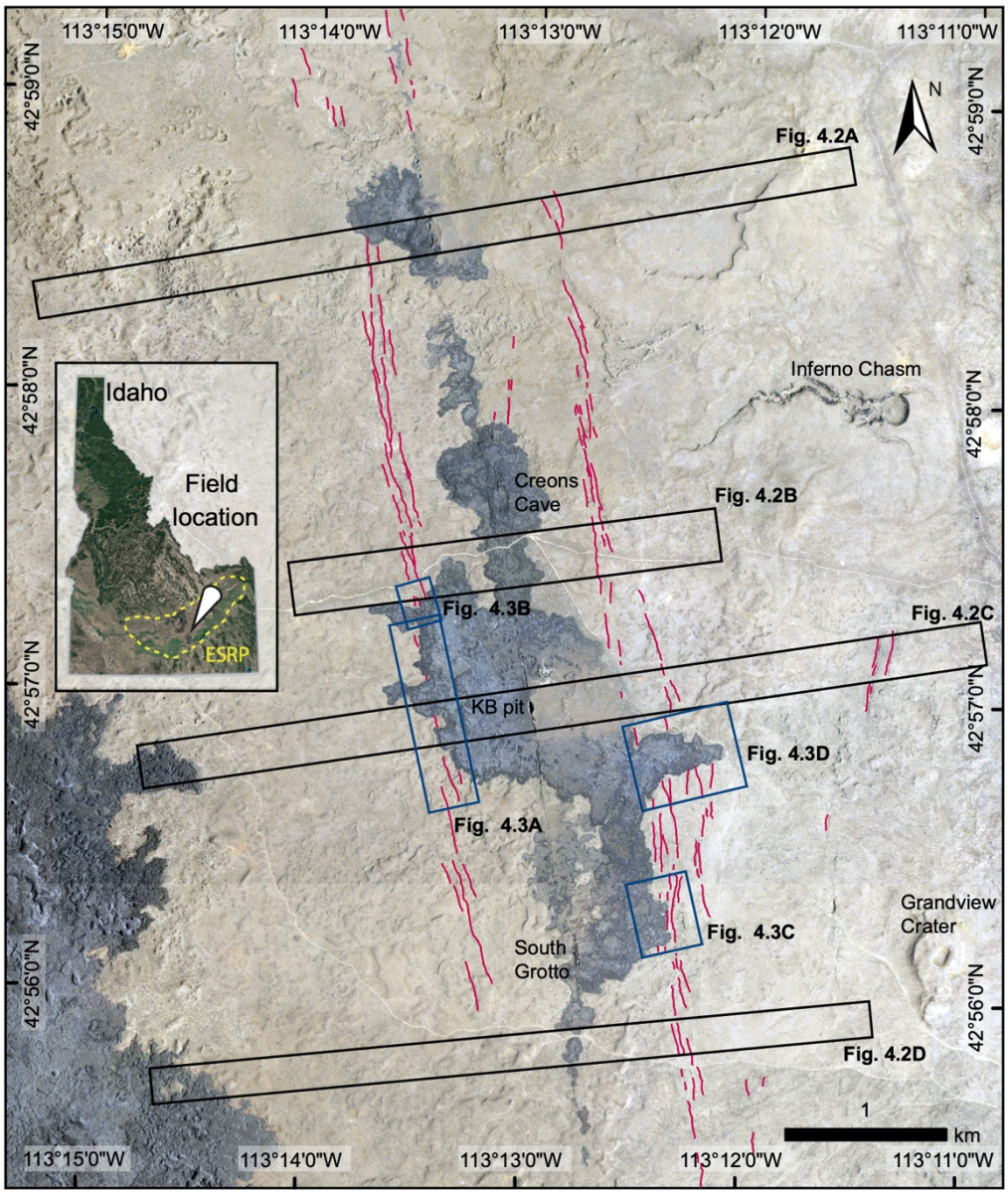

Figure 4.1 Photogeological overview map of the King's Bowl basaltic field located in the ESRP (yellow outline) of southeastern Idaho. A northwest trending fissure is bound by fractures symmetrically to the west and east (magenta lines). The central fissure fed lava flows, which are clearly visible from the underlying units by their fresh morphology and dark color in the photogeology. Note the tephra deposits to the east of KB pit and the northern pit appear as a lighter colored cover on top of lava flow surfaces. UAV flights

were conducted to investigate details of fracture/lava flow interaction (blue boxes) and long-wavelength topography (black boxes). Map uses 1 m National Agricultural Imagery Program data in a Transverse Mercator projection, centered at 113°13’0”W and 42°57’0”N coordinates.

This general topography stems from a broad region of subsurface compression, and a region reflecting tension above the dike, linking a zone of tension and fracturing at the surface directly to the extent and orientation of the dike. Once the dike propagates into the shallow subsurface up to a critical depth, at which tensile stresses exceed the strength of overlying rocks, the formation of fractures begins. Modeling has revealed that the critical depth is equivalent to half the average distance between fractures (Pollard et al., 1983) Additionally, boundary element modeling indicates that surface displacement created by dike intrusion favor graben formation (Mastin and Pollard, 1988; Rubin and Pollard, 1988).

Throughout all field and laboratory studies conducted, the KB rift has been attributed to the intrusion of a dike (Rodgers et al., 1990; Kuntz, 1992; Parsons et al., 1998; Kuntz et al., 2002; Holmes, 2005; Holmes et al., 2008). Holmes et. al. (2008) most recently used buoyancy equilibrium and boundary element modeling to estimate dike dimension and depths, utilizing the variable widths across the rift. The critical depth for KB rift is proposed to be at ~600 m beneath the surface (Kuntz et al., 2002; Holmes et al., 2008). As the rising dike intercepted and intruded above the critical depth, fracture formation locations began to migrate away from the rift. This process explains the

presence of multiple overlapping fractures (Fig. 4.1) (Kuntz et al., 2002). Results suggest the emplacement of a lensoid-shaped feeder at dike at an average depth to dike top of 633 m, with a total depth of 22 km and a maximum width of 8 m. Cumulative extension due to rift width is considered to range from 0.65 to 4.5 m (Holmes et al., 2008).

Even though, boundary element modeling suggests that dikes have surface displacements favoring the formation of graben directly above the dike (Mastin and Pollard, 1988; Rubin and Pollard, 1988), yet, at KB rift no such faults or graben are reported. It is unclear if at KB rift those fracture actually bound a very subtle topographic low to form a graben. Such a depression may be too subtle to be evident in the field but would be detectable in fine-scale topography. One explanation for the lack of vertical offset on fractures, which would transform the fractures into graben-bounding faults, is that the continued rise of the dike to shallow depths caused compression extending beyond the fracture zone. As intrusion continued, the tensional zone above the dike that allowed fracture formation, gave way to compression, therefore limiting any faulting (Kuntz et al., 2002). Lava flow formation at KB rift has been attributed to the breaching of the dike onto the surface (Kuntz et al., 2002), or to a dike that stalled at depth and eruption of lava caused by a smaller feeder dike (Holmes et al., 2008).

We hypothesize that these dimensions are sizeable enough for the KB fissure system to display dike-related topography and that this topography, which is too subtle to be observed in the field, can be detected with a detailed UAV campaign across the fissure. We model surface displacements of dikes for comparison with topography and assess if the dike-related topography affected the lava flow. Additionally, photogeology displays a multitude of conflicting observations between fractures and lava flow. Some

fractures appear to terminate at the lava flow, others appear to have been flowed over by lava, some locations show lava flow paralleling fractures (Fig. 4.1). Assessment of these fractures is crucial for a comprehensive understanding of the rift evolution at KB. We propose that these fractures predated lava flow eruption and evaluate if and how the dike-related topography and fractures affected the lava flow eruption and distribution.

Methods

To better understand mechanisms of dike-intrusion, dike-related topography, and the structures formed associated with the intrusion, we collected data using field observations and UAVs. We investigated long, rift-perpendicular regions and zones where fractures and lava flow were in direct contact along the rift zone to address outstanding questions on timing relationships between fracture opening and eruption. To search for dike-related long-wavelength topography we utilized UAVs to collect new fine-scale DEMs by designing UAV data collection campaigns, that would allow us to compute orthographic image mosaic and DEMs utilizing photogrammetry. We centered these UAV campaigns over critical regions of KB rift (Fig. 4.1).

Prior to the field campaign, fractures, fissures, and the prominent areas where lava flows and fractures interact were first mapped in digital mapping carried out in ArcGIS, using National Agricultural Image Program 1 m orthoimages (Fig.4.1). The mapping allowed us to identify specific locations of fracture/flow interactions that we targeted for field observations and UAV flights and plan out the field work. The methods for collecting observations and processing the UAV data are described below.

Field methods

From the preliminary mapping in ArcGIS, we identified areas of interest where fractures interacted with lava flows. We designate fracture/lava flow interaction locations as areas where fractures are in direct map contact with lava flows (for example Fig. 4.1, box Fig 3D). The preliminary map shows that fractures strike perpendicular or parallel to flows, and we identify five certain locations, where fractures and lava flows show superposition relationships. We targeted those areas for our field work, and they were subsequently imaged in high resolution using the UAV (see areas outlined with boxes in Fig. 4.1). In the field, we visited and walked the contact of each fracture/flow interaction location at KB, recorded the GPS coordinates and elevation, measured the length, spacing, depth, and character of the fracture using a measuring tape. Fracture orientations were recorded with a Brunton compass. We recorded flow heights at the interaction location, general condition of the lava flows and additional characteristics that were present at the area. Any evidence, or lack of evidence on the interaction between fracture and lava flow were recorded. Once we completed collecting extensive field sketches, photographs, and notes, we acquired high resolution orthoimages to produce fine-scale orthomosaics and DEMs across these areas of interest.

UAV Methods and processing

We used UAV technology to complement traditional field methods to obtain a better understanding of long-wavelength topographic variations as well as structure/lava flow interaction across KB. We investigated 8 targeted areas (Fig. 4.1), four of which represent km-long swaths perpendicular to the KB rift to better understand variations in topography and how they relate to the emplacement of the dike at KB. The northernmost

swath not only reflects long-wavelength topography but also shows one of the regions where fractures and KB lava interact. The remaining four areas of investigation were selected to highlight interaction between fractures and KB lava flow. Details of all UAV flights and collected data are listed in Table 4.1.

The northern, southern (near South Grotto), and central swaths (over KB pit) are the longest swaths across the rift, they are ~5 km long (Fig.1, Table 4.1). These dimensions were selected to capture variations in long-wavelength topography up to 3 km away on either side of the fissure. Each of these swaths were split into six individual flight missions, in order to comply with the Federal Aviation Administration (FAA) rule that an observer was able to maintain visual line of sight with the UAV and to accommodate battery changes efficiently. Each individual flight dimension ranged from 0.7 to 1km in length and swath widths between 240 to 340 m, resulting in a total of 18 individual flight missions. An additional swath was added south of Creons Cave with a total length of 2.7 km (Fig. 4.1). The four areas of interest that were flown to explore fracture/ lava flow interaction, are of different shapes and sizes (Fig. 4.1, boxes with blue outline). All of these missions were planned to capture the highest amount of fracture/lava flow interaction at very high resolution. Generally, all locations are aligned with areas of interest where lava flow is in direct contact with fractures.

Table 4.1. UAV flights analyzed in this study

Area of Interest	Number of Flights	GCPs	Length (m)	Width (m)*	Number of photos	DEM resolution cm/px	Orthoimage resolution cm/px	Pit	Fractures	Fracture /lava interaction	Figure number
KB North	6	38	5059	133	3468	5.78	2.89	Yes	4	No	2A
Creons Cave	2	9	2582	244	2050	4.42	2.21	Yes	5	No	2B
KB Pit	6	32	5311	130	3596	5.54	2.67	Yes	4	Yes	2C
South Grotto	6	32	4544	133	3902	5.51	2.76	No	3	No	2D
West long	1	6	1014	137	728	5.13	2.56	N/A	6	Yes	3A
West	1	4	244	159	326	5.23	2.62	N/A	6	No	3B
East lobe	1	4	573	451	1584	5.42	2.71	N/A	8	Yes	3C
Southeast	1	4	403	294	889	5.41	2.71	N/A	10	Yes	3D

*shortest width recorded for merged flights

We deployed a DJI Phantom 3 Professional and a DJI Mavic 2 Pro to collect orthographic images. Both drones were flown at variable altitudes (~ 53m and ~112m respectively) to accommodate differences in the imaging sensor capabilities such that similar resolutions in the end products would be achieved. Flights were pre-planned and programmed using Pix4D capture, using double grid missions that are suitable for producing 3D models. In general, flights were programmed for a ground sampling distance of ~ 2.5cm/pixel with camera angle of 80° (facing the ground), with 80% front and side overlap.

A total of 116 ground control points (GCPs) were used in the areas of investigation to enable us to produce high-resolution, georeferenced data products. Our GCPs, 12-in white paper plates, were temporarily installed to the ground using tent stakes and their respective location and elevation was recorded using a Garmin GPSMAT 64st GPS handheld system. For each individual area we dispersed between four and seven evenly-spaced GCPs depending on size of the flight mission throughout the area. Individual flight missions were planned so that overlap with the next area would ensure easier processing, leading to placement of at least one GCP within the overlap zone between flights. Overlap GCPs were only counted once for each swath, resulting in 116 GCPs that were physically deployed in the field. The number of GCPs placed in each swath is dependent on the total swath length, longer flights displayed higher numbers of GCPs. Once flights were completed, tent stakes and GCPs were removed and used for the next flight. The total number of GCPs is listed for each area in Table 4.1.

The individual orthographic images that were collected by the UAVs were processed with Agisoft's Metashape software. Images were uploaded, aligned to another

creating a sparse point cloud. Subsequently, the GCP locations were identified in the sparse point cloud and tagged in at least 15 to 40 images using the recorded GPS elevations and coordinates. The cameras were then optimized to reflect changes in georeferencing based on GCP locations. This allowed for all images to be positioned at the correct altitude. Once this step was complete, we produced a dense point cloud in Metashape which enabled us to create high-resolution orthographic mosaics and DEMs for all areas of interest (Table 4.1).

Image processing proved challenging at times, due to the extremely large number of images and flights that had to be aligned and merged to produce the final results. When encountering such problems, we pre-processed individual flights up to the georectified sparse point cloud before merging them into larger swath sections and ultimately producing the dense point cloud, orthomosaics, and DEMs, for the total areas outlined in Fig. 4.2.

Further processing and subsequent analysis of the orthomosaics and DEMs were conducted in ArcGIS, where hillshades were produced for all areas to highlight the topography of the areas and topographic profiles were extracted. Colorized terrain maps for swaths across the rift and locations for fracture and lava flow interactions are presented in Figs. 2 and 3, respectively. Small artifacts visible in the DEM are attributed to overlapping seams from flight processing.

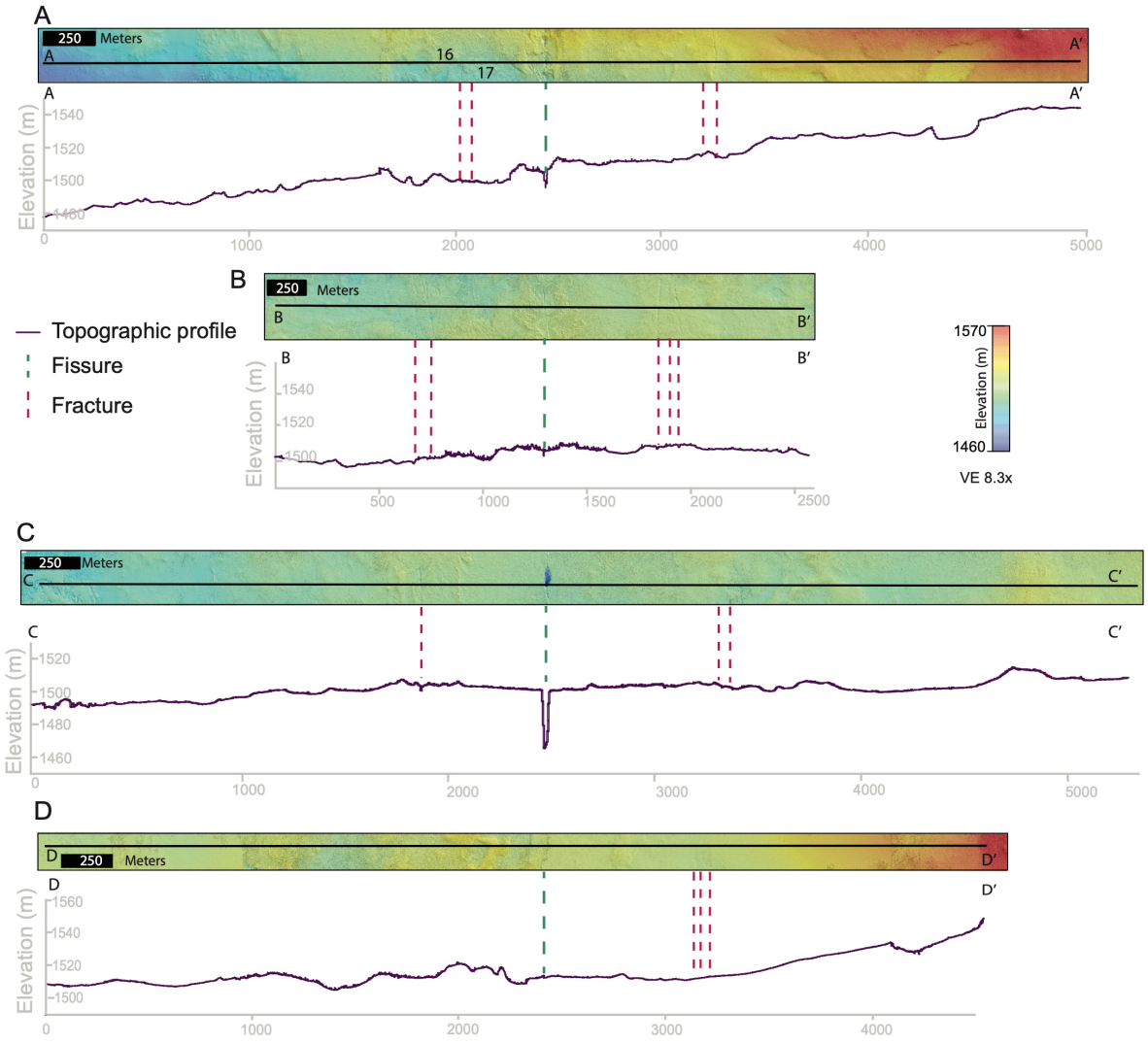

Figure 4.2 Colorized terrain maps of swaths and corresponding topographic profiles across KB rift. Terrain maps show UAV-derived DEMs overlaid on hillshade maps with an azimuth of 90° and incidence angle of 40°. Topographic profiles were extracted from cross sections lines along A–A' in the north, B–B' south of Creons Cave, C–C' across King's Bowl pit, and D–D' near South Grotto (Fig. 4.1). Terrain maps shown in Transverse Mercator projection are rotated for ease of viewing, their true orientation and geographic

context is shown in Fig. 4.1. All topographic profiles are show with 8.3x vertical exaggeration.

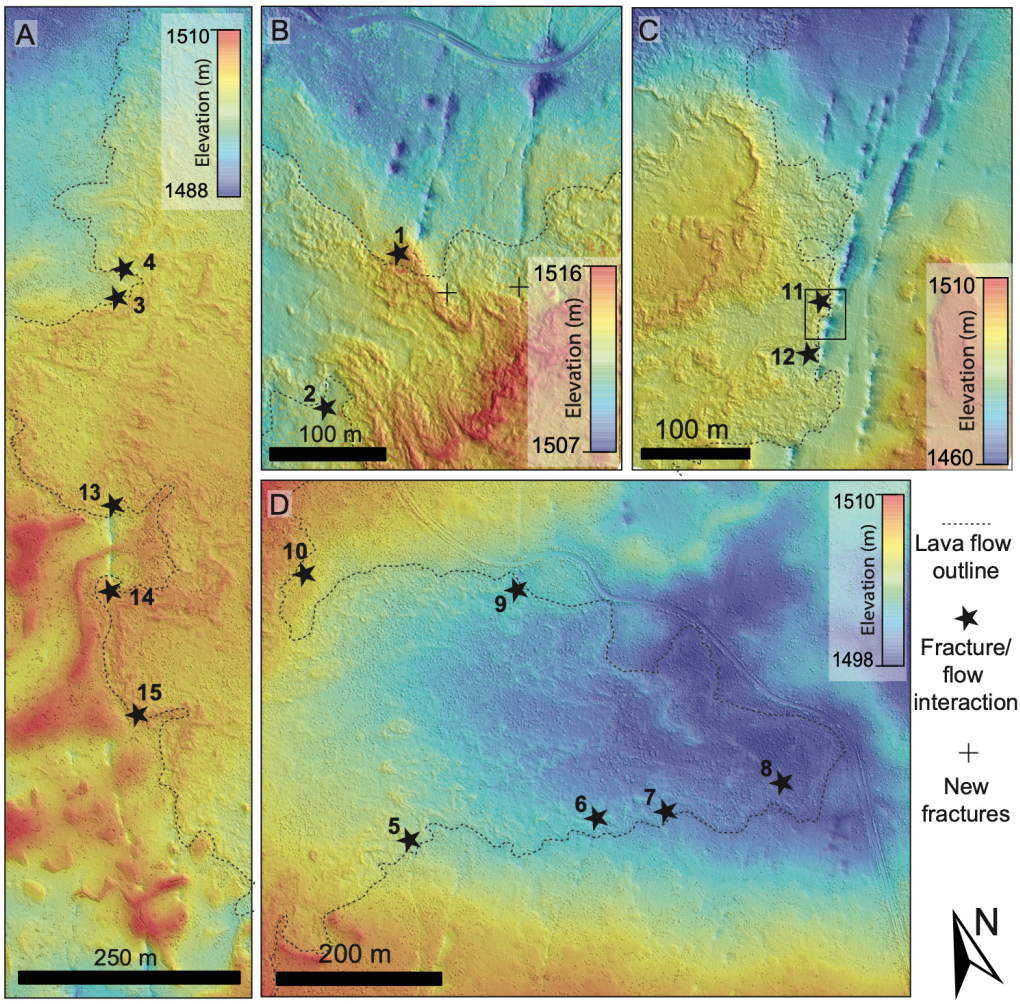

Figure 4.3 Colorized terrain maps of fracture/lava flow interactions. Terrain maps show UAV-derived DEMs overlaid on hillshade maps with an azimuth of 90° and incidence angle of 40°. Lava flow extent is outlined (dashed grey lines) and coincides with sites where interaction between fractures and flow have been documented (black stars). (A)

Terrain map of West long, showing fracture/flow interaction and highlighting preexisting lava flow channels from earlier eruptions. (B) Map of West, showing fractures terminating into lava flow. New small fractures enclosed by lava flow are located near flow margins (pluses) (C) Terrain Map of Southeast, displaying fracture parallel flow, lava tube overflow, and topographically lower set fractures. (D) East lobe terrain map reveals interaction surrounding all around lava flow lobe. Maps are shown in Transverse Mercator projection and are rotated for ease of viewing, their true orientation and geographic context is shown in Fig. 4.1.

Results

Fracture description

The KB rift is bound to the west and east by two parallel fracture sets separated by 1.1 – 1.8 km, over a length of 10 km along the rift (Fig. 4.1). Fracture orientations are generally similar to the NNW strike of the rift, but variations in strike of up to ~10° difference to that of the rift likely reflect local variations in the stress field. In general, the amount of fracturing reduces towards the northern and southern extent of the rift, displaying only one to two overlapping fracture sets, whereas near the rift center we find up to three to four overlapping fractures. Fractures occur in multiple en echelon patterns, with individual fractures ranging in lengths from tens to hundreds of meters (Fig. 4.1).

The fractures on the eastern side of the rift extend farther south, whereas the fractures on the western side of the rift extent farther north (Fig.1). Fracture spacing is

ranges from 13 to 90 m across KB rift. Most fractures overlap in varying lengths with other fractures ranging from tens to hundreds of meters. In a few locations, fractures link, forming V-shaped map patterns. This can be observed in Fig.1, just north of the road above fracture interaction flights and in Fig 3D, south of AOI-5. Our high-resolution orthoimage mosaics also reveal fractures within the region, that were previously unresolvable with the available data. We identified ~55 new fractures ranging in length from 1.5 m to 35.4 m. Interestingly, two new fractures are located in older terrain surrounded by inflated KB lava flow (Fig. 4.3B). One of these particular fractures aligns with other fractures that are in contact with the lava margin. The second fracture is aligned with the general orientation of the region but does not appear beyond the lava flow margins.

Fracture openings display typical opening-mode geometries, where fracture aperture taper towards the tips and displaying widest apertures at the half-length point of the fracture (Vermilye and Scholz, 1995). Fractures at KB rift occur in older, thick basaltic flow units, utilizing planes of weakness along polygonal cooling joints for propagation, resulting in vertical, jagged-or irregular shaped fractures at the surface (Fig. 4.4A). None of the fractures we investigated displayed any shear displacement along them, which is consistent with previous findings (Kuntz et al., 2002; Holmes et al., 2008). As also noted by previous studies (Kuntz, 1992; Holmes et al., 2008; Hughes et al., 2018), the fractures at KB rift are very well preserved, due to their young age and the prevalent arid climate in the region. Fracture walls can be classified as slightly weathered and maintaining their jagged or irregular shape from utilization of the preexisting columnar joint surfaces. Fractures with apertures that are wider than basalt

column diameter of ~0.2 -0.3m have columnar blocks fill in the fracture void space. Additionally, rubble and debris in the fracture cavities have been covered by loess to various degrees, but it is found in the majority of fractures. Measurements of fracture apertures, depths, orientations are listed in Table 4.2 for selected fractures that show interactions with the lava flow (see fracture/lava flow interaction section). The reported fracture depths in Table 4.2 are measurements from the surface opening to top of loess/rubble within the fracture. Minor physical weathering and erosion caused partial infilling of fractures, but also the lateral extent of fractures is occasionally obscured by loess deposits and overgrown, superposing the total fracture continuity and extent.

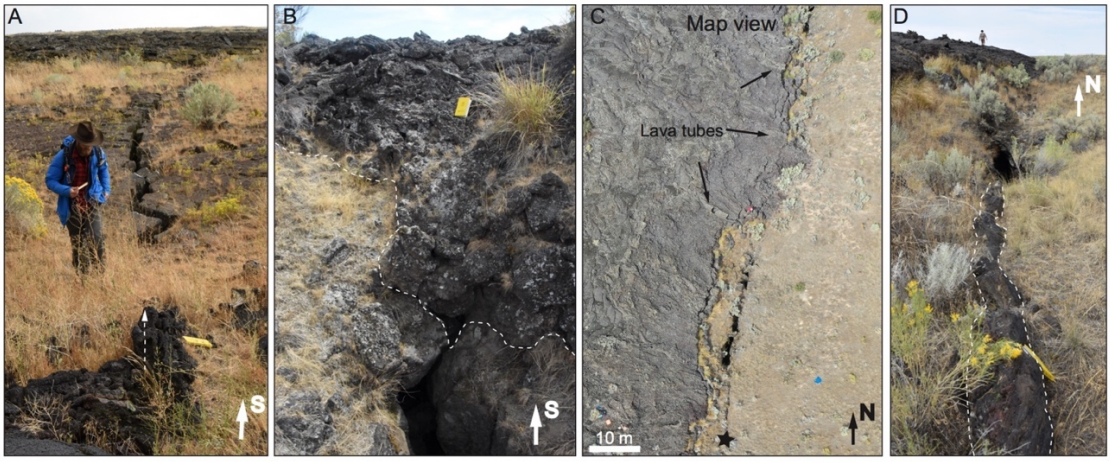

Figure 4.4 Field and UAV photographs of fracture and lava interaction at KB rift. (A) Fractures and lava flow utilize preexisting columnar joints to propagate. Linear lava flow surface deformation shows younger KB lava flow structures aligning with trend of fracture (dashed arrow). (B) KB lava flowed over the surface and into topographically low-lying fractures, partially filling them. (C) The UAV orthoimage shows flow-parallel fractures. Lava tubes provided conduits for fresh lava transported to the flow edges, spilling and

flowing into fractures. The star designates the location where photo (D) was taken. (D) lava squeeze-up along fracture. Note field notebook for scale.

Our DEMs reveal that the majority of imaged fractures are located in topographic lows, with those lows ranging in depth from one to three meters (Fig 3B, C). The topographic lows surround all fracture extent and gently slope towards the fractures. These lows are filled with varying amount of loess, rubble and vegetation. Only three locations (Fig 3A, near northern star) were found to show fractures in less pronounced topographic depressions. Topographic lows increase in depth and become more prominent along fracture sections that are wider. The topographic lows are less pronounced and display gentle slopes towards fracture tips (Fig. 4.3C) From these maps we are also able to observe that topographic lows can appear lense-shaped in maps view.

Lava description

Our observations on lava flow extent primarily concentrate along the flow margins, where lava flow and fractures are in physical contact. We observe lava flow heights ranging from 0.4 m to 2.7 m along fracture locations (Table 4.2). From field observations we have detected that the margins of flows can show ʻaʻā-type lava, rough in texture, but also have pāhoehoe ropey flow textures near the margins, attributed to lava flow lobes and deposition of pāhoehoe lava through lava tubes. The majority of lava flow heights in the area were consistently below one meter. The only exception to this was the eastern flow margin near South Grotto (Fig. 4.1 and Fig., 3C). The lava flow here was up

to 2.7 m in height, showing a predominantly blocky texture and multiple lava tubes carried and drained pāhoehoe lava into the fractures (Fig. 4.4C).

Fracture/lava flow interaction

The temporal relationship between fracture formation and eruption and flow of lava is best investigated at locations, where fractures and lava are in physical contact with one another. Our field work reveals that there are four systematic spatial relationships between lava and fractures present in the field. (1) We observe lava flows to stop at, or just before, a fracture and not show any signs of interaction (Fig. 4.4B). (2) Lava flows to, stops at, or just before fractures and lava morphology shows flow indicators that align with fracture orientation but there is no direct cross-cutting relationship between the two (Fig. 4.4A). (3) Lava is observed to flow into the fracture, filling the fracture void, and either stopping at the fracture or flowing beyond the fracture (Fig. 4.3-4.5). (4) Lava is squeezed up through fracture, leaving a positive relief morphology referred to as squeeze-up (Fig. 4.4D).

All of these observations have meaning for the temporal relationships between fractures and lava flow eruption. In observation (1), when the fracture stops before or at the lava flow, we cannot discern any specific timing relationships. For observation (2) lava stops before or at the fracture, and shows flow indicators that align with fracture orientation, signifying that lava flowed into an existing fracture, and flow patterns arose as lava filled the opening. This would place fracture formation before or consecutively with lava flow eruption. Observation (3) is similar in that lava is observed to fill into a fracture, which would require fractures to exist before lava flowed into the fracture opening. The last observation, (4), where we recorded lava squeezing up through a

fracture with remnant positive relief requires the fracture to exist before lava flowed through it. We have compiled our observations (detailed below), including lava flow height, fracture dimensions and orientations, depth lava flowing into fracture, and field notes pertaining to the interaction, for those four categories of relationships at 17 areas of interest (AOIs) in Table 4.2.

Table 4.2. Compilation of fracture/ lava flow interaction data collected

AOI	Latitude (N)	Longitude (W)	Fract. aperture at lava flow (m)	Fracture depth (m)	Fracture trend (°)	Flow height (m)	Infill depth * (m)	Fracture/flow interaction Description and notes
1	42°57'19.00"	113°13'28.00"	0.19	N/A	325	0.65		No interaction can be observed, no depression or inflow.
2	42°57'13.44"	113°13'30.60"	0.35	7.4	331	1.4		Obscured by vegetation, no linear trend, brecciation of lava. Depth measured at center of fracture.
3	42°57'3.06"	113°13'26.70"	0.16	2.28	323	0.4	1.54	Infill occurred, vesicular lava flow in between fractures of columnar basalt, fills 2/3 into the cavity.
4	42°57'3.79"	113°13'27.08"	N/A	N/A	323	0.33		Lava surface deformation, lava structures aligned with fracture (Fig. 4.5A).
5	42°56'44.28"	113°12'22.02"	0.40	2.79	345	1.18	1.57	Lava flowed into fracture, as well as into general fracture topographic low (Fig. 4.6 B), lava surface above is linearly aligned with fracture.
	42°56'46.02"	113°12'14.94"	0.43	0.34	356	1.04		Topographic lows have lava flowing down, fracture inaccessible, overgrown and rubble covered.
7	42°56'46.86"	113°12'13.02"	0.17	0.95	345	0.99		No evidence on flow surface or evident infill.
8	42°56'48.48"	113°12'7.56"	0.45	N/A	348	0.92		No evidence on flow surface, blocks have fallen in.
9	42°56'53.82"	113°12'20.40"	0.14	3.5	438	0.91		No interaction visible, no evidence on flow surface.
10	42°56'52.27"	113°12'29.78"	0.43	2.74	334	0.66		No clear evidence of interaction.
11	42°56'15.38"	113°12'20.08"	1.3	9.22	349	2.70		Lava tubes channelized flow over fracture. Access for measurement obscured (Fig. 4.5C).
12	42°56'13.84"	113°12'19.99"	0.73	9.22	349	2.74		Lava flow squeeze up structure (Fig 5 D).
13	42°56'55.53"	113°13'25.07"	0.48	16.76	327	0.83		Interaction not observed, deepest fracture observed and couldn't observe if it was deeper.
14	42°56'53.46"	113°13'24.41"	0.66	2.43	328	1.06	1.45	Flow filled into fracture; multiple drip structures observed.
15	42°56'48.57"	113°13'21.78"	0.20	1.85	331	1.01		Lava infill in topographic low and fracture, but could not measure drip structure, not accessible (Fig. 4.5B).
16	42°58'30.96"	113°13'47.25"	~0.3	N/A	350	0.99		Location covered by rubble and overgrown.
17	42°58'29.99"	113°13'44.55"	~0.1	N/A	335	0.95		Location overgrown and brecciated from host rock.

*only reported if present

The first systematic relationship we identified was that lava flows stop at, or just before, a fracture and not show any signs of interaction (Fig. 4.4B). In many locations where lava flow and fracture were in direct contact, we were unable to discern any patterns in the lava flow or the fracture that would indicate fracture formation before lava deposition or vice versa (Table 4.2). This is likely the case because of basaltic rubble, loess, and vegetation covering fractures. In locations where fractures were concealed by loess or lava flows, the extent of lava flows coincide with the topographic lows that we detected to be associated with the fractures. Fresh flows covered fractures without showing cracks in the lava surface that would indicate subsidence after flow deposition. (Fig.5 B). Some fractures perpendicular to the lava flow were fairly inaccessible due to fill and others terminated before the lava flow, and thus did not interact with the flow. Many fractures oriented parallel to flow also did not interact specifically with parts of the flow.

The second observation we made was that lava flows stop at, or just before fractures, and lava morphology shows flow indicators that align with fracture orientation but there is no direct cross-cutting relationship between the two (Fig. 4.4A). Some lava flow surfaces themselves also show evidence of fracture-flow interaction. In two locations we identified surface structures in the lava flow, directly juxtaposed to a fracture, with linear patterns oriented in the same trend of the nearby fracture (Fig. 4.4A). These structures were often of slightly higher relief than surrounding areas. The general vicinity of the flow showed typical amorphous flow structures but similar to ʻaʻā-type lava, but the locations directly in line with the fracture aligned with their respective trends, which may be attributed to the surface extensions of sub-surface flow.

In 7 locations we were able to identify areas where fractures show indicators that lava flow filled preexisting fractures, and either stopping at the fracture or flowing beyond the fracture (Fig. 4.3-5) (3). The most important of those observations is where we were able to record lava flowing into an open fracture, cooling and freezing in place, leaving behind drip-structures in the open fracture (Fig. 4.5). This was specifically observed and recorded in three locations at KB rift, with lava inflow depths measured to be ~1.5 m into the fractures (Table 4.2). Lava flow inflow is markedly different than the host rock basalt, generally, lava infill depth was ~1.5 m and did not fill the fractures to the soil top, but rather leaving void space in the fracture (Fig. 4.5). The lava that infilled into the fractures left solid, non-fractured flow behind. We did not observe any location where lava flowed over the fracture without filling in. Additionally, along the southwestern flow near South Grotto, we identified lava tubes that supplied lava towards the furthest edges of the flow, spilled lava over and into fractures (Figs. 4.3C and 4.4C). In these regions lava flow only partially covers/fills the fractures and it can be clearly observed that fractures continue north and south of the lava flow.

One of the fracture/lava interaction sites near South Grotto (Fig. 4.3C and 4.4D) exhibited a fracture squeeze-up structure. Here, in line with a fracture, a short, near vertical extrusion of hardened basalt extruded onto the surface. The structure stands 0.27 m vertically above the surface and is 0.17 m wide 7.5 m long. The squeeze-up is perfectly aligned with a longer fracture, separated only by loess-covered lava flow, making them likely part of the same structure.

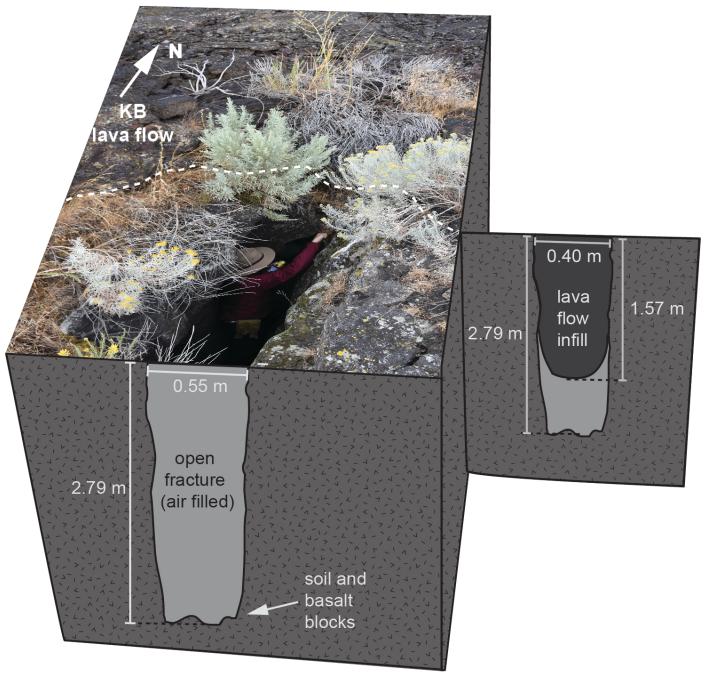

Figure 4.5 Block diagram of lava flow into an open fracture, with field photograph from AOI 5 (Table 4.2). Lava flowed from the north and over fracture, partially filling the fracture but leaving void underneath the lava.

Long-wavelength Topography at King's Bowl

DEMs are an integral part to our analysis and have been produced for all areas of interest for topographic analysis. We produced a total of 8 DEMs (Fig. 4.1), four of which were used for fracture analysis, covering areas to the west and east of the fissure where fractures were in direct contact with lava flow (Fig. 4.3). The remaining four DEMs were produced as long swaths perpendicular to the rift system. Although these long DEM swaths were designed for long-wavelength topographic analysis, they still cover areas over fracture and lava flow interaction and were applied in both types of

analyses. All these fine-scale DEMs reveal topographic variations at a very detailed level, highlighting small changes in surface topography, including detecting small vegetation, highlighting new fractures, and displaying new detail in topographic depressions. For the remainder of this section we will discuss the analysis of the long-wavelength topography across the rift system.

We extracted topographic profiles along the long axes of the DEMs of our swaths (Fig. 4.2). The profile positions were selected to capture fractures, pits, fissures, and other notable landforms of the area. Topographic profiles range in length from 2.6 to 5.3 km to ensure that both the long- and short-wavelength topographic nature of the KB rift was captured. The profiles show regional changes in topography relating to larger structures in the vicinity (but not captured by our imaging campaign), but also reveal small details that correspond with lava lake surfaces and tectonic structures. In general, we observe that topography is lower to the western extent and increases to the east. For each topographic profile, we mark the positions of the lava flow, fractures, and fissure, if present in the geology (Figs. 4.2, 4.6).

The DEM and resulting 5 km long topographic profile from A–A' along the northern KB swath, are centered over the northernmost pit, lava flow, and tephra deposit (Figs. 4.2A, 4.6A). The topographic profile shows a range of elevation from 1479 m to 1544 m. The topography gradually and consistently increases toward the east. The fissure and pit in this section show a depth and width of ~ 8 m and 12m, respectively. Directly to the east and west of the fissure is a raised region that becomes flatter with increasing distance from the fissure. The topography around the fissure is raised, which directly correlates with the superposed lava flow (Fig. 4.6A). Beyond the fissure and lava flow,

the topography is smooth, and two fractures are present on both sides. The remainder of the topography in the DEM shows volcanic landforms preceding the KB lava flow. There is a channel-like structure in the eastern section of the DEM and profile. This 207 m wide and ~10 m deep depression is tied to the evacuation of lava from a nearby small, unnamed shield volcano (Fig. 4.1). This feature is also linked to the general rise of topography to the northeast, where just 1.3 km and 2.5 km away are the locations of Cottrell's Blowout and Horse Butte, two volcanic vents in the area.

The DEM located just south of Creons Cave, is a much smaller, but wider swath that highlights very clear positions of the central fissure and fracture sets (Figs. 2B, 6B). The 2.5-km-long profile from B–B' gradually rises to the east and highlights a range in elevation from 1496 to 1508 m (Fig. 4.2B), which is a much smaller range compared to the other profiles. The fissure is located in the center of a broad rise (Fig. 4.6B). In particular, a subtle depression around the fissure is symmetrically flanked on each side by topographic highs (similar to our observation in A–A'), followed by bowl-like depression to either side. The extent of the lava flow does not coincide with the topographic highs (Fig. 4.6B), but small variations in lava lake surfaces are observable. These variations show small topographic elevation changes that align with ridges and levees remainders from lava flow. Fracture sets are present and can be observed as sharply delineated topographic lows to either side from the fissure in the DEM.

The DEM and 5.3-km-long topographic profile C–C' are centered over the KB pit and main extent of the lava flow (Fig. 4.2C, 6C). It shows a range in elevation from 1465 m marking the depth of KB pit, to 1514 m in the east (Fig. 4.2C). The lowest topography in the west is 1489 m. The terrain overall is fairly smooth. The KB pit shows a width of

37 m and a depth of 35 m at that particular location. The pit and fissure are located near the center of a topographic rise (Fig. 4.6C). The rise is spatially uncorrelated with the extent of the lava flow. Lava levee remnants and lava mounds are discernable in the topography as small spikes along the topographic profile. At the eastern extent of the DEM and profile, there is a peak that hosts two pressure ridges that formed as part of older volcanic units. At the westernmost extent of the DEM and topographic profile, the topography is rugged, as it covers the easternmost portion of the Wapi flow field.

The southernmost DEM and topographic profile we investigated is located just south of South Grotto (Figs. 2D, 6D). The 4.5-km-long topographic profile D–D' shows a range in elevation from 1504 m to 1541 m. This DEM and topographic profiles do not reveal a pit or gaping fissure at the location where the lava erupted. In contrast to the other profiles, there is no systematic topographic variation surrounding the fissure. A topographic high located 400 to 500 m west of the fissure are composed of remnant lava flow structures from older flows. The fairly smooth terrain on the western portion of the topographic profile is host to gentle depressions. The terrain on the eastern section displays a fairly steep topography increase, which we attribute to its proximity to Grandview Crater (King, 1982).

In summary, we observe a topographic trend reflecting a gradual, 1.6° to up to 6.8° sloping increase in elevation from west to east (Fig. 4.2). The most pronounced topographic variations covered by our DEMS are caused by volcanic landforms formed by previous structures. The two DEMs and topographic profiles in the center of the rift reflect a visually smoother topography across the area. All of the topographic profiles contain the volcanic fissure (or its remnant) that is the origin for the KB flow. The most

pronounced fissure and associated pits are located towards the center region of KB rift (profiles B–B' and C–C'). In three instances, the fissure is found atop a topographic rise that is not correlated with the extent of the lava flow (Fig. 4.6). Fractures, which display the previously described localized topographic low (see Fracture Description section), are identified on both sides of the fissure.

Dike Modeling

To compare our observed long-wavelength topography to that produced by dikes, we simulated static ground displacements caused by dike intrusion using the elastic dislocation code COULOMB (Toda et al., 2011) for previously proposed dike geometries (Holmes et al., 2008). The COULOMB code allows modeling of stresses and elastic deformation around fractures in an elastic halfspace following the framework by Okada (1992). Our models were designed to be 10 by 10 km in area, with a 10 m resolution to yield solutions for the ground displacement that would be detailed enough for comparison with our topographic data. We assigned a Poisson's ratio of 0.25, an elastic modulus of 25 GPa, and a coefficient of friction of 0.6 to the elastic halfspace. The calculation depth was set to 0 km to reproduce surface results. We then introduced one vertical fracture in shapes of tabular or tapered bodies and modeled the ground displacement caused by the opening of the fracture. On the assumption that erosion and topographic relaxation are minimal at the timescale since the eruption, the ground displacement would be reflected in the present-day topography. Parameters relating to the depth to dike top, dike width, and depth to dike bottom were selected for the corresponding locations of our profiles across the rift using previously published values at these locations (Holmes et al., 2008) as a starting point. We then modeled ground displacements that matched observed

topography and extracted dike geometries. The parameters are listed in Table 4.3.

For comparison to the simulated ground displacements, we used the same topographic profiles as described in Fig. 4.2, but detrended them and plotted them with geographic context removed, showing the location of the fissure at the origin of the diagram (Fig. 4.6). Topographic detrending was carried out by removing the above described regional slopes. The southern swath (Fig. 4.6D) displayed no discernable regional slope at the fissure and was left as observed. The eastern- and westernmost extents of this profile are also not shown in Fig. 4.6D.

We first modeled ground displacements for the dike dimensions at KB rift suggested by Holmes et al. (2008), who proposed an optimum of 8 m as dike width, 23 km depth to dike bottom, and a depth at which the dike stalled of 0.55 to 0.65 km (Table 4.3). These authors also suggested that a maximum dike width of 21 m would be possible at the KB rift, which we used for a second set of simulations for the comparison to our topography (Fig. 4.6, Table 4.3). Each of the simulated fits used the varying depths at which the dike stalled for the corresponding location along the rift/dike, as indicated in their publication (Holmes et al., 2008) and summarized in Table 4.3. Additionally, we also simulated ground displacements that matched more closely the observed topography, by varying all three parameters until a suitable fit was achieved for both (1) tabular and (2) tapered dike geometries (Fig. 4.6).

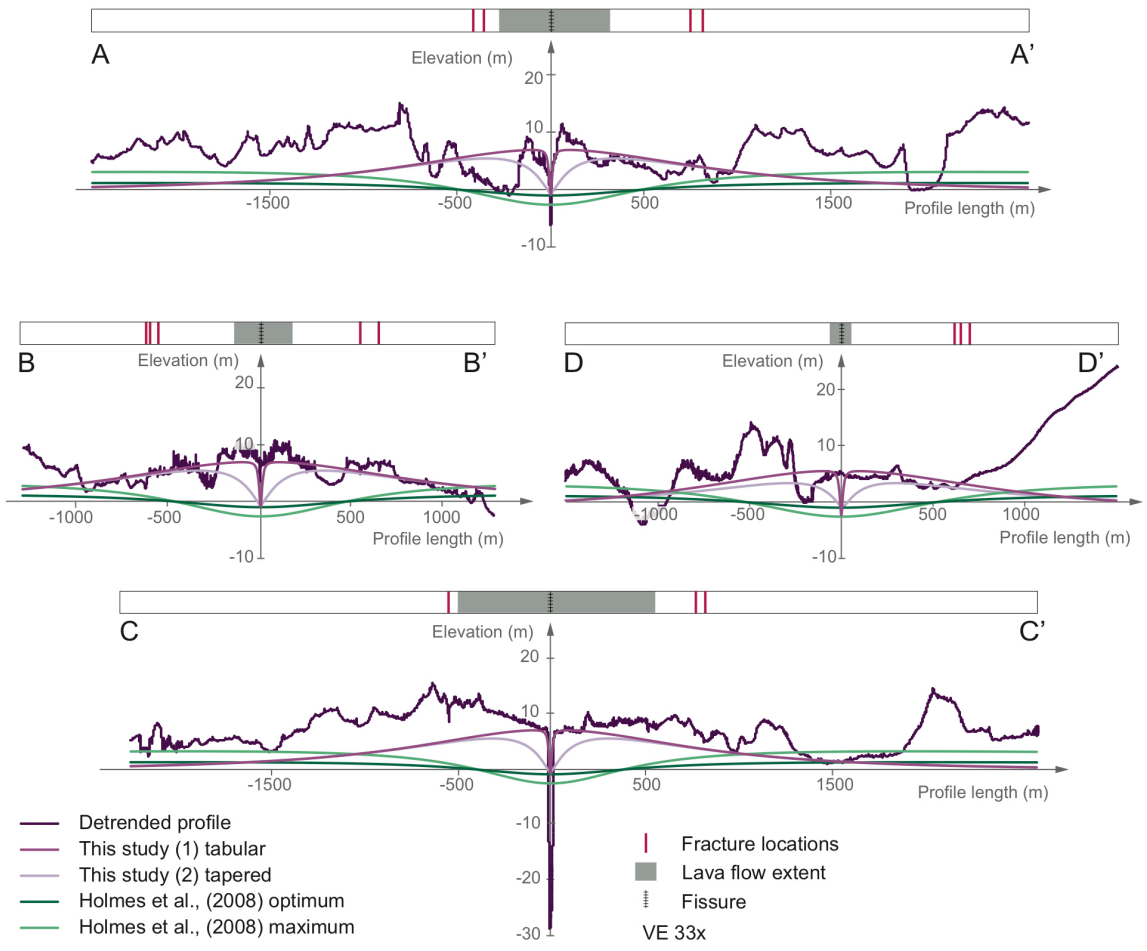

Figure 4.6 Detrended topographic profiles (dark purple lines) matched with simulated ground displacements of dikes across KB rift. Simulated ground displacement of varying dike dimensions are given for each profile and represent dimensions proposed by Holmes et al. (2008) (green lines) or better fitting ground displacements produced in this study (purple lines). Fissure and fracture locations, and lava flow extent are marked above each profile. All profiles correspond to profiles in Fig. 4.2 but are vertically exaggerated 33x for display of greater detail.

In general, the resulting modeled topography based on our dike geometries are smooth and symmetrical topographies. The dike dimensions proposed by Holmes et al. (2008) produce gentle, wide depressions near the center of the rift and marginally increase in elevation away from the central fissure. Most simulated fits based on these dimensions do not match the observed topographic profiles. The northern profile, AA' is the only region where these simulations reflect the shape of the observed topography, but yet do not match the observed elevation.

In contrast, the topographies simulated using our dike geometries show elevated rises near the center that taper off with increasing distance to the fissure. In the center of the elevated region a sharp depression is located directly in line with the location of the fissure in observed topography and display narrow and wide fissures (dike fit 1, 2 respectively). The individual fits for our dimensions are alike to the topography observed. The topography from AA' model reflects the general shape of simulated dike fit 1, including the topographic expression near the fissure. Whereas the tapered dike (dike fit 2) has a much wider slope along the fissure boundaries. Along BB', and DD' (Fig. 4.6) our simulated dike-induced ground displacements align with the observed topography, by matching a general sharp rise near the fissure and gentle sloping flanks to the west and east. For the topography along the profile CC' our simulated ground displacements (dike fit 1) display a general broad rise that ends at the exact inflection point of the observed topography. Dike fit 2, matches a similar topography but provides less of a match to observed topography due to the overall wider pit.

Table 4.3. Parameters used for simulations of dike ground displacements.

Dike fit	Dike width (m)	Depth to dike top (km)	Depth to dike bottom (km)	
Holmes et al., (2008) optimum	8	0.6	23.6	KB North (A–A')
		0.58	23.58	Creons Cave (B–B')
		0.55	23.55	KB Pit (C–C')
		0.65	23.65	South Grotto (D–D')
Holmes et al., (2008) maximum	21	0.6	23.6	KB North (A–A')
		0.58	23.58	Creons Cave (B–B')
		0.55	23.55	KB Pit (C–C')
		0.65	23.65	South Grotto (D–D')
This study (1) tabular	25	0.01	1	all profiles
This study (2) tapered	2	0.01	0.05	all profiles
	8	0.05	0.1	
	17	0.1	0.2	
	25	0.2	1	

Our simulations of tabular dike geometries produce ground displacements that most closely fit the observed topography only for dikes of unrealistic geometries (Fig. 4.6). The topographic rise on which the fissure is located is most closely matched by a 25-m-wide magmatic body found at unusually shallow depths to dike top and bottom, of only 0.01 and 1 km, respectively. We then accounted for the natural, tapered shape of an opening-mode fracture by tapering the dike tips. The uppermost portion of the dike was selected to have a narrow width, which was then widened with increasing depth. Our simulations of tapered dike geometries produce ground displacements that closely fit the observed topography for dikes that are 2 meters wide at 10 m below the surface, also widening to 25 m at 200 meters below the surface.

Discussion

Fracture formation

The data collected on the fractures and their interaction with lava flow at the KB rift helps us contributing towards understanding the processes and mechanisms that lead volcanic eruption there. Our field and UAV observations of fractures and fracture/lava interactions align with previous studies that fracture formation occurred before the eruption of lavas with multiple instances and types of fractures/lava flow interactions supporting this timing relationship.

Different observations would be expected for different timing scenarios. If lava flow either partially or completely solidified before fracturing occurred or if fracturing and lava flow occurred contemporaneously, we would expect fracturing of the lava or collapse of lava into the underlying fractures, due to lack of support underneath the cooling flow itself. This would result in clearly observable linear depressions across the lava flow terrain that flow over fractured regions. We would also expect certain regions along flow margins to be completely fractured and separated from the main flow. Instead, if lava flows reached the area after formation of fractures, one would anticipate lava flows flowing into fractures in regions where lava flows extended that far and likely also over fractures. Fractures may appear partially or completely covered. A possibility exists that some kind of cooling patterns or depressions linked to cooling would form above the fractures.

We have searched for evidence of both scenarios and have not identified any observations that would support the first scenario, where lava flow precedes or is contemporaneous with fracture formation. Instead, the observations we collected are

evidence for the latter scenario, in which fractures formed before lava flow reached them. Most importantly, we have documented multiple areas around the KB rift, where lava flowed directly into topographic lows observed to be around fractures and directly into fractures, filling the fracture cavities up to a specific depth of 1.5 m before lava solidified. Such filled and flowed-over fractures are found on both sides of the rift (Fig. 4B and Fig. 4.5), showing that this timing relationship holds true across the entire field area. Even though fracture aperture and fracture depth differ at the locations where lave infill is observed, the infill depth is consistent at 1.5 m. We attribute this constant depth as being related to the viscosity of the flowing lava flow and the constant distance of the fractures to the fissure. As the lava flow approached the fractures, it flowed into the fractures, and began to flow down, and due to increased surface contact, the flow became cooler and more viscous, arresting in place before it could reach deeper depths. As the fracture filled up to the surface, which may have occurred fast, it sealed the fracture underneath off and created a new flow surface, over which lava could spill across the fracture and leaving no room on the lava flow surface to form a depression just above the fracture.

Another indication of this timing relationship is the effect that fractures had on the flow itself. We also observed at least 2 locations where the lava flow surface showed linear flow fabric that aligned with the trend of fractures in immediate contact with the lava flow (Fig. 4.3A). Likely this is caused by lava flowing into the linear depression associated with the fractures, pooling and flowing within that linear depression, which would then lead to structures indicative of flow parallel to other nearby fractures. Unfortunately, none of these surface flow indicators were identified in locations where flow into fractures could be studied above and below the flow. Yet, the most remarkable

on of such fabrics (Fig. 4A, Table 4.2 - AOI 4), is located along the same fracture that also displays infill.

One of the most intriguing areas is the southeastern region (Fig. 4.3C and 4.4C), displaying two different types of interaction. Lava flow here flowed toward fractures, arrested and inflated, and flowed parallel to the fractures without flowing into them (Fig 4C). In locations where lave tubes formed, fresher pahoehoe lava was supplied to the flow margins, spilled over the flow margins and into the fractures (Fig 4C). In addition, a squeeze-up structure also formed where highly viscous lava squeezed out of the subsurface from within the fracture. The squeeze-up structure is perfectly aligned with the trend of the fracture next to it (Fig. 4C and 4D). Lava here must have flowed into the fracture, likely at a location further south, continued to flow inside the fracture, and was squeezed up at this location.

These observations together support that fracture formation occurred before the eruption of lava from the central fissure at KB. These rift zones were previously investigated by multiple studies, but timing of fractures has only been suggested to predate flow formation by (Kuntz et al., 2002). In this study, we collect and compile specific evidence that KB-related lava flows flowed into preexisting fractures. Similar occurrences have been identified elsewhere in the ESRP in Box Canyon (Welhan et al., 2002), where younger lava filled into open fractures set in older lava flow units and solidified before reaching the fracture base. Welhan et al. (2002) also suggested the existence of a critical aperture width, that when too small, the lava flow would simply flow over the fracture, instead of flowing into it. For Box Canyon, this critical aperture was recorded to be 0.03 to 0.15 m as inferred from size measurements of 28 fractures. At

our three locations, where infill and the aperture of the fracture that was filled is measurable, apertures of 0.16, 0.40, and 0.66 m are all above the critical aperture proposed by Welhan et al. (2002). Fractures we observe are near-vertical and did not display a noticeable decrease in aperture with exposed depth to impede inflow. Such critical aperture would also be tied to the viscosity of the basalt, likely allowing for a smaller aperture for more less viscous lava flows and vice versa.

Topography and dike dimensions

Dikes have long been tied to the volcanic features we observe in the ESRP, especially in the Great Rift. Due to lack of exposures in this region, geologists can only rely on structural patterns, topography, and models to hypothesize locations and test for dike dimensions. Previously measured rift zone widths, defined as the distance between the fracture sets, have provided estimates on the depth to dike tops (Kuntz et al., 2002; Holmes, 2005), whereas buoyancy equilibrium modeling was used to interpret depth to dike bottom and driving pressures for the dike, and boundary element modeling was used to constrain dike widths beneath KB rift (Holmes et al., 2008). Mastin and Pollard (1988) previously used numerical as well as physical modeling to predict dike widths related to surface extension, based on which a 2 m to 21m maximum dike aperture underneath the Great Rift was proposed (Holmes et al., 2008).

Our investigation of the long-wavelength topography has revealed several systematic patterns across the KB rift. We observe topographic trends with topographic highs in the east and lows in the west. The slopes are most noticeable in the data covering the northern and southern extent of the KB rift (Fig. 4.2). These are interpreted as regional trends that are caused by nearby volcanic structures such as Mosby and Horse

Butte, volcanic shields, to the northeast and the remnants of Grandview Crater in the south. Another pattern we identified across the region is a presence of broad rises centered at the fissure and unrelated to the lava flow. The rises shows a clear increase in breadth towards the center of the rift, located in the KB pit area (Fig. 4.6C). We interpret the increase in breadth to the shape of the underlying dike, where the broadest rise formed at the location where the dike is widest and tapering in rise breadth and associated dike width to the north and south. Such geometry, where the aperture is widest at the center of the structure tapering toward the tips, is typical for dikes and other opening-mode fractures (Mastin and Pollard, 1988; Vermilye and Scholz, 1995; Fossen, 2009).

We compared the rises with proposed dike dimension using the Pollard modeling methodology (Pollard et al., 1983). Our simulated ground displacements for the dike dimensions proposed by Holmes et al. (2008), do show first-order trends that match the shape for the northern and central swaths over KB rift (Fig. 4.6A–C), but do not produce a pronounced rise. In contrast, we are able to match the long-wavelength trend of the topography and pronounced nature of the rise, but they require unusual dike geometries. Our modeled dikes, a tabular dike (1) with 25 m width, at shallow depth of 10 m, and a tapered dike (2) with 2 m width at a depth of 10 m depth (Table 4.3), are not realistic. Our modeling approach is not entirely suited for KB, problems may arise from the purely elastic nature of the ground displacement modeled in elastic halfspace, when in reality we observe plastic deformation. Additionally, we assumed heterogeneous material properties, which are likely not present at KB. Accepting these shortcomings and only following general trends in the models, they may nevertheless be useful for understanding the intrusion geometry and history of the KB rift.

Previously it was suggested that either the whole dike breached the surface (Kuntz et al., 2002) or that the dike top stalled at some depth and that subsequent fissure eruptions were caused by narrower feeder dikes. Based on our findings, we support the former scenario favoring a wide dike near the surface, producing the topographic expression we detect in our DEMs at the KB rift. Our modeling also requires a shallow depth to dike bottom to produce the observed topographic rise, which is vastly different from the proposed deep-seated dike dimensions of previous studies. It may be that a narrow feeder dike is present beneath the wide portion of our proposed dike that did not produce much ground displacement and thus not noticeably partake in the formation of the observed topography. This scenario is in agreement with a series of studies in the Craters of the Moon portion of the National Monument and other nearby regions (Kuntz, 1992; Kuntz et al., 2002; Holmes et al., 2008), suggesting that there is likely a more complex plumbing system than individual dikes propagating to the surface. Further research along the non-eruptive New Butte and Minidoka fracture set using UAVs to collect long-wavelength may reveal more information on complex intrusive bodies underneath the Great Rift and highlight differences that set the eruptive KB rift apart from those that did not erupt.

Additionally, the COULOMB methodology can and has been applied topography above planetary dikes. Research conducted by Klimczak (2014) has already compared observed graben topography with ground displacement simulations produced using COULOMB and has yielded results that show dikes to cause formation of graben. This methodology is applicable to other planetary bodies to model dike intrusion along graben or rift systems but also indicates that more complex systems may be present here as well.

Other complexities that may arise on planetary bodies are: the nature of the surface impacted by craters, which reveals a much more fractured lithosphere and different effects of gravitational acceleration. What our research reveals is that topographic rises and rift systems are tied to shallow and wide dikes, which needs to be considered in further planetary research.

An adapted timeline of events at King's Bowl rift

With all the observations collected in this study and its subsequent interpretation, we add further details and update the sequence of events at the KB rift (Hughes et al., 2018; (Fig. 4.7). The intrusion begins to cause uplift across the region to form a broad rise (Fig. 4.7A). As uplift continued and the intrusion approached a critical, shallow depth, it triggered the formation of the parallel sets of fractures (Pollard et al., 1983; Rubin and Pollard, 1988; Kuntz et al., 2002) (Fig. 4.7B). The wide dike stalls at shallow depths, similarly as proposed by Kuntz et al. (2002). The uplift ultimately lead to the formation of the up to 10-m-high and 1.5 to 3-km-broad rise, with the fractures being located near the inflection point of topography. Once a narrow feeder dike presented a conduit from the shallow and wide dike to the surface, the eruption events began at the central fissure opening.

We concur with the eruption history proposed by (Hughes et al., 2018), in that lava flow filled local depressions and that two or more stages of flow formed a large lava lake, which was highly elevated and deflated over time. Even though the region was elevated as dike intrusion began and should have led to topography not conducive to pooling of lava, remnant topographic lows may have been preserved as uplift began. A shallow and wide dike causes uplifted of a larger region, possibly preserving topography

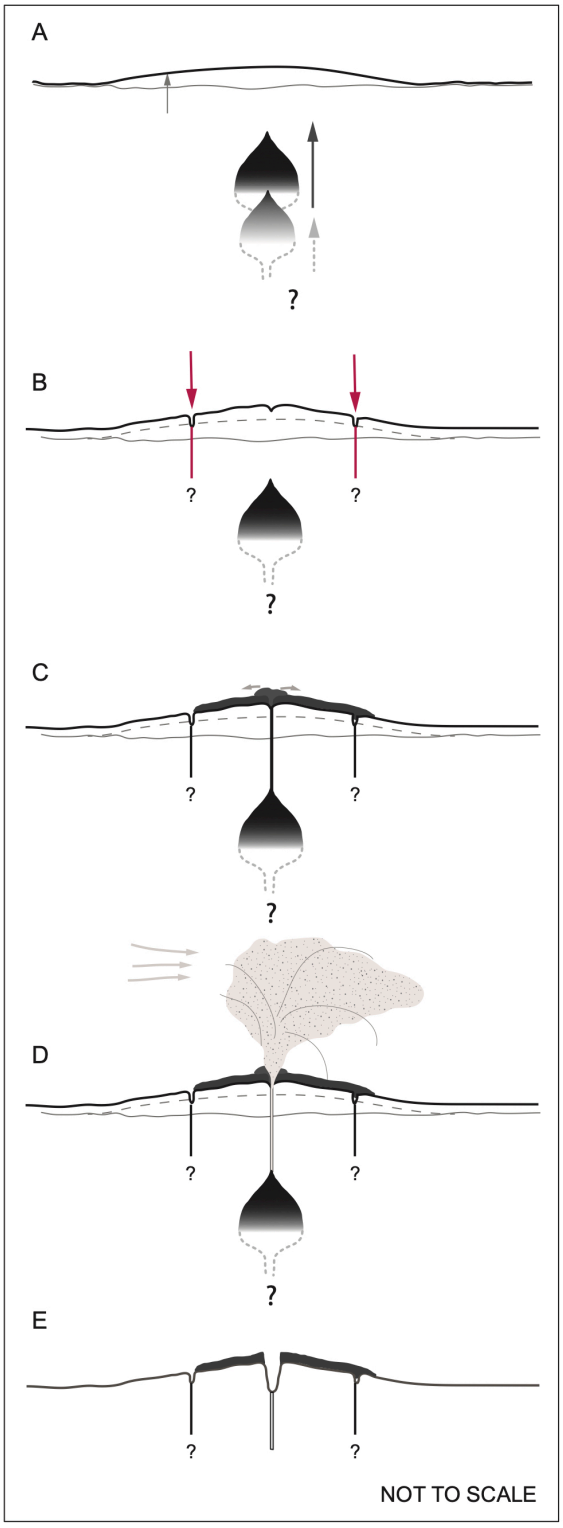

Figure 4.7 Conceptual model of the formation and evolution of the KB rift. Adapted from figures by Kuntz et al. (2002) and Hughes et al. (2018).

on very local scales. As lava spread across the surface, it began to infill in fractures and move across the fracture zones (Fig. 4.7C), occasionally leaving behind a record of surface flow deformation.

The presence of lava outflow lobes caused by pressurized lava breaking through levees is supported by our understanding of how lava was supplied in tubes into fractures and across fractures in the southeastern section of KB Rift near South Grotto (Fig. 4.5C). As magma supply waned, it was proposed by Hughes et al. (2008) that the central fissure walls collapsed, creating accommodation space for water influx at the water table of 245 m (King, 1977). This water influx lead to violent phreatomagmatic explosions that not only deposited ash predominantly to east of the fissure at KB pit and at a northern location (near our North KB site) but also ejecta blocks within a 200 m radius around the KB pit. The collapse of the fissure and phreatomagmatic explosions left behind the wide and open pit as we see it today.

Conclusions

The formation of the KB rift and its related eruptive fissures and fractures have long been tied to a dike breaching the surface. Our study reveals previously undocumented evidence on interaction between fractures and eruption at KB rift, including inflow of lava into fractures, linear lava surface deformation, and fracture lava squeeze-up, ultimately supporting the formation of fractures before fissure fed eruption. These results allowed us to place fracture formation ahead of the previously detailed description of eruption history at KB rift (Hughes et. al., 2018) and thus contributing more details to the evolution history at KB rift.

Our study has also investigated long-wavelength topography and how the observed topography at KB rift relates to a dike. Collection and subsequent analysis of high-resolution UAV topography revealed a broad rise across the central part of the KB rift near the KB pit that becomes less pronounced toward the northern and southern extent of the rift. We then compared this topography to ground displacements produced by the opening of a dike simulated with the COULOMB code. Previously proposed dike dimensions do not produce the observed topography. Models matching the observed topography better than those of dikes with inferred dimensions by the previous studies require unexpected and unusual dike geometries, largely suggesting a more complex plumbing system than previously thought. An in-depth investigation of the other, non-eruptive rift segments of the area may provide additional detail on the processes that lead to eruption at this particular rift segment.

We show that long-wavelength topographic expressions of a dike can be detected from data collected by UAVs that then can be used to help inform us about the subsurface geometry of the intrusion. This methodology can not only be applied to other rift or intrusive systems but also lends additional support that topographic rises associated with graben on other terrestrial bodies may be a result of dikes at depth (e.g., Klimczak, 2014). Therefore, the KB rift is an ideal analogue field site for understanding dike-related topography but also lava-fracture interactions at lunar graben and those in other planetary systems.

Acknowledgements

We thank Todd Stefanic for his aid in obtaining permission to fly our UAV across King's Bowl at Craters of the Moon National Monument and Preserve, as well as Holly

Crawford for providing permission to do the same at the surrounding Bureau of Land Management lands. We also thank Corbin Kling for helpful discussions about King's Bowl and UAV practices. M.B.C. was supported by the Watts Wheeler Award and the Geological Society of America Graduate Research Grant.

CHAPTER 5

CONCLUSIONS

Brittle deformation on planetary surfaces reveals an abundant amount of information on prevalent conditions in the lithosphere. In particular, the record of fractures, faults, and grabens in extensional tectonic settings can provide clues on fault growth patterns, material rock strength, and fault gouge conditions, as well as loading conditions and stresses occurring in the lithosphere and their likely causes. In this dissertation, I focused on the geomorphological and topographic character of brittle structures in extensional tectonic environments and used the collected observations to provide context on fault growth and how they relate to dike emplacement.

Lunar Investigations

The lack of weathering and erosion on the Moon has preserved a rich record of brittle deformation in the form of grabens on the Moon. Grabens and their bounding faults occur concentric and radially around the maria and are found across different terrain types, such as mare, highlands, or on the floors of large impact basin and craters. Grabens have been interpreted to have formed during extension likely linked to the formation and cooling of lunar maria (Lucchitta and Watkins, 1978; Watters and Johnson, 2010; Klimczak, 2014), but have also been attributed to the intrusion of dikes (Head and Wilson, 1993; Wilson et al., 2011; Klimczak, 2014; Wilson and Head, 2018) or loading related to mascon structures (McGovern and Litherland, 2011; Melosh et al., 2013; Thomas et al., 2015; Michaut et al., 2019). Their preserved characteristics inform

how faults grew, what stresses caused them, and how host rock surrounding the fault plane evolved.

Chapters 2 and 3 address the evolution of faults and what effect this fault growth had on host rock, with implications to formation mechanisms. Results of chapter 2 show that amongst 14 investigated grabens displacement scales disproportionally with length. Slip distribution analysis highlights that fault growth on the Moon primarily occurs via fault linkage. Chapter 2 also revealed that mare-concentric grabens may originate from the cooling of the lunar maria. Using PYFM modeling, chapter 3 demonstrates that stress and strength properties exhibit a relationship with fault length. We show that short faults require a higher remote stress to propagate and reveal that rock properties and loading conditions evolve in two ways. Along the master faults of 9 grabens, loading conditions and rock properties remain constant, regardless of individual fault length. In 5 graben systems they are found to decrease for individual faults with longer fault lengths. We propose that these findings are caused by differences in fault gouge formation. Together these chapters provide a comprehensive account of long lunar fault growth and what happens to the rock properties surrounding the fault as they evolve.

A Terrestrial Analogue

Field investigations at planetary analogue sites on Earth are vital for understanding processes on other bodies in our Solar System. One of the best analogue sites to study extensional structures is at King's Bowl, in Craters of the Moon National Monument and Preserve. Not only is this site beautifully preserved due to its young age and arid climate, but it also was hypothesized that the fractures, fissures, and lava flow were caused by emplacement of a dike. This site allowed me to physically test how dike

intrusion affects the topography and address timing relationships between fracture formation, dike emplacement, and lava flow eruption.

In chapter 4, newly collected field measurements constrain fracture formation to occur during or subsequent to dike intrusion yet predating the eruption of lava from the central fissure. Multiple types of evidence were collected and described across the basaltic rift in evidence of this relationship. Orthographic images collected by Unpiloted Aerial Vehicles were used to produce high resolution image mosaics and Digital Elevation Models that reveal that a rise across the region which is indeed supportive of dike emplacement. Further numerical modeling revealed that previously suggested dike dimensions do not produce the topography observed in the region today, indicative that the subsurface geometry of present intrusive structures may be more complex than previously assumed.

Future work

This dissertation research exemplifies how much information complex fracture systems reveal about planetary tectonics, including the distribution, kinematics and deformation in the lithosphere, and lithospheric strength properties. Continued study of such processes will shed light on planetary evolution, and what role brittle deformation mechanisms play in this complex system. Studies of this magnitude may have implications for understanding early processes on Earth, for which the record has been erased.

To further understand fault growth and processes causing the formation of these complex structures I would apply the same methodology for slip distributions and fault growth models on other planetary bodies, investigating complex fracture systems and

normal faults on other planets like Mars may reveal information if the same fault growth scenarios occur there. A recent study has revealed that normal fault dip angles may be lower for Martian faults than previously thought (Vaz et al., 2014), and investigating what role this may play on normal fault evolution may relate to other planets as well. Equally as intriguing would be further investigation of an extensional rift system on Venus such as to Devana Chasma (Swafford and Kiefer, 2004; Kiefer and Swafford, 2006), which may also shed light on how subsurface magmatism relates to the formation of complex structures. It is also vital to follow up to these studies with further field investigations on Earth, where normal faulting is exposed on the surface. A location like Hawaii would also a be good planetary analogue to further study extension as related to dike emplacement.

Throughout the research conducted for this dissertation, it has become clear that rift systems such as graben on the Moon or the Great Rift in Idaho are caused by a multitude of complex factors. On the Moon, multiple driving mechanisms have been suggested for graben formation (Lucchitta and Watkins, 1978; Head and Wilson, 1993; Watters and Johnson, 2010; Wilson et al., 2011; Melosh et al., 2013; Klimczak, 2014), and studies on multiple planets have already tied dike emplacement to graben formation (Rubin and Pollard, 1988; Rubin, 1992; Head and Wilson, 1993; Ernst et al., 2001; Schultz et al., 2004b; Head et al., 2009; Klimczak, 2014; Hardy, 2016), but questions remain. One of the biggest questions is if all long lunar grabens evolved as one population, with one major underlying cause, or as multiple populations that were caused by different mechanisms. This may be addressed by further investigating individual, but related questions. It is unclear if all grabens are tied too cooling of units within the large

lunar basins, which may be addressed by further studying the cooling of the lunar mare. Additionally, local conditions caused by impact cratering and related processes (e.g. Byrne et al., 2016) as well as loading of the lithosphere may be linked in some form to graben formation. Investigations that examine the topographic response to impact cratering or lithospheric loading may shed light on these questions. At this point it is also unclear if all grabens on the Moon are underlain by dikes. There is uncertainty what the parameters are that may influence the intrusion, and if a threshold exists under which graben formation will not occur. If grabens are underlain by dikes, it remains unclear why have we not discovered any locations where magma conduits reached the surface like on Earth. By further investigating the structures we observe, and also expanding this research to strain the mare units must have experienced during their cooling (Head and Wilson, 1992; Grove and Krawczynski, 2009) and comparing it to the strain expressed by the graben, may reveal further information on the very early days of graben formation on the Moon.

Furthermore, this dissertation showed that a relationship between fault length, loading conditions and rock properties exist. Using PYFM modeling I explain how lunar faults evolve in two ways, related to frictional rock strength and fault gouge development. Overall, rock friction and fault strength are undeniably linked, and their relationship of other fault characteristics needs further investigation. Some studies use experimental analyses on friction during high velocity slip and constant loading, frictional behavior in mixed mode faults, amongst many others (Collettini et al., 2011; Liao et al., 2014; Niemeijer and Collettini, 2014). Others consider the evolution of a natural fault system based on different parameters (Ikari et al., 2011b; Tesei et al., 2015;

Zhang et al., 2019). This subject has also been highly debated in the petroleum industry, in order to understand the role of carbon sequestration on frictional strength and slip behavior dependent on slip velocity (Samuelson and Spiers, 2012; Urpi et al., 2016). All of these studies focus on different roles between faults and rock mechanical changes that the host rock undergoes as fault accumulate slip.

I believe one of the most important questions that arises out of the relationship between friction and fault strength based on theory and laboratory results is how these findings carry over into the natural fault regime. In chapter 3, I discuss implications from lab results that revealed that frictional velocity and stability strongly influence fault strength (Ikari et al., 2011a, 2011b) for lunar graben evolution. Not only does friction affect fault strength, but also structural diagenesis, fault width, and internal structure play a role. Another question that can be added is how the relationship between thick fault cores and fault age evolve (Kim et al., 2004; O'Hara et al., 2017; Peacock et al., 2017a; Ritter et al., 2018; Delogkos et al., 2020). Based on previous studies and the assumption of a linear displacement-thickness relationship, it is implied that as faults propagate and mature, they would be expected to weaken over time. This has not yet been demonstrated valid and needs to be further investigated in Earth analogue studies, investigating changes in fault damage zones across larger normal fault complexes.

The relationship between frictional strength of a fault and physical fault state are being investigated on fault surfaces across the world. One of the best regions to study this is the Alpine fault in New Zealand, an 850 km-long transform fault with abundant surface exposures. Ongoing research considering the effect of fault gouges and fault behavior and factors influencing them are ongoing (Boulton et al., 2012, 2017, 2018; Ikari et al., 2014;

Upton et al., 2017; Chen et al., 2019; Valdez et al., 2019). Some show preferential fault slip along surfaces with water-saturated, smectite-bearing fault gouges with steady state friction coefficients (Boulton et al., 2012, 2017; Chen et al., 2019), others discuss the temperature control on frictional fault behavior (Valdez et al., 2019) , or fault architecture and strain partitioning (Upton et al., 2017). Such studies are numerous but highlight that we still have much to learn about the frictional behavior of faults in natural in situ rocks. A topic that is also debated is the subject of fault strength being more rate dependent than can be observed in laboratory frictional experiments, suggesting that fault healing, which is the recovery of frictional strength, mechanisms may play a role.

The relationship between friction and lithospheric strength affects the mechanics of fault growth and propagation and manifests itself in the character of the fault rock itself. Friction next to discontinuities and stress field orientation is one of the biggest influential factors on fault growth and fault anatomy. Answering these outstanding questions will not only shed light on fault dynamics, but also reveal underlying driving mechanisms of planetary tectonics and evolution on other rocky or icy planetary bodies in our Solar System.

REFERENCES

Allken, V., Huismans, R.S., and Fossen, H., 2013, 3D numerical modelling of graben interaction and linkage: a case study of the Canyonlands grabens, Utah: Basin Research, v. 25, p. 436–449, doi:10.1111/bre.12010.

Boulton, C., Barth, N.C., Moore, D.E., Lockner, D.A., Townend, J., and Faulkner, D.R., 2018, Frictional properties and 3-D stress analysis of the southern Alpine Fault, New Zealand: Journal of Structural Geology, v. 114, p. 43–54, doi:10.1016/j.jsg.2018.06.003.

Boulton, C., Carpenter, B.M., Toy, V., and Marone, C., 2012, Physical properties of surface outcrop cataclastic fault rocks, Alpine Fault, New Zealand: Geochemistry, Geophysics, Geosystems, v. 13, doi:10.1029/2011gc003872.

Boulton, C., Yao, L., Faulkner, D.R., Townend, J., Toy, V.G., Sutherland, R., Ma, S., and Shimamoto, T., 2017, High-velocity frictional properties of Alpine Fault rocks: Mechanical data, microstructural analysis, and implications for rupture propagation: Journal of Structural Geology, v. 97, p. 71–92, doi:10.1016/j.jsg.2017.02.003.

Bürgmann, R., Pollard, D.D., and Martel, S.J., 1994, Slip distributions on faults: effects of stress gradients, inelastic deformation, heterogeneous host-rock stiffness, and fault interaction: Journal of Structural Geology, v. 16, p. 1675–1690, doi:10.1016/0191-8141(94)90134-1.

Caine, J.S., Evans, J.P., and Forster, C.B., 1996, Fault zone architecture and permeability structure: Geology, v. 24, p. 1025, doi:10.1130/0091 7613(1996)024<1025:fzaaps> 2.3.co;2.

Callihan, M.B., and Klimczak, C., 2019, Topographic expressions of lunar graben: Lithosphere, v. 11, p. 294–305, doi:10.1130/l1025.1.

Cartwright, J.A., and Mansfield, C.S., 1998, Lateral displacement variation and lateral tip geometry of normal faults in the Canyonlands National Park, Utah: Journal of Structural Geology, v. 20, p. 3–19, doi:10.1016/s0191-8141(97)00079-5.

Cartwright, J.A., Trudgill, B.D., and Mansfield, C.S., 1995, Fault growth by segment linkage: an explanation for scatter in maximum displacement and trace length data from the Canyonlands Grabens of SE Utah: Journal of Structural Geology, v. 17, p. 1319–1326, doi:10.1016/0191-8141(95)00033-a.

Chen, X., Morgan, C.B., Carpenter, B.M., and Reches, Z., 2019, Weakening Mechanisms of Alpine Fault Gouge in High-Velocity Shear Experiments: Journal of Geophysical Research: Solid Earth, v. 124, p. 7413–7428, doi:10.1029/2019jb017383.

Clark, R.M., and Cox, S., 1996, A modern regression approach to determining fault displacement-length scaling relationships: Journal of Structural Geology, v. 18, p. 147–152, doi:10.1016/s0191-8141(96)80040-x.

Collettini, C., Niemeijer, A., Viti, C., Smith, S.A.F., and Marone, C., 2011, Fault structure, frictional properties and mixed-mode fault slip behavior: Earth and Planetary Science Letters, v. 311, p. 316–327, doi:10.1016/j.epsl.2011.09.020.

Cowie, P.A., and Scholz, C.H., 1992, Physical Explanation for the Displacement Length Relationship of Faults Using a Post-Yield Fracture-Mechanics Model: Journal of Structural Geology, v. 14, p. 1133–1148, doi:10.1016/0191-8141(92)90065-5.

Dawers, N.H., and Anders, M.H., 1995, Displacement-length scaling and fault linkage: Journal of Structural Geology, v. 17, p. 607–614, doi:10.1016/0191-8141(94)00091-d.

Delogkos, E., Manzocchi, T., Childs, C., Camanni, G., and Roche, V., 2020, The 3D structure of a normal fault from multiple outcrop observations: Journal of Structural Geology, p. 104009, doi:10.1016/j.jsg.2020.104009.

Ernst, R., Grosfils, E., and Mège, D., 2001, Giant Dike Swarms: Earth, Venus, and Mars: Annual Review of Earth and Planetary Sciences, v. 29, p. 489–534, doi:10.1146/annurev.earth.29.1.489.

Finch, E., and Gawthorpe, R., 2017, Growth and interaction of normal faults and fault network evolution in rifts: insights from three-dimensional discrete element modelling: Geological Society, London, Special Publications, v. 439, p. 219–248, doi:10.1144/sp439.23.

Fossen, H., 2009, Faults, *in* Structural Geology, Cambridge University Press: p. 151–188, doi:10.1017/cbo9780511777806.010.

Fossen, H., and Rotevatn, A., 2016, Fault linkage and relay structures in extensional settings—A review: Earth-Science Reviews, v. 154, p. 14–28, doi:10.1016/j.earscirev.2015.11.014.

Fossen, H., Schultz, R.A., and Rundhovde, E., 2010, Fault linkage and graben stepovers in the Canyonlands (Utah) and the North Sea Viking Graben, with implications

for hydrocarbon migration and accumulation: AAPG bulletin, v. 94, p. 597–613, doi:10.1306/10130909088.

French, R.A., Bina, C.R., Robinson, M.S., and Watters, T.R., 2015, Small-scale lunar graben: Distribution, dimensions, and formation processes: Icarus, v. 252, p. 95–106, doi:10.1016/j.icarus.2014.12.031.

Garry, B.W., Hughes, S.S., Nawotniak, S.E.K., Neish, C.D., Haberle, C.W., Heldmann, J.L., Darlene, and Lim, S.S., 2014, The Geology of Inferno Chasm, Idaho: A Terrestrial analog for lunar rilles?, *in* v. 3047,

Golombek, M.P., 1979, Structural analysis of lunar grabens and the shallow crustal structure of the Moon: Journal of Geophysical Research: Solid Earth, v. 84, p. 4657–4666, doi:10.1029/jb084ib09p04657.

Golombek, M.P., and McGill, G.E., 1983, Grabens, basin tectonics, and the maximum total expansion of the Moon: Journal of Geophysical Research: Solid Earth, v. 88, p. 3563–3578, doi:10.1029/jb088ib04p03563.

Greeley, R., 1982, The Snake River Plain, Idaho: Representative of a New Type of Volcanism: Journal of Geophysical Research, v. 87, p. 2705–2712.

Greeley, R., and Schultz, P.H., 1977, Possible Planetary Analogs to Snake River Plain basalt features, *in* v. CR-154621, p. 233–251.

Grove, T.L., and Krawczynski, M.J., 2009, Lunar Mare Volcanism: Where Did the Magmas Come From? Elements, v. 5, p. 29–34, doi:10.2113/gselements.5.1.29.

Gudmundsson, A., Guidi, G.D., and Scudero, S., 2013, Length–displacement scaling and fault growth: Tectonophysics, v. 608, p. 1298–1309, doi:10.1016/j.tecto.2013.06.012.

Gupta, A., and Scholz, C.H., 2000, A model of normal fault interaction based on observations and theory: Journal of Structural Geology, v. 22, p. 865–879, doi:10.1016/s0191-8141(00)00011-0.

Hardy, S., 2016, Does shallow dike intrusion and widening remain a possible mechanism for graben formation on Mars? Geology, doi:10.1130/g37285.1.

Head, J.W. et al., 2009, Evidence for intrusive activity on Mercury from the first MESSENGER flyby: Earth and Planetary Science Letters, v. 285, p. 251–262, doi:10.1016/j.epsl.2009.03.008.

Head, J.W., and Wilson, L., 1993, Lunar Graben Formation Due to Near-Surface Deformation Accompanying Dike Emplacement: Planetary and Space Science, v. 41, p. 719–727, doi:10.1016/0032-0633(93)90114-h.

Head, J.W., and Wilson, L., 1992, Lunar mare volcanism: Stratigraphy, eruption conditions, and the evolution of secondary crusts: Geochimica et Cosmochimica Acta, v. 56, p. 2155–2175, doi:10.1016/0016-7037(92)90183-j.

Hiesinger, H., and Head, J.W., 2006, New Views of Lunar Geoscience: An Introduction and Overview: Reviews in Mineralogy and Geochemistry, v. 60, p. 1–81, doi:10.2138/rmg.2006.60.1.

Holmes, A.A.J., 2005, Extension along the great rift as revealed by field measurements of surface deformation features. Master's Thesis, Idaho State University, p.135.

Holmes, A.A.J., Rodgers, D.W., and Hughes, S.S., 2008, Kinematic analysis of fractures in the Great Rift, Idaho: Implications for subsurface dike geometry, crustal extension, and magma dynamics: Journal of Geophysical Research, v. 113, p. 15379–15, doi:10.1029/2006jb004782.

Hughes, S.S., Nawotniak, S.E.K., Borg, C., Mallonee, H.C., Purcell, S., Neish, C., Garry, W.B., Haberle, C.W., Lim, D.S.S., and Heldman, J.H., 2016, Diverse eruptions at ~2,200 years B.P. on the Great Rift, Idaho: Inferences for mgama dynamics along volcanic rift zones. , *in* v. 2841, doi:47th Lunar and Planetary Science Conference (2016).

Hughes, S.S., Nawotniak, S.E.K., Sears, D.W.G., Borg, C., Garry, W.B., Christiansen, E.H., Haberle, C.W., Lim, D.S.S., and Heldmann, J.L., 2018, Phreatic explosions during basaltic fissure eruptions: Kings Bowl lava field, Snake River Plain, USA: Journal of Volcanology and Geothermal Research, v. 351, p. 89–104, doi:10.1016/j.jvolgeores.2018.01.001.

Hughes, S.S., Smith, R.P., Hackett, W.R., and Anderson, S.R., 1999, Mafic Volcanism and Environmental Geology of the Eastern Snake River Plain, Idaho, *in* v. 1, p. 143–167.

Ikari, M.J., Carpenter, B.M., Kopf, A.J., and Marone, C., 2014, Frictional strength, rate-dependence, and healing in DFDP-1 borehole samples from the Alpine Fault, New Zealand: Tectonophysics, v. 630, p. 1–8, doi:10.1016/j.tecto.2014.05.005.

Ikari, M.J., Marone, C., and Saffer, D.M., 2011a, On the relation between fault strength and frictional stability: Geology, v. 39, p. 83–86, doi:10.1130/g31416.1.

Ikari, M.J., Niemeijer, A.R., and Marone, C., 2011b, The role of fault zone fabric and lithification state on frictional strength, constitutive behavior, and deformation microstructure: Journal of Geophysical Research, v. 116, p. 423–25, doi:10.1029/2011jb008264.

Jaumann, R. et al., 2012, Geology, geochemistry, and geophysics of the Moon Status of current understanding: Planetary and Space Science, v. 74, p. 15–41, doi:10.1016/j.pss.2012.08.019.

Jozwiak, L.M., Head, J.W., and Wilson, L., 2015, Lunar floor-fractured craters as magmatic intrusions: Geometry, modes of emplacement, associated tectonic and volcanic features, and implications for gravity anomalies: Icarus, v. 248, p. 424–447, doi:10.1016/j.icarus.2014.10.052.

Jozwiak, L.M., Head, J.W., Zuber, M.T., Smith, D.E., and Neumann, G.A., 2012, Lunar floor-fractured craters: Classification, distribution, origin and implications for magmatism and shallow crustal structure: Journal of Geophysical Research: Planets, v. 117, p. 1–23, doi:10.1029/2012je004134.

Kiefer, W.S., and Swafford, L.C., 2006, Topographic analysis of Devana Chasma, Venus: implications for rift system segmentation and propagation: Journal of Structural Geology, v. 28, p. 2144–2155, doi:10.1016/j.jsg.2005.12.002.

Kim, Y.-S., Peacock, D.C.P., and Sanderson, D.J., 2004, Fault damage zones: Journal of Structural Geology, v. 26, p. 503–517, doi:10.1016/j.jsg.2003.08.002.

King, J.S., 1977, Crystal Ice Cave and Kings Bowl Crater, eastern Snake River Plain, Idaho: Nasa Contract , v. CR-154621, p. 153–163.

King, J.S., 1982, Selected volcanic features of the south-central Snake River Plain, Idaho. : Cenozoic Geology of Idaho: Idaho Geological Survey Bulletin, v. 26, p. 439–451.

Klimczak, C., 2014, Geomorphology of lunar grabens requires igneous dikes at depth: Geology, v. 42, p. 963–966, doi:10.1130/g35984.1.

Klimczak, C., 2015, Limits on the brittle strength of planetary lithospheres undergoing global contraction: Journal of Geophysical Research: Planets, v. 120, p. 2135–2151, doi:10.1002/2015je004851.

Klimczak, C., Callihan, M., Crane, K.T., Kling, C.L., and Byrne, P.K., 2018, Fault Rock Evolution of Large Thrust Systems on Mars, *in* Lunar and Planetary Science Conference, v. 1083, p. 1–2.

Krantz, R.W., 1988, Multiple fault sets and three-dimensional strain: theory and application: Journal of Structural Geology, v. 10, p. 225–237, doi:10.1016/0191-8141(88)90056-9.

Kuntz, M.A., 1992, A model-based perspective of basaltic volcanism, eastern Snake River Plain, Idaho, *in* Regional Geology of Eastern Idaho and Western Wyoming, v. 179, p. 289–304, doi:10.1130/mem179-p289.

Kuntz, M.A., 1989, Geology of the craters of the Moon Lava Field, Idaho: American Geophysical Union (AGU), v. 60, doi:10.1029/ft305p0051.

Kuntz, M.A., Anderson, S.R., Champion, D.E., Lanphere, M.A., and Grunwald, D.J., 2002, Tension cracks, eruptive fissures, dikes, and faults related to late Pleistocene-Holocene basaltic volcanism and implications for the distribution of hydraulic conductivity in the eastern Snake River Plain, Idaho: Special Paper 353: Geology, hydrogeology, and environmental remediation: Idaho National Engineering and Environmental Laboratory, eastern Snake River plain, Idaho, v. 353, doi:10.1130/0-8137-2353-1.111.

Kuntz, M.A., Champion, D.E., Spiker, E.C., and Lefebvre, R.H., 1986, Contrasting Magma Types and Steady-State, Volume-Predictable, Basaltic Volcanism Along

the Great Rift, Idaho: Geological Society of America Bulletin, v. 97, p. 579–594, doi:10.1130/0016-7606(1986)97<579:cmtasv>2.0.co;2.

Kuntz, M.A., Skipp1, B., Champion, D.E., Gans, P.B., Sistine, D.P.V., and Snyders, and S.R., 2007, Geologic Map of Craters of the Moon 30’ x60’ Quadrangle, Idaho:

Long, J.J., and Imber, J., 2011, Geological controls on fault relay zone scaling: Journal of Structural Geology, v. 33, p. 1790–1800, doi:10.1016/j.jsg.2011.09.011.

Lucchitta, B.K., and Watkins, J.A., 1978, Age of graben systems on the moon, *in* Pro. Lunar Planet. Sci. Conf., Geochim. Cosmochim. Acta, p. 3459–3472.

Manighetti, I., King, G.C.P., and Gaudemer, Y., 2007, Slip accumulation and lateral propagation of active normal faults in Afar: , p. 1–30.

Mansfield, C., and Cartwright, J., 2001, Fault growth by linkage: observations and implications from analogue models: Journal of Structural Geology, v. 23, p. 745–763, doi:10.1016/s0191-8141(00)00134-6.

Martel, S.J., and Langley, J.S., 2006, Propagation of normal faults to the surface in basalt, Koae fault system, Hawaii: Journal of Structural Geology, v. 28, p. 2123–2143, doi:10.1016/j.jsg.2005.12.004.

Mastin, L.G., and Pollard, D.D., 1988, Surface Deformation and Shallow Dike Intrusion Processes at Inyo Craters, Long Valley, California: Journal of Geophysical Research: Solid Earth, v. 93, p. 13221–13235, doi:10.1029/jb093ib11p13221.

Melosh, H.J. et al., 2013, The Origin of Lunar Mascon Basins: Science, v. 340, p. 1549–1552, doi:10.1126/science.1235768.

Melosh, H.J., and Williams, C.A., 1989, Mechanics of graben formation in crustal rocks: A finite element analysis: Journal of Geophysical Research: Solid Earth (1978–2012), v. 94, p. 1–13, doi:10.1029/jb094ib10p13961.

Michaut, C., Thiriet, M., and Thorey, C., 2016, Insights into mare basalt thicknesses on the Moon from intrusive magmatism: Physics of the Earth and Planetary Interiors, v. 257, p. 187–192, doi:10.1016/j.pepi.2016.05.019.

Muraoka, H., and Kamata, H., 1983, Displacement distribution along minor fault traces: Journal of Structural Geology, v. 5, p. 483–495, doi:10.1016/0191-8141(83)90054-8.

Nahm, A.L., 2016, A New Map of Graben on the Lunar Nearside: Initial Observations and Classification, *in* Lunar and Planetary Science Conference, v. 47th, p. 1855.

Nahm, A.L., and Dudde, A.K., 2016, Relative ages of graben and wrinkle ridges on the nearside of the Moon reveal contradictory relationships, *in* New Views on the Moon, p. 1.

Nahm, A.L., and Schultz, R.A., 2013, Rupes Recta and the geological history of the Mare Nubium region of the Moon: insights from forward mechanical modelling of the 'Straight Wall': Geological Society, London, Special Publications, v. 401, p. 377–394, doi:10.1144/sp401.4.

Niemeijer, A.R., and Collettini, C., 2014, Frictional Properties of a Low-Angle Normal Fault Under In Situ Conditions: Thermally-Activated Velocity Weakening: Pure and Applied Geophysics, v. 171, p. 2641–2664, doi:10.1007/s00024-013-0759-6.

O'Hara, A.P., Jacobi, R.D., and Sheets, H.D., 2017, Predicting the width and average fracture frequency of damage zones using a partial least squares statistical

analysis: Implications for fault zone development: Journal of Structural Geology, v. 98, p. 38–52, doi:10.1016/j.jsg.2017.03.008.

Okada, Y., 1992, Internal Deformation due to Shear and Tensile Faults in a Half-space: Bulletin of the Seismological Society of America, v. 2, p. 1018–1040.

Opheim, J.A., and Gudmundsson, A., 1989, Formation and Geometry of Fractures, and Related Volcanism, of the Krafla Fissure Swarm, Northeast Iceland: Geological Society of America Bulletin, v. 101, p. 1608–1622, doi:10.1130/0016-7606(1989)101<1608:fagofa>2.3.co;2.

Parsons, T., Thompson, G.A., and Smith, R.P., 1998, More than one way to stretch: a tectonic model for extension along the plume track of the Yellowstone hotspot and adjacent Basin and Range Province: Tectonics, v. 17, p. 221–234, doi:10.1029/98tc00463.

Peacock, D., 2002, Propagation, interaction and linkage in normal fault systems: Earth-Science Reviews, v. 58, p. 121–142, doi:10.1016/s0012-8252(01)00085-x.

Peacock, D.C.P., and Sanderson, D.J., 1991, Displacements, segment linkage and relay ramps in normal fault zones: Journal of Structural Geology, v. 13, p. 721–733, doi:10.1016/0191-8141(91)90033-f.

Polit, A.T., Schultz, R.A., and Soliva, R., 2009, Geometry, displacement–length scaling, and extensional strain of normal faults on Mars with inferences on mechanical stratigraphy of the Martian crust: Journal of Structural Geology, v. 31, p. 662–673, doi:10.1016/j.jsg.2009.03.016.

Pollard, D.D., Delaney, P.T., Duffield, W.A., Endo, E.T., and Okamura, A.T., 1983, Surface deformation in volcanic rift zones: Tectonophysics, v. 94, p. 541–584, doi:10.1016/0040-1951(83)90034-3.

Ritter, M.C., Rosenau, M., and Oncken, O., 2018, Growing Faults in the Lab: Insights Into the Scale Dependence of the Fault Zone Evolution Process: Tectonics, v. 37, p. 140–153, doi:10.1002/2017tc004787.

Rodgers, D.W., Hackett, W.R., and Ore, H.T., 1990, Extension of the Yellowstone plateau, eastern Snake River Plain, and Owyhee plateau: Geology, v. 18, p. 1138, doi:10.1130/0091-7613(1990)018<1138:eotype>2.3.co;2.

Roggon, L., Hetzel, R., Hiesinger, H., Clark, J.D., Hampel, A., and Bogert, C.H. van der, 2017, Length-displacement scaling of thrust faults on the Moon and the formation of uphill-facing scarps: Icarus, v. 292, p. 112–124, doi:10.1016/j.icarus.2016.12.034.

Rotevatn, A., Jackson, C.A.-L., Tvedt, A.B.M., Bell, R.E., and Blækkan, I., 2018, How do normal faults grow? Journal of Structural Geology, doi:10.1016/j.jsg.2018.08.005.

Rubin, A.M., 1992, Dike-induced faulting and graben subsidence in volcanic rift zones: Journal of Geophysical Research: Solid Earth, v. 97, p. 1839–1858, doi:10.1029/91jb02170.

Rubin, A.M., and Pollard, D.D., 1988, Dike-induced faulting in rift zones of Iceland and Afar: Geology, v. 16, p. 413, doi:10.1130/0091-7613(1988)016<0413:difirz>2.3.co;2.

Samuelson, J., and Spiers, C.J., 2012, Fault friction and slip stability not affected by Co2 storage: Evidence from short-term laboratory experiments on North Sea reservoir sandstones and caprocks: International Journal of Greenhouse Gas Control, v. 11, p. 78–90, doi:10.1016/j.ijggc.2012.09.018.

Schultz, P.H., 1976, Floor-fractured lunar craters: The Moon, v. 15, p. 241–273, doi:10.1007/bf00562240.

Schultz, R.A., 2019, Geologic Fracture Mechanics:, doi:10.1017/9781316996737.

Schultz, R.A., and Fossen, H., 2002, Displacement-length scaling in three dimensions: the importance of aspect ratio and application to deformation bands: Journal of Structural Geology, v. 24, p. 1389–1411, doi:10.1016/s0191-8141(01)00146-8.

Schultz, R.A., and Fossen, H., 2008, Terminology for structural discontinuities: AAPG Bulletin, v. 92, p. 853–867, doi:10.1306/02200807065.

Schultz, R.A., Hauber, E., Kattenhorn, S.A., Okubo, C.H., and Watters, T.R., 2010, Interpretation and analysis of planetary structures: Journal of Structural Geology, v. 32, p. 855–875, doi:10.1016/j.jsg.2009.09.005.

Schultz, R.A., Moore, J.M., Grosfils, E.B., Tanaka, K.L., and Mege, D., 2007, The Canyonlands model for planetary grabens: Revised physical basis and implications, *in* The Geology of Mars: Evidence from Earth-Based Analogs, p. 371–399, doi:https://doi.org/10.1017/CBO9780511536014.016.

Schultz, R.A., Okubo, C.H., Goudy, C.L., and Wilkins, S.J., 2004, Igneous dikes on Mars revealed by Mars Orbiter Laser Altimeter topography: Geology, v. 32, p. 889–892, doi:10.1130/g20548.1.

Schultz, R.A., Okubo, C.H., and Wilkins, S.J., 2006, Displacement-length scaling relations for faults on the terrestrial planets: Journal of Structural Geology, v. 28, p. 2182–2193, doi:10.1016/j.jsg.2006.03.034.

Smith, D.E. et al., 2009, The Lunar Orbiter Laser Altimeter Investigation on the Lunar Reconnaissance Orbiter Mission: Space Science Reviews, v. 150, p. 209–241, doi:10.1007/s11214-009-9512-y.

Soliva, R., and Benedicto, A., 2004, A linkage criterion for segmented normal faults: Journal of Structural Geology, v. 26, p. 2251–2267, doi:10.1016/j.jsg.2004.06.008.

Soliva, R., and Benedicto, A., 2005, Geometry, scaling relations and spacing of vertically restricted normal faults: Journal of Structural Geology, v. 27, p. 317–325, doi:10.1016/j.jsg.2004.08.010.

Soliva, R., Benedicto, A., and Maerten, L., 2006, Spacing and linkage of confined normal faults: importance of mechanical thickness: Journal of Geophysical Research, v. 111, p. 1–17, doi:10.1029/2004jb003507.

Soliva, R., Schultz, R.A., Benedicto, A., and Soliva, R., 2005, Three-dimensional displacement-length scaling and maximum dimension of normal faults in layered rocks: Geophysical Research Letters, v. 32, p. 1–4, doi:10.1029/2005gl023007.

Solomon, S.C., and Head, J.W., 1979, Vertical Movement in Mare Basins - Relation to Mare Emplacement, Basin Tectonics, and Lunar Thermal History: Journal of Geophysical Research, v. 84, p. 1667–1682, doi:10.1029/jb084ib04p01667.

Stubblefield, R.K., 2019, Extensional Tectonics at Alba Mons, Mars: A Case Study for Local versus Regional Stress Fields.

Studer-Ellis, G.L., 2019, Structural and Geomorphic Mapping of Northern Claritas Fossae and the Thaumasia Graben, Mars: Implications for Formation.

Swafford, L.C., and Kiefer, W.S., 2004, Topographic and Structural Analysis of Devana Chasma, Venus: A propagating Rift System.

Tesei, T., Lacroix, B., and Collettini, C., 2015, Fault strength in thin-skinned tectonic wedges across the smectite-illite transition: Constraints from friction experiments and critical tapers: Geology, v. 43, p. 923–926, doi:10.1130/g36978.1.

Thomson, B.J., Grosfils, E.B., Bussey, D.B.J., and Spudis, P.D., 2009, A new technique for estimating the thickness of mare basalts in Imbrium Basin: Geophysical Research Letters, v. 36, p. 16319–5, doi:10.1029/2009gl037600.

Toda, S., Stein, R.S., Sevilgen, V., and Lin, J., 2011, Coulomb 3.3 Graphic-rich deformation and stress-changes oftware for earthquake, tectonic, and volcano reseach and teachin - Userguide:, 63 p.

Trudgill, B., and Cartwright, J., 1994, Relay-ramp forms and normal-fault linkages, Canyonlands National Park, Utah: Geological Society of America Bulletin, v. 106, p. 1143–1157, doi:10.1130/0016-7606.

Upton, P., Song, B.R., and Koons, P.O., 2017, Topographic control on shallow fault structure and strain partitioning near Whataroa, New Zealand demonstrates weak Alpine Fault: New Zealand Journal of Geology and Geophysics, v. 61, p. 1–8, doi:10.1080/00288306.2017.1397706.

Urpi, L., Rinaldi, A.P., Rutqvist, J., Cappa, F., and Spiers, C.J., 2016, Dynamic simulation of CO2-injection-induced fault rupture with slip-rate dependent

friction coefficient: Geomechanics for Energy and the Environment, v. 7, p. 47–65, doi:10.1016/j.gete.2016.04.003.

Valdez, R.D., Kitajima, H., and Saffer, D.M., 2019, Effects of temperature on the frictional behavior of material from the Alpine Fault Zone, New Zealand: Tectonophysics, v. 762, p. 17–27, doi:10.1016/j.tecto.2019.04.022.

Vaz, D.A., Spagnuolo, M.G., and Silvestro, S., 2014, Morphometric and geometric characterization of normal faults on Mars: Earth and Planetary Science Letters, v. 401, p. 83–94, doi:10.1016/j.epsl.2014.05.022.

Walsh, J.J., Nicol, A., and Childs, C., 2002, An alternative model for the growth of faults: Journal of Structural Geology, v. 24, p. 1669–1675, doi:10.1016/s0191-8141(01)00165-1.

Walsh, J.J., and Watterson, J., 1987, Distributions of cumulative displacement and seismic slip on a single normal fault surface: Journal of Structural Geology, v. 9, p. 1039–1046, doi:10.1016/0191-8141(87)90012-5.

Watters, T.R., and Johnson, C.L., 2010, Lunar Tectonics, *in* Planetary Tectonics, p. 121–182.

Welhan, J.A., Johannesen, C.M., Reeves, K.S., Clemo, T.M., Glover, J.A., and Bosworth, K.W., 2002, Morphology of inflated pahoehoe lava and spatial architecture of their porous and permeable zones, eastern Snake River Plain, Idaho: GSA Special Paper 353: Geology, Hydrogeology, and Envriomental Remediation: Iadho National Engineering and Environmental Laboratory, Eastern Snake River Plain, Idaho, p. 135–150, doi:0-8137-2353-1.

Wilhelms, D.E., Howard, K.A., and Wilshire, H.G., 1979, Geologic map of the south side of the Moon.:

Willemse, E.J.M., 1997, Segmented normal faults: Correspondence between three-dimensional mechanical models and field data: Journal of Geophysical Research: Solid Earth, v. 102, p. 675–692, doi:10.1029/96jb01651.

Willemse, E., Pollard, D.D., and Aydin, A., 1996, Three-dimensional analyses of slip distributions on normal fault arrays with consequences for fault scaling: Journal of Structural Geology, v. 18, p. 295–309.

Wilson, L., Hawke, B.R., Giguere, T.A., and Petrycki, E.R., 2011, An igneous origin for Rima Hyginus and Hyginus crater on the Moon: Icarus, v. 215, p. 584–595, doi:10.1016/j.icarus.2011.07.003.

Wilson, L., and Head, J.W., 2018, Lunar floor-fractured craters: Modes of dike and sill emplacement and implications of gas production and intrusion cooling on surface morphology and structure: Icarus, v. 305, p. 105–122, doi:10.1016/j.icarus.2017.12.030.

Wilson, L., and Head, J.W., 2002, Tharsis-radial graben systems as the surface manifestation of plume-related dike intrusion complexes: Models and implications: Journal of Geophysical Research, v. 107, p. 1-1-1–24, doi:10.1029/2001je001593.

Zhang, F., An, M., Zhang, L., Fang, Y., and Elsworth, D., 2019, The Role of Mineral Composition on the Frictional and Stability Properties of Powdered Reservoir Rocks: Journal of Geophysical Research: Solid Earth, v. 124, p. 1480–1497, doi:10.1029/2018jb016174.

Zoback, M.D., 2010, Basic constitutive laws, *in* Reservoir Geomechanics, Cambridge University Press, Cambridge UK,v. 1, p. 56–83.

APPENDIX A

OVERLAP AND SPACING DATA TABLE

The following table shows all individual measurements obtained for fault segments that displayed spacing and overlap. Values were extracted from open source Digital Elevation Model (MOON LRO LOLA) data and are presented in the order of overlap appearance within the graben system.

Table 1. Overlap and Spacing data from lunar graben bounding faults.

Name (N – north, S – south)	Overlap (km)	Spacing (km)
Mersenius	13.51667075	1.725334527
Hesiodus S1	2.132631565	1.19614057
Hesiodus S2	7.51383239	0.889841837
Hesiodus S3	1.690653861	0.960470101
Hesiodus S4	0.334960033	0.528918883
Hesiodus S5	0.187422394	0.338673716
Hesiodus S6	1.467674929	0.755630227
Hesiodus S7	2.419862826	0.453150729
Hesiodus S8	1.019872247	0.350347976
Hesiodus S10	0.449007704	0.14487417
Hesiodus S11	1.226829784	0.487123504
Hesiodus S12	1.16082106	0.68644764
Hesiodus S13	1.875229978	0.697622811
Hesiodus S14	3.274896055	0.720811118
Hesiodus N1	0.419267971	0.510940157
Hesiodus N2	0.664926001	0.656607224
Hesiodus N3	1.261451448	0.963374481
Flammarion and Oppolzer N1	1.842095077	0.800744525
Flammarion and Oppolzer S1	2.38396426	0.709734762
Ariadaeous	3.749623253	1.222117998

Goclenius 1 N1	3.496136975	0.648335213
Goclenius 1 N2	6.215221726	0.617109979
Goclenius 1 S1	0.557462293	0.983425717
Goclenius 1 S2	1.205853074	0.500956167
Goclenius 1 N3	6.995054641	0.666708499
Goclenius 2S1	6.969723913	0.465203283
	0	0
Cauchy N1	4.208226914	0.630128282
Cauchy N2	5.04630554	0.584232631
Cauchy N3	4.089447668	0.643495868
Cauchy N4	0.505686951	0.868490489
Cauchy N5	0.905654014	1.384762025
Cauchy N6	1.842340354	1.26591125
Cauchy N7	1.475133148	0.640483532
Cauchy S1	2.773279714	1.70535341
Cauchy S2	3.099456737	0.691530585
Cauchy S3	11.34312221	0.915541391
Cauchy S4	19.85341701	0.629368649
Cauchy S5	1.155841479	0.548915393
Daniell S1	0.992815558	0.886758678
Daniell N1	5.265567673	2.665223433
Daniell N2	0.414860635	0.824364426
Daniell N3	0.622809543	0.473963282
Daniell N4	1.316003468	0.477454317
Daniell N5	5.703176687	1.924277183
Daniell N6	4.963226309	0.430190072
Cardanus N1	15.02917095	1.883048942
Cardanus S1	4.458526304	0.953755294
Sirsalis N1	10.095716	1.263736287
Sirsalis N2	1.016837602	1.016938201
Sirsalis N3	9.624196494	0.998465162
Sirsalis N4	0.911672271	0.618799121
Sirsalis N5	9.176742921	1.016264199
Sirsalis S1	5.104460552	0.988438703
Sirsalis S2	6.106227068	0.884403243
Sirsalis S4	10.03607039	0.860228107
Sirsalis S3	29.40339612	1.47272228

Sirsalis N6	14.90200685	1.262239002
Sirsalis N7	5.727451158	0.873677947
Sirsalis N8	2.004146739	1.526055523
Sirsalis S5	26.64761213	2.864902907
Sirsalis S6	4.30220294	1.435278263
Sirsalis S7	10.66322977	0.917297547
Sirsalis N9	9.353836401	1.042342607
Sirsalis N10	4.403563283	2.908635261

APPENIX B

SUPPLEMENTAL STATISTICS FOR PYFM

The following table shows individual statistical calculations for each of the individual graben-bounding master faults investigated in chapter 3.

Table 1. Supplementary Statistics on PYFM model and observed slip distribution fit.

Num. of faults	**Fault Length (km)**	**σ_r (MPa)**	**σ_y (MPa)**	**Stand. Error of the Mean (S)**	**St. Deviation (SD)**	**Deg. of freedom**	**Median**	**Most negative deviation (m)**	**Most positive deviation (m)**	**Con-fidence Interval 5%**	**D_{max}**	**St. Dev/ D_{max}**
Ariadaeous												
1	38.34	51	168	15.62	44.19	8	-53.38	-126.10	-13.45	32.73	117.87	0.37
2	164.543			41.74	191.30	21	-97.42	-239.02	476.94	83.84	1021.91	0.19
3				44.78	214.74	23	-76.99	-252.80	619.62	89.73	797.82	0.27
ALL	304.848			**26.11**	**191.85**	**54**	**-76.99**	**-252.80**	**619.62**	**51.65**	**1021.91**	**0.19**
Cardanus 1												
1	72.554	32	123	3.73	15.38	16	7.88	-20.09	38.77	7.78	168.52	0.09
Cardanus 2												
1	80.97943	40	160	16.43	71.62	18	-46.87	-84.71	188.28	34.04	302.58	0.24
2a	55.64911			13.02	46.96	12	20.00	-42.87	116.54	27.75	245.93	0.19

2b	51.01168			19.65	68.06	11	-1.37	-70.19	129.05	42.18	237.67	0.29
3	23.7414			5.86	14.35	5	-17.20	-38.28	2.16	14.07	59.03	0.24
4	20.09243			14.34	35.13	5	0.86	-8.05	35.04	34.43	75.94	0.46
5	33.51602			10.74	30.38	7	9.17	-59.15	29.79	24.31	99.22	0.31
ALL	223.214			**7.31**	**57.98**	**62**	**-3.32**	**-84.71**	**188.28**	**14.55**	302.58	0.19
Cauchy												
1	16.046			5.56	13.63	5	-12.72	-35.49	2.59	13.35	32.57	0.42
2	38.005			8.64	25.93	8	-30.79	-57.22	31.92	19.21	93.86	0.28
3,4	42.687			6.73	25.19	13	59.34	14.12	95.03	14.25	200.21	0.13
5–8	58.907	36	140	7.84	47.05	35	-22.17	-143.31	44.56	15.81	158.71	0.30
9	50.876			7.62	22.86	8	-25.09	-67.50	11.80	16.94	107.72	0.21
10	38.699			7.79	25.84	10	-43.03	-70.53	7.08	16.88	70.80	0.36
ALL	204.856			**5.46**	**48.26**	**77**	**-21.86**	**-143.31**	**95.03**	**10.85**	**200.21**	**0.24**
Daniell												
1	32.5929			25.96	73.43	7	114.70	-38.98	164.46	58.75	272.44	0.27
2	47.2888			25.35	84.08	10	-48.50	-103.87	95.52	54.93	255.89	0.33
3	35.35747			13.90	41.71	8	-88.87	-119.14	4.03	30.90	79.09	0.53
4	35.26653			20.22	57.20	7	-24.29	-55.99	109.72	45.77	186.08	0.31
5	14.95781	58	225	6.71	15.00	4	38.73	9.60	43.55	16.97	94.89	0.16
6	7.367959			6.31	14.11	4	70.27	60.14	93.82	15.97	119.78	0.12
7	26.08159			3.86	10.20	6	6.39	-8.41	17.18	8.94	100.76	0.10
8	15.77809			2.42	5.93	5	17.91	8.99	25.43	5.81	79.16	0.07
9	21.67555			7.86	19.26	5	6.39	-14.10	37.35	18.87	90.11	0.21
10	5.903825			0.90	2.02	4	76.69	72.70	77.23	2.28	100.09	0.02

12	18.3335			25.23	66.74	6	9.88	-10.84	170.49	58.50	233.13	0.29
13	18.22438			10.92	34.54	9	86.86	37.36	132.66	23.94	177.30	0.19
14	42.17524			47.53	116.42	5	-109.55	-141.63	175.71	114.09	188.08	0.62
ALL	**264.74**			**8.38**	**79.01**	**88**	**16.30**	**-141.63**	**175.71**	**16.60**	**272.44**	**0.29**
Flammarion and Oppolzer												
1	49.229			8.46	31.66	13	-5.56	-60.29	45.05	17.91	222.28	0.14
2	62.45			28.46	113.85	15	-29.00	-177.37	159.18	59.64	313.52	0.36
3a	45.849			16.72	55.45	10	6.46	-107.50	57.08	36.23	215.36	0.26
3b	52537	45	176	15.38	55.45	12	-16.34	-95.90	21.78	32.77	156.96	0.35
3c	66.866			12.23	47.35	14	-24.03	-160.18	106.61	25.74	60.00	0.79
4	13.77			40.75	99.80	5	145.54	-23.17	241.28	97.81	275.89	0.36
ALL	**282.983**			**10.80**	**92.93**	**73**	**-6.25**	**-177.37**	**241.28**	**21.47**	**313.52**	**0.30**
Goclenius 2												
1	21.26628			7.63	27.51	12	-49.98	-82.48	3.89	16.26	60.98	0.45
2	12.27744			13.92	36.83	6	-37.67	-49.13	47.01	32.29	88.91	0.41
3	16.94451	78	257	11.29	35.71	9	-1.91	-23.67	81.97	24.75	127.55	0.28
4	9.413617			7.23	17.70	5	2.61	-12.42	29.41	17.35	65.73	0.27
ALL	**42.985**			**6.90**	**41.38**	**35**	**-15.66**	**-82.48**	**81.97**	**13.91**	**127.55**	0.32
Gerard												
1	22.976			14.02	37.09	6	-29.35	-79.56	14.13	32.51	88.36	0.42
2a	24.635	45	176	19.32	54.65	7	15.02	-63.86	110.90	43.73	174.64	0.31
2b	17597			15.99	39.17	5	33.71	-6.06	99.39	38.39	154.75	0.25

2c	21.1156			61.76	174.69	7	2.58	-61.36	445.30	139.78	538.35	0.32
2d	35.194			22.74	71.91	9	-16.17	-119.66	128.04	49.83	260.27	0.28
ALL	**115.368**			**16.53**	**99.17**	**35**	**3.91**	**-119.66**	**445.30**	**33.33**	**538.35**	**0.18**
						Mersenius						
1	81.254	55	215	22.74	90.97	15	-81.57	-209.99	116.91	47.65	348.70	0.26
2a	61.766			21.54	80.61	13	-21.85	-180.27	142.68	45.61	271.63	0.30
2b	52.263			21.55	74.64	11	7.20	-177.21	96.70	46.26	278.39	0.27
ALL	**173.045**			**13.71**	**87.80**	**40**	**-25.59**	**-209.99**	**142.68**	**27.55**	**348.70**	**0.25**
						Hesiodus						
1	31.227336	50	195	11.85	33.53	7	-16.98	-69.27	26.14	26.83	131.19	0.26
2	23.096576	70	273	4.36	9.75	4	4.65	-1.09	21.85	11.03	133.15	0.07
3	5.2176	200	780	6.61	14.78	4	11.02	4.78	38.79	16.73	93.22	0.16
4	6.9568	230	897	18.92	42.32	4	30.33	-52.76	42.44	47.89	152.33	0.28
5	13.56576	200	780	7.87	17.60	4	-0.70	-35.48	3.97	19.92	184.00	0.10
6	17.04416	150	585	15.42	34.48	4	2.29	-30.03	53.71	39.02	197.84	0.17
7	27.8272	100	390	14.00	42.01	8	44.91	-34.54	100.92	31.12	185.32	0.23
8	36.17536	70	273	19.81	59.44	8	1.26	-128.35	69.43	44.03	179.18	0.33
9	18.08768	150	585	12.17	29.80	5	11.36	-21.72	58.37	29.21	187.91	0.16
10	18.6964	130	507	25.02	61.28	5	13.57	-116.44	37.12	60.05	161.03	0.38
11	42.6104	70	273	14.77	48.99	10	-32.33	-107.69	67.38	32.00	217.31	0.23
12	19.566	150	585	31.49	77.14	5	-30.96	-128.51	55.73	75.59	221.20	0.35
13	31.04472	90	351	17.12	48.43	7	10.36	-110.94	37.57	38.75	229.04	0.21
14	39.132	70	273	15.47	48.92	9	-20.22	-31.55	96.35	33.90	189.87	0.26
15a	52.176	65	254	11.51	41.50	12	-21.73	-54.64	61.73	24.52	258.17	0.16

15b	39.132	70	273	18.00	59.70	10	-57.44	-124.74	60.66	39.00	232.41	0.26
ALL				**4.71**	**51.98**	**121**	**0.86**	**-128.51**	**100.92**	**9.30**	**258.17**	**0.20**
Schrödinger												
1	77.73427	101	393	90.51	359.64	16	-120.47	-425.62	527.76	188.86	1085.45	0.33
2	14.25864	201	783	43.25	105.94	5	113.68	-14.19	279.15	103.82	433.80	0.24
3	69.34752	101	393	51.42	205.69	15	-112.03	-314.30	384.25	107.75	862.06	0.24
4	112.4555	66	257	38.76	189.87	23	-269.89	-427.11	147.96	79.34	1115.20	0.17
ALL				**33.29**	**254.13**	**62**	**-71.48**	**-427.11**	**527.76**	**66.32**	**1115.20**	**0.23**
Goclenius 1												
1	17.92339	43	166	7.62	18.67	5	-4.81	-41.88	7.86	18.30	57.60	0.32
2	23.87755	53	205	11.64	30.79	6	-10.10	-48.45	38.85	26.99	102.22	0.30
3	14.46432	95	371	8.22	18.37	4	31.81	-0.35	42.99	20.79	122.56	0.15
4	20.9352	66	255	6.96	17.04	5	4.64	-29.60	14.35	16.70	105.66	0.16
5	20.05973	53	205	13.32	29.79	4	14.07	-34.61	36.79	33.71	92.52	0.32
6	27.97704	53	205	11.24	31.79	7	5.56	-23.36	79.52	25.44	138.33	0.23
7–9	18.15462	100	390	14.57	56.43	14	-12.45	-45.11	102.77	30.67	151.13	0.37
10,11	17.71403	130	507	35.01	110.70	9	-33.04	-102.52	222.66	76.71	291.42	0.38
12	45.94801	42	164	18.99	68.47	12	-43.95	-130.47	113.39	40.46	245.06	0.28
ALL				**7.02**	**60.82**	**74**	**-0.35**	**-130.47**	**222.66**	**13.95**	**291.42**	**0.21**
Plinius												
1A	121.25	50	190	35.86	107.59	8	129.25	56.63	388.95	79.70	388.95	0.28
1B	31.43	80	312	14.63	67.05	20	199.15	102.95	322.14	30.15	312.07	0.21
ALL	**89.81**			**15.61**	**82.61**	**27**	**175.63**	**56.63**	**388.95**	**31.76**	**388.95**	**0.21**

Sirsalis												
1	36.83585	250	975	70.33	211.00	8	-54.37	-299.61	246.61	156.31	746.06	0.28
2	45.26292	200	780	57.00	180.24	9	5.85	-258.69	321.39	124.90	752.67	0.24
3	57.43149	90	351	32.27	116.35	12	26.09	-253.34	244.06	68.76	423.93	0.27
4	39.75492	80	312	59.25	177.75	8	-136.36	-203.91	254.05	131.68	400.54	0.44
5	20.13616	80	312	8.69	19.43	4	-1.12	-35.98	9.52	21.99	109.25	0.18
6	61.66529	90	351	43.92	164.33	13	-22.68	-245.71	274.37	92.97	585.80	0.28
7	46.63364	100	390	36.49	121.02	10	-6.93	-56.46	307.48	79.06	479.15	0.25
8	20.82152	80	312	22.21	54.41	5	-35.98	-88.64	43.04	53.32	127.97	0.43
9,10	90.23624	60	234	14.35	97.33	45	-54.85	-271.93	186.34	28.76	694.77	0.14
11	93.05492	65	254	5.13	11.47	4	26.72	15.25	38.19	12.98	452.09	0.03
ALL	**19.48748**			**12.39**	**140.15**	**127**	**-27.75**	**-299.61**	**321.39**	**24.47**	**752.67**	**0.19**